

---

# Field-level Inference of the Baryon Acoustic Oscillation Scale

Ivana Babić

---



München 2024



---

# Field-level Inference of the Baryon Acoustic Oscillation Scale

Ivana Babić

---

Dissertation  
an der Fakultät für Physik  
der Ludwig-Maximilians-Universität  
München

vorgelegt von  
Ivana Babić  
aus Split, Croatia

München, den 12.9.2024.

Erstgutachter: Prof. Dr. Eiichiro Komatsu

Zweitgutachter: Prof. Dr. Ariel Sánchez

Tag der mündlichen Prüfung: 17.10.2024.

# Contents

<b>Zusammenfassung</b>	<b>xv</b>
<b>1 Introduction</b>	<b>1</b>
1.0.1 Notation . . . . .	4
<b>2 Cosmological Setup</b>	<b>5</b>
2.1 Robertson-Walker Metric . . . . .	5
2.1.1 Redshift . . . . .	7
2.1.2 Distances . . . . .	7
2.2 Dynamics of the Universe . . . . .	9
2.2.1 Homogeneous Universe . . . . .	9
2.3 Perturbed spacetime . . . . .	10
<b>3 Structure Formation</b>	<b>13</b>
3.1 Standard Perturbation Theory . . . . .	14
3.1.1 Linear Solution . . . . .	15
3.1.2 Nonlinear solution . . . . .	16
3.2 Effective Field Theory of Large Scale Structure . . . . .	18
3.2.1 Equations of Motion in EFT . . . . .	19
3.2.2 EFT Power spectrum and renormalization . . . . .	21
3.3 Lagrangian Perturbation Theory . . . . .	21
<b>4 From evolved matter to biased tracers</b>	<b>25</b>
4.1 General Bias Expansion . . . . .	25
4.2 Lagrangian Bias Expansion . . . . .	27
4.3 Eulerian Bias Expansion . . . . .	30
4.4 Higher-derivative bias . . . . .	31
4.5 Renormalized galaxy bias . . . . .	32
<b>5 Baryon Acoustic Oscillations</b>	<b>35</b>
5.1 Physics of Baryon Acoustic Oscillations . . . . .	35
5.1.1 Boltzmann equation for Photons . . . . .	36
5.1.2 Boltzmann Equation For Baryons . . . . .	38

5.1.3	Linear Theory of BAO . . . . .	39
5.1.4	Non-linear Evolution and Galaxy Clustering Bias . . . . .	43
5.2	BAO reconstruction . . . . .	44
5.2.1	Reconstruction Algorithm . . . . .	44
5.2.2	Understanding BAO Reconstruction Using Lagrangian Perturbation Theory . . . . .	45
5.3	Baryon Acoustic Oscillations as a Cosmological Probe . . . . .	48
<b>6</b>	<b>EFT Based Forward Model for BAO inference</b>	<b>53</b>
6.1	EFT based Forward Model . . . . .	54
6.1.1	Initial density field . . . . .	54
6.1.2	EFT likelihood . . . . .	57
6.2	Code Implementation of the forward model . . . . .	58
<b>7</b>	<b>BAO scale inference from biased tracers using the EFT likelihood</b>	<b>61</b>
7.1	Introduction . . . . .	62
7.2	Inference method . . . . .	62
7.3	Field-Level Results . . . . .	63
7.4	Comparing the field-level results to the power spectrum approach . . . . .	66
7.4.1	Power spectrum likelihood . . . . .	66
7.4.2	Results . . . . .	67
7.5	Summary and Conclusions . . . . .	77
<b>8</b>	<b>Straightening the Ruler: Field-Level Inference of the BAO Scale with LEFTfield</b>	<b>79</b>
8.1	Introduction . . . . .	79
8.2	Synthetic Data sets . . . . .	80
8.3	Field level BAO inference . . . . .	81
8.3.1	Sampling method and data analysis . . . . .	81
8.3.2	Field-level results . . . . .	82
8.4	Comparing the field-level results to the reconstruction approach . . . . .	87
8.4.1	BAO Reconstruction Procedure . . . . .	87
8.4.2	Inference results and comparison with the field level . . . . .	90
8.5	Discussion and Conclusions . . . . .	91
<b>9</b>	<b>Summary and Outlook</b>	<b>95</b>
<b>A</b>	<b>Power spectrum covariance for fixed phases</b>	<b>97</b>
<b>B</b>	<b>Details of Data Analysis</b>	<b>101</b>
B.1	Correlation length . . . . .	101
B.2	Parameter posteriors: marginalized likelihood . . . . .	102
B.2.1	Parameter posteriors: non-marginalized likelihood . . . . .	103





# List of Figures

5.1	Evolution of the radial mass profile of a point-like overdensity initially . . .	42
5.2	Illustration of the effects of the BAO reconstruction procedure . . . . .	47
6.1	Comparing the linear power spectrum to the power spectrum approximation.	56
7.1	Profile likelihood $-2 \ln P^{\text{prof}}$ plotted as a function of $\beta$ for two different cut- offs $\Lambda$ at $z = 0$ . The blue line shows the parabolic fit which was used to find the maximum-a-posteriori value $\hat{\beta}$ and its error $\sigma(\hat{\beta})$ . . . . .	64
7.2	MAP value $\hat{\beta}$ found using the EFT likelihood for two bias orders at $z = 0$ . The different sub-figures show four different mass ranges. . . . .	69
7.3	$\sigma_F(\hat{\beta})$ values as a function of $\Lambda$ at $z = 0$ . Different sub-figures show four different mass ranges. . . . .	70
7.4	MAP values for $\beta$ using the EFT likelihood found at different redshifts for run 1. Different panels show four different mass ranges at three different redshifts each. . . . .	71
7.5	MAP values for $\beta$ using the EFT likelihood found at different redshifts for run 2. Different panels show four different mass ranges at three different redshifts each. . . . .	72
7.6	MAP values for $ \hat{\beta} - 1 $ found at the cutoff $\Lambda = 0.16 h \text{ Mpc}^{-1}$ for all halo mass bins and redshifts against $(b_1 - 1)D_{\text{norm}}(z)$ , where $D_{\text{norm}}(z) = D(z)/D(0)$ . .	73
7.7	Profile likelihood $-2 \ln P^{\text{prof}}$ for the power spectrum, plotted as a function of $\beta$ for two different cutoffs $\Lambda$ at $z = 0$ . The blue line shows the parabolic fit which was used to find MAP $\hat{\beta}$ and $\sigma_{PS}(\hat{\beta})$ error. . . . .	73
7.8	MAP values for $\beta$ using the power spectrum likelihood for different $\Lambda$ . Dif- ferent panels show four different mass ranges at three different redshifts. . . . . .	74
7.9	$\sigma_{PS}(\hat{\beta})$ values found using the power spectrum likelihood for different $\Lambda$ . Different panels show four different mass ranges at the redshift $z = 0$ . . . .	75
7.10	Ratio of the uncertainty on the BAO scale inferred from the power spectrum likelihood, $\sigma_{PS}(\hat{\beta})$ , to that from the field-level likelihood, $\sigma_F(\hat{\beta})$ , as a func- tion of cutoff for different redshifts. Each panel corresponds to a different halo mass range. . . . .	76

- 8.1 Trace plot of parameter  $\beta$  for  $\Lambda = 0.2 h \text{ Mpc}^{-1}$  for three independent MCMC chains, where  $n$  denotes the sample index. The chain shown in green started from the true initial conditions  $\hat{s}_{\text{true}}$  while the other two chains started from random initial conditions  $\hat{s}$ . Each chain started from a different initial  $\beta$  value, with all quickly converging to the same value. Dashed black line indicates the ground truth value  $\beta_0$ . . . . . 83
- 8.2 The normalized auto-correlation function for parameter  $\beta$  inferred at  $\Lambda = 0.2 h \text{ Mpc}^{-1}$ . In the figure we also display the correlation length value  $\tau$  together with the maximum separation  $M$  between the samples considered, both of which are defined in App. B. The correlation length of  $\beta$  is estimated to be  $\tau \simeq 244$  samples. In the lower panel, we zoom into the first 1800 samples of the chain. . . . . 84
- 8.3 Inference results for the Mock A. Left panel shows inferred BAO scale relative to ground truth obtained using Lagrangian bias for sampling. FreeIC are represented using circle marker and FixedIC using a square. On the right we show the 68% CL error bar on the BAO scale,  $\sigma_{\text{F}}(\beta)$ , as a function of cutoff  $\Lambda$ . . . . . 85
- 8.4 Inference results for Mock B. The left panel displays the inferred BAO scale relative to the ground truth, where the BAO scale is sampled alongside the initial conditions. The Lagrangian bias points, computed for the same values of  $\Lambda$ , have been slightly displaced horizontally for better visibility. On the right, we show the 68% CL error bar,  $\sigma_{\text{F}}(\beta)$ , as a function of the cutoff  $\Lambda$ . The results obtained using the Lagrangian bias are depicted in blue, while those obtained using Eulerian bias are shown in orange. . . . . 85
- 8.5 Posterior of parameters for the FreeIC inference in the case of Mock B. Left panel (a) represents the Eulerian bias model while the right panel (b) represents the Lagrangian bias. The dotted gray line indicates the ground truth value  $\beta_0$  in each case. The inference was performed at  $\Lambda = 0.18 h \text{ Mpc}^{-1}$  in both cases. . . . . 86
- 8.6 Diagram of two methods of BAO inference; field level inference (top) and power spectrum-based inference with and without reconstruction (bottom). The reconstruction step includes the generation of a discrete tracer catalog from  $\delta_g$ , as described in the text . . . . . 87
- 8.7 The left panel shows the oscillatory part of the power spectrum averaged over 500 Mock A-like realizations. We show this for both the pre- and post-reconstructed power spectrum (for  $\Lambda = 0.2 h \text{ Mpc}^{-1}$ ). We see that following the reconstruction, the wiggles on smaller scales become more pronounced. The right panel shows the inferred error bar  $\sigma_{\text{PS}}(\beta)$  on the BAO scale using pre- and post-reconstruction power spectrum. The gain in BAO scale precision due to reconstruction increases as  $\Lambda$  increases. . . . . 89

8.8	Inferred error bar $\sigma_{\text{PS}}(\beta)$ on the BAO scale using pre- and post-reconstruction power spectrum, relative to that in the field-level inference $\sigma_{\text{F}}$ , in the case of Mock A. This mock was generated (and sampled, in case of field-level inference) using Lagrangian bias. Pre-reconstruction results are depicted using squares, whereas post-reconstruction results are represented by stars. It is evident that, even comparing to power spectrum after BAO reconstruction, the field-level BAO scale inference is more precise, by up to a factor of 1.4, corresponding to a $\sim 2$ times larger survey volume. . . . .	90
8.9	Inferred error bar $\sigma_{\text{PS}}(\beta)$ on the BAO scale from the post-reconstruction power spectrum, relative to that in the field-level inference $\sigma_{\text{F}}$ , in the case of Mock B. Blue points indicate the scenario where the Lagrangian bias is used in the field level inference, while orange points correspond to the Eulerian case (the reconstruction results are the same in both cases). The field-level error bar is consistently smaller, regardless of which bias basis is used in the field-level inference. . . . .	91
A.1	Ratio of the variance of $10^3$ power spectra with fixed phases to the prediction obtained in Eq. (A.18) for a variety of bias and noise parameters. . . . .	99
B.1	Posterior of parameters for the inference performed on Mock B. Top two panels (orange color) corresponds to Eulerian bias, while the lower two panels (blue) correspond to Lagrangian bias. The intermediate cutoff $\Lambda = 0.18 h \text{ Mpc}^{-1}$ behaves similarly, and is not shown here for brevity. . . . .	104
B.2	Posterior of parameters for the inference performed on Mock A. . . . .	105
B.3	Trace plot for parameter $\beta$ in chains generated using the non-marginalized likelihood. Inference was performed at $\Lambda = 0.15 h \text{ Mpc}^{-1}$ for Mock B. . . . .	106
B.4	The normalized auto-correlation function for parameter $\beta$ inferred at $\Lambda = 0.15 h \text{ Mpc}^{-1}$ using the non-marginalized likelihood. We also show the correlation length value $\tau$ together with the maximum separation $M$ between the samples considered. The lower panel zooms in on the first 3000 samples. . . . .	106
B.5	Results of the joint FreeIC inference on the Mock B using non-marginalized likelihood and Eulerian bias. We show the posterior for all noise parameters, bias parameters and $\beta$ . Inference was performed at $\Lambda = 0.15 h \text{ Mpc}^{-1}$ . . . . .	107
B.6	Results of the joint FreeIC inference on the Mock A using non-marginalized likelihood and Lagrangian bias. We show the posterior for all noise parameters, bias parameters and $\beta$ . Inference was performed at $\Lambda = 0.15 h \text{ Mpc}^{-1}$ . . . . .	108



# List of Tables

7.1	Number density of halos in run 1 at different redshifts. . . . .	63
7.2	Summary of the results found using the field-level EFT likelihood at the cutoff $\Lambda = 0.16 h \text{ Mpc}^{-1}$ for different redshifts and halo mass bins. . . . .	65
7.3	MAP values of $\beta$ for cutoff $\Lambda = 0.16 h \text{ Mpc}^{-1}$ inferred from the power spectrum likelihood, at different redshifts for different halo mass ranges. . . . .	67
8.1	Values of parameters used to produce mock datasets A and B. For both mocks, we use second order LPT combined with second order bias expansion and cutoff $\Lambda_0 = 0.3 h \text{ Mpc}^{-1}$ . . . . .	81
B.1	Correlation length values for chains run on the Mock A using Lagrangian bias. . . . .	102
B.2	Correlation length values for chains run on the Mock B using Lagrangian bias.	102
B.3	Correlation length values for chains run on the Mock B using Eulerian bias.	102



# Zusammenfassung

Die baryonische akustische Oszillationsskala (BAO) ist mittlerweile eine der wichtigsten kosmologischen Messgrößen. Durch die Beobachtung ihres Abdrucks in der Verteilung der Galaxien können wir sowohl den Hubble-Parameter als auch den Winkeldurchmesserabstand bestimmen.

Allerdings führen nichtlineare Strukturbildung und Prozesse der Galaxienbildung zu einer Verschiebung und Verbreiterung des BAO-Gipfels in der Korrelationsfunktion, was die Präzision unserer Messungen verringert. Um nichtlineare Effekte zu minimieren, verwenden herkömmliche BAO-Inferenzmethoden ein Verfahren, das als BAO-Rekonstruktion bekannt ist. Diese Methode nutzt die beobachtete Verteilung der Galaxien, um die Verschiebungen durch großräumige Bewegungen zu schätzen und verschiebt die Galaxien damit näher an ihre ursprüngliche Position zurück. Dadurch werden die Galaxien wieder näher an ihre Ausgangsposition gebracht, was die Genauigkeit der BAO-Messung verbessert. Jedoch basiert dieses Verfahren auf einer angenommenen Kosmologie und weiteren galaxienspezifischen Parametern, während es wünschenswert wäre, diese Größen zusammen mit der BAO-Skala zu ermitteln. Darüber hinaus nutzen konventionelle Methoden keine höherwertigen  $n$ -Punkt-Funktionen, die wertvolle Informationen enthalten könnten.

In dieser Dissertation stellen wir eine alternative Technik vor, die auf einer feldbasierten Inferenz und einem Forward-Modeling-Ansatz beruht. Beim Forward Modeling werden die heute beobachtbaren Strukturen direkt aus den anfänglichen Bedingungen, die durch die Inflation gesetzt wurden, entwickelt. Das von uns verwendete Forward-Modell basiert auf der effektiven Feldtheorie der großräumigen Strukturen (EFTofLSS) und wird LEFTfield genannt. Diese Methode ermöglicht es uns, die BAO-Skala, kosmologische Parameter, Bias-Parameter und die Anfangsbedingungen gemeinsam zu bestimmen, um eine vollständig konsistente Inferenz zu gewährleisten. Darüber hinaus liefert unser Modell direkte Informationen aus dem Feld selbst, ohne auf höherwertige  $n$ -Punkt-Funktionen angewiesen zu sein.

Zunächst wenden wir diesen Ansatz auf Kataloge von simulierten Halos im Ruhesystem an, bei denen die Anfangsbedingungen auf die aus der Simulation bekannten tatsächlichen Werte festgelegt sind. Unsere Analyse zeigt eine systematische Abweichung von weniger als 2% für eingesetzte Skalen für den EFT cutoff von  $\Lambda \leq 0,25h\text{Mpc}^{-1}$  über alle untersuchten Datenstufen hinweg, wobei nur die massereichsten Halos eine Abweichung von mehr als 1% aufweisen. Darüber hinaus zeigen wir, dass die feldbasierte Inferenz die Größe der Fehlerbalken im Vergleich zur Leistungsspektrum-basierten Inferenz ohne Verwendung der BAO-Rekonstruktion um das 1,1- bis 3,3-fache reduziert.

Anschließend erweitern wir unsere Analyse auf ein komplexeres Szenario, in dem wir die BAO-Skala gemeinsam mit den Anfangsbedingungen bestimmen. Diese Analyse wird mit simulierten Daten durchgeführt, die mit dem LEFTfield-Code erzeugt wurden. Wir zeigen, dass auch in diesem Fall der systematische Fehler sehr gering bleibt. Darüber hinaus zeigen wir, dass unsere Einschränkungen auf die BAO-Skala niedriger sind als die mit traditionellen BAO-Methoden erzielten.

# Abstract

Baryon acoustic oscillation (BAO) scale has been an important cosmological probe in the past decade. By observing its imprint in the distribution of galaxies at later times, we can estimate both the Hubble parameter and the angular diameter distance. However, nonlinear matter evolution and galaxy formation processes shift and broaden the BAO peak in the correlation function, consequently reducing the precision of our measurement. To minimize non-linear effects, conventional BAO inference employs a method known as BAO reconstruction. This approach uses galaxy maps to estimate bulk motion displacements and shifts the galaxies back closer to their initial position. This restores the galaxies closer to their original positions, improving the accuracy of the BAO scale measurement. Nonetheless, this approach relies on assumed fiducial cosmology and bias values, whereas a more accurate method would involve sampling these quantities along with the BAO scale. Additionally, conventional methods do not utilize higher-order  $n$ -point functions, which may contain valuable information.

In this thesis, we introduce an alternative technique based on the field-level inference and forward modeling approach. Forward modeling takes the initial conditions that were set by the inflation and then evolves them into observable structures as we see today. Forward model we use is based on the Effective Field Theory of Large Scale Structure (EFTofLSS) and called LEFTfield. This method allows us to jointly sample the BAO scale, cosmological parameters, bias parameters, and initial conditions, ensuring a fully consistent inference. Moreover, our model provides insights directly from the field itself, avoiding the need for higher-order  $n$ -point functions.

We first apply this approach to rest-frame halo catalogs, in the case when the initial conditions are fixed to the ground truth. Our analysis shows a systematic bias of less than 2% for the  $\Lambda \leq 0.25, h\text{Mpc}^{-1}$ , where  $\Lambda$  is the maximum wavenumber included in the forward mode. This systematic bias is consistent across all samples, with only the most biased samples showing a systematic bias above 1%. Additionally, we demonstrate that the field-level inference reduces error bar size by 1.1 to 3.3 times compared to the power spectrum based inference without the use of the BAO reconstruction.

We then extend our analysis to a more complex scenario where we sample the BAO scale along with the initial conditions. This analysis is conducted using mock data generated with the LEFTfield code. We demonstrate that, even in this case, systematic bias remains very low. Furthermore, we show that our constraints on the BAO scale are lower than those obtained using traditional BAO methods.



# Chapter 1

## Introduction

Baryon Acoustic Oscillations (BAO) represent one of the most significant observables in cosmology. Originating from the period when photons and baryons were tightly coupled, the imprints of BAO are visible in both the Cosmic Microwave Background (CMB) temperature anisotropies and the clustering of matter at later times. By measuring the apparent size of the BAO scale,  $r_s$ , in the late-time matter distribution, it is possible to estimate both the angular diameter distance and the Hubble parameter as functions of redshift. Moreover, the BAO feature imprinted in galaxy clustering is much less sensitive to the details of the galaxy-matter relation (bias) than the broad-band galaxy statistics. However, the nonlinear evolution of the matter density field and the formation of structures complicate this picture. The bulk motion of matter (and galaxies with it) leads to a damping of the BAO oscillations in the power spectrum, reducing the accuracy with which the BAO scale can be measured from the late-time clustering of galaxies. Additionally, this effect will reduce the size of the BAO scale, shifting its position in the correlation function and introducing a systematic bias into our measurement [51, 94, 120, 124].

Traditional BAO inference methods aim to reduce non-linear effects through a technique known as *BAO reconstruction* [28, 50, 92, 95, 113, 114, 125, 135, 142]. BAO reconstruction is based on the principle that the same galaxy maps used to measure the power spectrum can be used to estimate the displacements caused by bulk motions. The estimated displacement field is then used to shift galaxies back to their original positions, effectively reducing the effects of non-linear evolution.

The BAO reconstruction technique has been highly successful and has played a crucial role in inferring the BAO scale over the past decade [3, 5, 37, 68, 85, 97, 136]. However, this technique relies on assumptions about the underlying cosmology and galaxy bias, which should ideally be sampled alongside the BAO scale for consistent inference. Furthermore, it only extracts information from the power spectrum, whereas higher-order  $n$ -point functions could also provide valuable insight into the BAO scale.

In this thesis, we adopt a different approach to BAO scale inference, and use a fully Bayesian field-level forward modeling approach to constrain the BAO scale. Forward modeling has gained significant momentum in the past few years [10, 53, 54, 61–64, 69, 70, 72, 84, 105, 115–117, 141]. The main goal of the field level inference is to find a joint posterior for

the initial density field, cosmological parameters and nuisance parameters (bias parameters and stochastic amplitudes). This posterior is constructed using the following elements:

- prior on the initial conditions
- forward model for matter and gravity
- bias expansion
- likelihood.

This posterior allows us to jointly sample all the cosmological and bias parameters along with the initial conditions, eliminating the need to rely on a fiducial cosmology<sup>1</sup>

In this work, we demonstrate that field-level inference based on our forward model, which will be detailed below, can effectively constrain the BAO scale. As shown in Chapters 7 and 8, not only is this approach feasible, but we also find that the results for fully nonlinear tracers remain nearly unbiased, even when the BAO scale is sampled jointly with the initial conditions. Furthermore, we show that this method yields tighter constraints on the BAO scale compared to current approaches. This makes the method highly promising for future cosmological analyses.

The forward model we use is based on the Effective Field Theory of Large Scale Structure (EFTofLSS) [17, 30]. A key component of any EFT framework is the cut-off scale, denoted as  $\Lambda$ , which represents the maximum wavenumber of the modes included in the calculations (in  $n$ -point-function-based analyses, this is often referred to as  $k_{\max}$ ). The cut-off  $\Lambda$  excludes the impact of small-scale physics, which cannot be accurately modeled using perturbation theory. While  $\Lambda$  can theoretically take any value, the upper limit in the EFTofLSS is set by the nonlinearity scale ( $\Lambda_{\text{NL}} \approx 0.25 h \text{ Mpc}^{-1}$  at  $z = 0$ ), beyond which the perturbation theory for large-scale structure breaks down. By applying this cut-off to the initial density field, we ensure that all considered modes remain within perturbative control from the outset. Importantly, the information about small-scale physics is not lost; rather, it is captured through counterterms that are introduced during the renormalization process.

The language of EFTofLSS allows us to express the highly complex relationship between the matter density field and the tracer density field in terms of *bias operators*  $O$  [42]:

$$\delta_g(\mathbf{x}, \eta) = \sum_O b_O(\eta) O(\mathbf{x}, \eta), \quad (1.1)$$

where *bias coefficients*  $b_O$  parameterize our ignorance about small scale physics. In other words, they correct the error we make by ignoring all modes above  $\Lambda$ . Choice of operators  $O$  is determined by the equivalence principle. Up to any given order in perturbation theory, we have a finite number of such operators, forming what is known as a basis. Importantly, the choice of this basis is not unique. In this work, we will employ both a

---

<sup>1</sup>In this study, we fix all cosmological parameters apart from the BAO scale in the inference, but all bias parameters are jointly inferred with the BAO scale.

Lagrangian basis, which includes operators constructed at an initial time, and an Eulerian basis, whose operators are expressed at the observation time.

At the center of the forward model we are using is the so-called *field-level* or EFT likelihood, which has been derived in a series of papers [29, 52, 112]. The key feature of this likelihood is that it enables us to access information directly from the field, without relying on compression functions. As a result, it captures the BAO information contained in higher  $n$ -point functions, such as the bispectrum.

## Thesis Outline

This thesis is structured in the following way:

- Chapter 2: In this chapter, we establish the foundations for the subsequent chapters. We introduce the background cosmological model used to describe our universe and define measurements within this framework. Additionally, we briefly introduce perturbations in spacetime.
- Chapter 3: We begin this chapter by deriving a set of partial differential equations that govern the evolution of dark matter and gravity. We then discuss various methods for solving these equations. First, we explore the standard perturbation theory approach, which treats the matter density as a small perturbative parameter. Afterward, we examine the limitations of this method, which motivate the introduction of the Effective Field Theory of Large Scale Structure (EFTofLSS). Finally, we conclude the chapter by introducing Lagrangian perturbation theory, offering an alternative approach to solving these equations within the Lagrangian framework, where we also briefly mention how EFTofLSS fits in the context of this approach.
- Chapter 4: This chapter addresses galaxy bias, which provides the relationship between the matter and galaxy density fields. We begin with the local-in-matter-density bias expansion and demonstrate why this approach is incomplete. Using the equivalence principle, we then derive a more general bias expansion. Next, we discuss both Lagrangian and Eulerian bias expansions, presenting the explicit form of bias operators up to the 4th order in each framework. Additionally, we discuss the renormalization of galaxy bias.
- Chapter 5: In this chapter we focus on baryon acoustic oscillations (BAO). We start this section by providing some necessary background in the form of Boltzmann equations for photons and the Boltzmann equations for baryons. We then discuss the joint evolution of photons and baryons in the form of baryon-photon fluid. We show that the equation governing this fluid has a form of forced harmonic oscillator and discuss the physical intuition behind this. Next we discuss in more details how non-linear evolution and galaxy bias distort the BAO feature by displacing galaxies from their original position. After that, we introduce the BAO reconstruction as a means of fixing the effects of non-linearities. In the final part of this chapter, we show

how by measuring the apparent size of the BAO scale at some redshift  $z$  from the late time clustering of matter, we can directly measure the Hubble parameter  $H(z)$  and the angular diameter distance  $D_A(z)$  relative to the sound horizon scale  $r_s$ .

- Chapter 6: In this chapter we introduce the concept of field-level inference and forward modeling. We describe all the ingredients needed to construct our forward model based on EFTofLSS. Additionally, we explain how this model is applied to infer the Baryon Acoustic Oscillation (BAO) scale.
- Chapter 7: In this chapter, we apply the forward model introduced in the previous section to a rest-frame halo catalog and perform BAO scale inference, with the initial conditions fixed to the ground truth. We then compare the field-level results to those obtained using a Gaussian power spectrum-based likelihood, without implementing BAO reconstruction.
- Chapter 8: In this chapter, we conduct a joint inference of the BAO scale and the initial conditions of mock catalogs generated using our forward model. This analysis is performed using both Lagrangian and Eulerian bias expansions. Finally, we compare our results with those obtained using the reconstructed power spectrum and Gaussian power spectrum-based likelihood.
- Chapter 9: This final chapter summarizes the main results of the thesis and outlines plans for future research.

### 1.0.1 Notation

We use bold letters such as  $\mathbf{p}$  to indicate vectors.

The momentum space integrals are written as

$$\int_{\mathbf{p}_1, \dots, \mathbf{p}_n} = \int \frac{d^3 p_1}{(2\pi)^3} \cdots \int \frac{d^3 p_n}{(2\pi)^3}. \quad (1.2)$$

### Relevant Publications

The content of this thesis is based on the following publications:

- Ivana Babić , Fabian Schmidt, and Beatriz Tucci. *BAO scale inference from biased tracers using the EFT likelihood*. Published in JCAP, Volume 2022, August 2022. Preprint: 2203.06177.
- Ivana Babić , Fabian Schmidt, and Beatriz Tucci. *Straightening the Ruler: Field-Level Inference of the BAO Scale with LEFTfield*. Preprint: 2407.01524.

# Chapter 2

## Cosmological Setup

In this section, we will explore the geometry of our universe. First, we will introduce the Friedmann–Lemaître–Robertson–Walker (FLRW) metric, which describes an expanding homogeneous and isotropic universe. Following that, we will discuss how distances are defined within this framework, and introduce the concept of standard ruler and standard candles as tools for these measurements. In the final section of the chapter, we will briefly introduce the concept of metric perturbations.

This chapter was based on several chapters in [45] and several chapters in [87].

### 2.1 Robertson-Walker Metric

To describe the laws of gravity, we use general relativity. The fundamental object of theory of relativity is *metric*  $g_{\mu\nu}$ , a mathematical object that describes the geometry of spacetime. Metric defines how distances and intervals between events in spacetime are measured and it allows us to connect observer-dependent coordinates  $x_\mu = (t, \mathbf{x})$  to the invariant line elements:

$$ds^2 = g_{\mu\nu} dx^\mu dx^\nu. \quad (2.1)$$

The way the metric varies with position in spacetime is governed by the distribution of matter and energy in the universe. Finding the metric of an arbitrary spacetime can be challenging, but knowing the symmetry of the spacetime makes the problem easier.

Our universe is isotropic and homogeneous on large scales, and can thus be described using the Friedmann–Lemaître–Robertson–Walker (FLRW) metric:

$$ds^2 = -dt^2 + \gamma_{ij} dx^i dx^j, \quad (2.2)$$

where

$$\gamma_{ij} dx^i dx^j = a^2(t) \left( \frac{dr^2}{1 - Kr^2} + r^2 d\Omega^2 \right), \quad (2.3)$$

and

$$d\Omega^2 = d\theta^2 + \sin^2(\theta) d\phi^2, \quad (2.4)$$

with  $r$  being the radial coordinate. The scale factor  $a(t)$  characterizes the expansion of the universe. Due to the isotropy and homogeneity of the universe, the scale factor depends only on time. By convention, the present value of the scale factor, denoted  $a_0$ , is set to one. As we look further back in time, the value of  $a$  decreases, reflecting the fact that the universe was smaller in the past. The parameter  $K$  represents the spatial curvature of the universe and can take one of three values, corresponding to different types of geometry:

$$K \equiv \begin{cases} 0 & \text{Euclidean (flat) space,} \\ +1 & \text{spherical (closed) space,} \\ -1 & \text{hyperbolic (open) space.} \end{cases} \quad (2.5)$$

The value of  $K$  can only be determined through observational data. According to results from the Planck mission, observations strongly favor a flat universe [2], so we will adopt  $K = 0$  in the following discussion unless stated otherwise.

Coordinates  $\{x^i\}$  are referred to as *comoving coordinates*. The distance between two points expressed in comoving coordinates remains constant as the universe expands. Comoving coordinates can be related to *physical coordinates* through the relation:

$$x_{\text{phys}}^i = a(t)x^i. \quad (2.6)$$

The physical velocity of an object is given by:

$$v_{\text{phys}}^i \equiv \frac{dx_{\text{phys}}^i}{dt} = a(t)\frac{dx^i}{dt} + \frac{da}{dt}x^i = v_{\text{pec}}^i + Hx_{\text{phys}}^i. \quad (2.7)$$

We see that there are two contributions to physical velocity. First one is the *peculiar* velocity:

$$v_{\text{pec}}^i \equiv a(t)\frac{dx^i}{dt}. \quad (2.8)$$

This is the velocity as measured by a comoving observer. The second contribution to the physical velocity arises from the *Hubble flow*,  $Hx_{\text{phys}}^i$ , where the Hubble parameter is defined as:

$$H \equiv \frac{1}{a} \frac{da}{dt}. \quad (2.9)$$

When working with FLRW metric, it is often convenient to replace the physical time  $t$  with *conformal time*  $\eta$ , defined as:

$$\eta \equiv \int \frac{dt}{a(t)}, \quad (2.10)$$

so that the differential time element  $dt$  can be expressed as  $dt = a(t)d\eta$ . Using the conformal time simplifies the flat FLRW metric, allowing it to be rewritten in the following form:

$$ds^2 = a^2(t) [-d\eta^2 + (dr^2 + r^2d\Omega^2)]. \quad (2.11)$$

This representation makes the FLRW metric conformally related to the metric describing the flat Minkowski spacetime,  $ds^2 = -d\eta^2 + dr^2 + r^2 d\Omega^2$ . This similarity makes certain calculations and theoretical analyses simpler by making the metric easier to compare with the familiar flat spacetime metric. As we will soon see, this is particularly useful in the study of perturbations and the evolution of cosmic structures.

### 2.1.1 Redshift

Most of our knowledge about the universe comes from measuring the light emitted by very distant objects. However, before we can draw any conclusions from these measurements, we must account for the effect that the expansion of the universe has on the wavelength of the light emitted by these objects. As the universe expands, the wavelength of the light is stretched, meaning that the observed wavelength appears longer than the wavelength at the time of emission. This stretching is proportional to the scale factor of the universe. To quantify this effect, we define a stretching factor, commonly known as the *redshift*, denoted by  $z$ :

$$1 + z = \frac{\lambda_{\text{observed}}}{\lambda_{\text{emitted}}} = \frac{a_0}{a_{\text{emit}}} = \frac{1}{a_{\text{emit}}}, \quad (2.12)$$

where  $\lambda_{\text{observed}}$  is the wavelength we detect, and  $\lambda_{\text{emitted}}$  is the wavelength that was originally emitted. Similarly,  $a_{\text{emit}}$  is the scale factor at the time of emission and we have used the fact that the observation scale factor, i.e., the present-day scale factor, is set to one. The redshift  $z$  provides a direct measurement of how much the universe has expanded since the light was emitted and it plays an important role in understanding cosmic distances and the evolution of the universe.

### 2.1.2 Distances

Measuring distances in an expanding universe is challenging, and we must carefully define what we mean by “distance”, as there are several different interpretations of it in cosmology.

#### Comoving Distance

We begin by introducing a quantity that, while not directly observable, will prove useful in defining observable distances: the *comoving distance*  $\chi$ . Let us assume we are looking into some distant object which emitted a light ray at some redshift  $z$ . Then the total comoving distance light will travel to reach us is given by:

$$\chi(z) = \int_{t_1}^{t_0} \frac{dt}{a(t)} = \int_0^z \frac{dz}{H(z)}, \quad (2.13)$$

where evolution of  $H(z)$  depends on the matter content on the universe, therefore light will cover different conformal distances during different stages of universe evolution.

### Angular Diameter Distance

One way to define distance is through the use of *standard rulers*. Standard rulers are objects whose size at a given redshift  $z$  is well known, allowing us to determine the distance-redshift relation.

Let us assume that we have a standard ruler of size  $l$ . Since this object is very far away from us, the angular size  $\delta\theta$  of this object is small. In this case, the distance to the object can be determined by the following relation:

$$D_A = \frac{l}{\delta\theta}. \quad (2.14)$$

This quantity is called the *angular diameter distance*  $D_A$ . To translate this relation in terms of expanding universe, we note that the comoving size of this object is  $l/a$ , where  $a$  is the scale factor at the time of emission. The comoving distance to the object is given by Eq. (2.13). Therefore:

$$\delta\theta = \frac{l/a}{\chi(a)}, \quad (2.15)$$

which brings us to the angular diameter distance in Euclidean space:

$$D_A^{Euc} = a\chi = \frac{\chi}{1+z}. \quad (2.16)$$

We immediately observe that in an expanding universe, the angular diameter distance depends on the redshift,  $z$ . For small values of  $z$ , the angular diameter distance closely corresponds to the comoving distance, and the relationship between an object's size and its distance is intuitive: objects farther away appear smaller. However, beyond a certain redshift, the angular diameter distance begins to decrease as the redshift increases, causing distant objects to appear larger than expected. This is a direct consequence of the universe's expansion. When the light from these distant objects was emitted, the universe was much smaller and the object was actually much closer at that time than it is now.

### Luminosity distance

We can also define distances using objects of known luminosity  $L$  (energy emitted per second). Such objects are called *standard candles*. In a flat non expanding universe, the flux  $F$  observed at some distance  $d$  from such an object would be:

$$F = \frac{L}{4\pi d^2}. \quad (2.17)$$

To derive the expression for the observed flux in an expanding universe, we consider the flux measured at a comoving distance  $\chi(z)$ , assuming that all photons were emitted from the source with the same energy. The expansion of the universe impacts these photons in two ways:

- The rate at which photons from the source reach us will be reduced by a factor of  $1/(1+z)$ , compared to the rate at which they were emitted.
- The observed energy of the photons will also be diminished by the same factor  $1/(1+z)$ , compared to the emitted energy.

Taking these effects into account, the observed flux is given by

$$F = \frac{L}{4\pi\chi^2(z)(1+z)^2}, \quad (2.18)$$

where  $L$  is the luminosity of the source. This definition allows us to introduce the *luminosity distance* in Euclidian expanding universe:

$$d_L^{\text{Euc}} \equiv \chi(1+z). \quad (2.19)$$

We see that the luminosity distance and angular diameter distance are related by

$$D_A = \frac{d_L}{(1+z)^2}. \quad (2.20)$$

## 2.2 Dynamics of the Universe

### 2.2.1 Homogeneous Universe

Dynamics of the universe is described with the Einstein equations

$$R_{\mu\nu} - \frac{1}{2}g_{\mu\nu}R = 8\pi GT_{\mu\nu} + \Lambda g_{\mu\nu}, \quad (2.21)$$

where  $R_{\mu\nu}$  is the Ricci tensor,  $R$  is the Ricci scalar,  $T_{\mu\nu}$  is the energy-momentum tensor,  $\Lambda$  is cosmological constant, and  $G$  is the gravitational constant. Full form of the Ricci scalar, and tensors can be found in [87]. The left-hand side of this equation represents the curvature of spacetime, while the right-hand side relates it to the matter and energy content of the universe.

Let us start with the right-hand side of the Einstein equations. We can derive the expression for the energy momentum tensor using the isotropy and homogeneity of the universe. We start by decomposing it in 3-scalar,  $T_{00}$ , 3-vectors,  $T_{i0}$  and  $T_{0j}$ , and a 3-tensor,  $T_{ij}$ . Isotropy demands that mean of 3-vector vanish,  $T_{i0} = T_{0j} = 0$ . Isotropy around  $\mathbf{x} = 0$  further implies that

$$T_{ij}(\mathbf{x} = 0) \propto \delta_{ij} \propto g_{ij}(\mathbf{x} = 0). \quad (2.22)$$

To satisfy homogeneity, this proportionality term can only be a function of time. Therefore, homogeneity and isotropy lead us to the following form of the stress-energy tensor, which corresponds to that of a perfect fluid:

$$T_{\mu\nu} = (p + \rho)u_\mu u_\nu + g_{\mu\nu}p, \quad (2.23)$$

where  $u_\mu$  is the four-velocity of the fluid relative to the observer, while  $\rho \equiv \rho(t)$  and  $p \equiv p(t)$  are the background pressure and density.

Let us also add that the energy and momentum conservation are now combined in one condition:

$$\nabla_\mu T^{\mu\nu} = \partial_\mu T^{\mu\nu} + \Gamma_{\mu\lambda}^\mu T_\nu^\lambda - \Gamma_{\mu\nu}^\lambda T_\lambda^\mu = 0, \quad (2.24)$$

where  $\Gamma_{\mu\nu}^\lambda$  are Christoffel symbols:

$$\Gamma_{\mu\nu}^\lambda = \frac{1}{2} g^{\lambda\rho} (\partial_\mu g_{\nu\rho} + \partial_\nu g_{\mu\rho} - \partial_\rho g_{\mu\nu}). \quad (2.25)$$

From the  $\nu = 0$  component of this equation, we derive the continuity equation

$$\frac{\partial\rho}{\partial t} + 3H(\rho + p) = 0. \quad (2.26)$$

If we combine the solution for the Ricci tensor and Ricci scalar with the momentum tensor, we will arrive to *Friedmann equations*

$$\left(\frac{\dot{a}}{a}\right)^2 = \frac{8\pi G}{3}\rho, \quad (2.27a)$$

$$\frac{\ddot{a}}{a} = -\frac{4\pi G}{3}(\rho + 3p). \quad (2.27b)$$

Friedman equations describe how background cosmology evolves in FLRW universe.

Density  $\rho$  and the pressure  $p$  are the sum of all contributions to the density and the pressure in the universe. In fact, the first Friedmann equation is much more frequently written in a form that reflects this better:

$$H^2 = H_0^2 (\Omega_r a^{-4} + \Omega_m a^{-3} + \Omega_\Lambda), \quad (2.28)$$

with

$$\Omega_i = \frac{8\pi G}{3H_0^2} \rho_{0,i}. \quad (2.29)$$

Dimensionless density parameters  $\Omega_i$  quantify the fraction of the universe's total density associated with each specific component. Specifically,  $\Omega_r$  accounts for the contribution from radiation (photons and neutrons),  $\Omega_m$  corresponds to the matter contribution (including both dark and baryonic matter), and  $\Omega_\Lambda$  represents the contribution from the cosmological constant (dark energy). These components evolve differently with the scale factor  $a$ , which is reflected in the distinct powers of  $a$  in the equation: radiation scales as  $a^{-4}$ , matter as  $a^{-3}$ , and dark energy remains constant.

## 2.3 Perturbed spacetime

Up to this point, we have treated the universe as homogeneous. However, to describe the process of structure formation, it is necessary to go beyond this assumption and introduce

inhomogeneities into both sides of the Einstein equations. In this section, we will briefly introduce the concept of metric perturbations. In the subsequent chapters, we will explore perturbations in the matter density in greater detail.

The background metric we previously considered was time-dependent only. However, introducing inhomogeneities will also bring in spatial dependence. We will assume that these inhomogeneities are small, allowing the perturbed metric to remain close to the background FLRW metric. To quantify these perturbations, we introduce two scalar fields,  $\Phi(\mathbf{x}, t)$  and  $\Psi(\mathbf{x}, t)$ . In terms of these fields, the metric can be expressed as:

$$\begin{aligned} g_{00}(\mathbf{x}, t) &= -1 - 2\Psi(\mathbf{x}, t), \\ g_{0i}(\mathbf{x}, t) &= 0, \\ g_{ij}(\mathbf{x}, t) &= a^2(t)\delta_{ij} [1 + 2\Phi(\mathbf{x}, t)] \end{aligned} \tag{2.30}$$

We see that when we set  $\Phi = \Psi = 0$ , we recover FLRW universe.

The perturbation fields  $\Psi(\mathbf{x}, t)$  and  $\Phi(\mathbf{x}, t)$  are scalars. While vector and tensor perturbations can also exist, we will focus solely on scalar perturbations, as they are sufficient for the purposes of this thesis. Moreover, perturbation fields are gauge dependant, and our choice corresponds to the conformal Newtonian gauge. The field  $\Psi(\mathbf{x}, t)$  corresponds to the Newtonian potential which describes the motion of non-relativistic particles. While it is possible to derive evolution equations for both  $\Psi(\mathbf{x}, t)$  and  $\Phi(\mathbf{x}, t)$ , we will primarily be concerned with scales that are well within the Hubble radius and with non-relativistic matter. In this regime, the Poisson equation will suffice:

$$\nabla^2\Psi = 4\pi G a^2 \rho \delta, \tag{2.31}$$

where  $\rho$  represents the background matter density field. Variable  $\delta$  represents the fluctuation in matter density field which will be the topic of the next chapter.



# Chapter 3

## Structure Formation

The matter distribution in the early Universe was remarkably smooth, with only small fluctuations in the average overdensity amplitude. However, under the influence of gravitational forces, these overdensities grew and evolved into the large-scale structures we observe today. In this section, we will focus on working out the theory that will allow us to understand how this evolution happened.

We will assume that dark matter can be described as a set of collisionless and non-relativistic particles which interact only gravitationally. In other words, we will be treating dark matter as a fluid. Using the full theory of gravity would be rather challenging. Luckily, even for later universe gravity remains relatively weak which allows us to use the linear form of Einstein equations. Using all these assumptions, we will derive a set of partial differential equations describing the dark matter and gravity evolution. We will first address the equations using Standard Perturbation Theory (SPT), which focuses on the matter density and velocity fields and treats their components as small perturbations. However, when examining loop integrals within this theory, problems arise because SPT includes contributions from arbitrarily small scales, where the matter density can no longer be treated as a small parameter. To address this issue, we introduce the Effective Field Theory of Large Scale Structure (EFTofLSS), which incorporates a cut-off to properly account for small-scale effects. Although the cut-off value can, in principle, take any value, in the case of EFTofLSS, it should not exceed the nonlinearity scale at which density perturbations become of order unity.

This chapter will also discuss Lagrangian Perturbation Theory (LPT), an alternative approach that focuses on the evolution of the fluid in the Lagrangian frame, rather than the Eulerian frame previously considered. LPT uses the Lagrangian displacement vector to relate the observed position of the fluid to its initial Lagrangian position. By treating the components of this vector as small perturbations, we can describe the evolution of the dark matter fluid.

This chapter is based on several references. Section 3.1 is primarily based on [13] and Chapter 12 of [45]. The main references for Section 3.2 are [13, 17, 101]. Section 3.3 follows [13, 109].

### 3.1 Standard Perturbation Theory

In cosmology, we are not concerned with the fate of individual particles. Instead, we focus on studying the behavior of large groups of particles in certain regions of space. To describe the behavior of such groups, we use distribution functions. The distribution function  $f(\mathbf{x}, \mathbf{p}, t)$  gives the number of particles within an infinitesimal momentum-space element  $d^3p$  located within an infinitesimal volume element  $d^3x$  centered around a point  $\mathbf{x}$  at time  $t$ . We can relate the distribution function to the number of particles. Throughout this chapter, we will assume we are dealing with non-interacting particles, whose number is conserved. This assumption leads us to the collisionless Boltzmann equation:

$$\frac{df}{dt} = \frac{\partial f}{\partial t} + \frac{\partial f}{\partial x^i} \frac{dx^i}{dt} + \frac{\partial f}{\partial p^i} \frac{dp^i}{dt} = 0. \quad (3.1)$$

Furthermore, we are interested in sub-horizon scales and non-relativistic matter. In this case, the Boltzmann equation becomes:

$$\frac{\partial f}{\partial t} + \frac{\partial f}{\partial x^i} \frac{p^i}{ma} - \frac{\partial f}{\partial p^i} \left( Hp^i + \frac{m}{a} \frac{\partial \Psi}{\partial x^i} \right) = 0, \quad (3.2)$$

where  $m$  is the mass of the particles. This equation is called the Vlasov equation and, together with the Poisson equation, describes the evolution of dark matter under the influence of gravity. To solve this complicated set of equations, we can use the Standard Perturbation Theory (SPT) (see [19] or Chapter 12.2 in [45]). Furthermore, we are not interested in the full solution in momentum space, only in the evolution of the spatial distribution. This allows us to simplify the problem by exploiting the momentum moments of the Boltzmann equation. For this purpose, we introduce a momentum average which for some function  $A(\mathbf{x}, \mathbf{p}, t)$  is defined as

$$\langle A(\mathbf{x}, t) \rangle_f \equiv \int_p A(\mathbf{x}, \mathbf{p}, t) f(\mathbf{x}, \mathbf{p}, t). \quad (3.3)$$

Using this definition allows us to express two important quantities in a convenient way

- number density:

$$n(\mathbf{x}, t) \equiv \langle 1 \rangle_f = \frac{\rho(\mathbf{x}, t)}{m} \quad (3.4)$$

- the bulk or fluid velocity:

$$u^i(\mathbf{x}, t) \equiv \frac{\langle p^i \rangle_f}{\langle m \rangle_f} \quad (3.5)$$

- stress tensor:

$$\tau^{ij} = \frac{1}{m} \langle p^i p^j \rangle_f - \rho u^i u^j. \quad (3.6)$$

Taking the first two moments of the Vlasov equation and applying some algebraic manipulations brings us to the continuity and Euler equation:

$$\frac{\partial \rho}{\partial \eta} + \frac{\partial}{\partial x^i} (\rho u^i) + 3\mathcal{H}\rho = 0 \quad (3.7a)$$

$$\frac{\partial}{\partial t} u^i + u^j \frac{\partial}{\partial x^j} u^i + \mathcal{H}u^i + \frac{\partial \Psi}{\partial x^i} + \frac{1}{\rho} \frac{\partial}{\partial x^j} \tau^{ij} = 0, \quad (3.7b)$$

here used the relation between proper time  $t$  and conformal time  $\eta$ , given by  $dt = a(\eta)d\eta$ , and introduced the conformal Hubble parameter  $\mathcal{H} = aH$ .

The stress tensor  $\tau^{ij}$  can be interpreted as a pressure contribution. In SPT, we assume that the dark matter is a perfect fluid which allows us to set  $\tau^{ij} = 0$ . As we will see later, this assumption will be one of the breaking points of SPT since a more correct way of treating matter would be as an effective fluid. However, even with this assumption we can explore and understand a lot about large scale structures.

By removing the homogeneous solution  $\rho(t)$  through relation  $\rho(\mathbf{x}, t) = \rho(t)[1 + \delta(\mathbf{x}, t)]$ , we find the following set of nonlinear equations describing the dark matter evolution:

$$\dot{\delta} + \frac{\partial}{\partial x^i} ((1 + \delta)u^i) = 0, \quad (3.8a)$$

$$\dot{u}^i + u^j \frac{\partial}{\partial x^j} u^i + \mathcal{H}u^i + \frac{\partial}{\partial x^i} \Psi = 0, \quad (3.8b)$$

$$\nabla^2 \Psi = \frac{3}{2} \mathcal{H}^2 \Omega_m(\eta) \delta, \quad (3.8c)$$

where dot represents derivative with respect to  $\eta$ . We have also included the Poisson equation which accounts for gravity evolution.

### 3.1.1 Linear Solution

Let us start by ignoring all quadratic terms in Eq. (3.8), this allows us to focus on solving the linear part of the equations

$$\dot{\delta}^{(1)} + \nabla \mathbf{u}^{(1)} = 0 \quad (3.9a)$$

$$\dot{\mathbf{u}}^{(1)} + \mathcal{H}\mathbf{u}^{(1)} = -\nabla \Phi, \quad (3.9b)$$

Linear equations are much simpler to solve since the variables are fully decoupled. The solution becomes even more straightforward if we rewrite the Euler equation in terms of the velocity divergence  $\theta = \nabla \cdot \mathbf{u}$  and the velocity vorticity  $\boldsymbol{\omega} = \nabla \times \mathbf{u}$

$$\dot{\theta}^{(1)} + \mathcal{H}\theta^{(1)} = -\nabla^2 \Phi \quad (3.10a)$$

$$\dot{\boldsymbol{\omega}}^{(1)} + \mathcal{H}\boldsymbol{\omega}^{(1)} = 0. \quad (3.10b)$$

The solution of Eq. (3.10b) is  $\boldsymbol{\omega}^{(1)} \propto a^{-1}$ . This implies that any vorticity present at the initial time decays at the linear level. Therefore, we are free to focus solely on the velocity divergence.

From Eq. (3.9a), we see that the source of velocity divergence is in the time changing density perturbations. This allows us to combine Eq. (3.9a) and Eq. (3.10a) into one

$$\ddot{\delta}^{(1)}(k, \eta) + \mathcal{H}(\eta)\dot{\delta}^{(1)}(k, \eta) - \frac{3}{2}\Omega_m(\eta)\mathcal{H}^2(\eta)\delta^{(1)}(k, \eta) = 0. \quad (3.11)$$

In general, this equation will have two modes as solutions: a growing mode and a decaying mode. Since we are interested in the structure formation, i.e., the growing mode, we will discard the decaying mode. We can then solve this equation by assuming a separable solution of the form

$$\delta^{(1)}(\mathbf{k}, \eta) = D(\eta)\delta_L(\mathbf{k}), \quad (3.12)$$

where  $\delta_L(\mathbf{x})$  is the linear density field which was set by inflation and  $D(\eta)$  is the growth factor

$$D(\eta) = D_0 H(\eta) \int^{a(\eta)} \frac{da'}{\mathcal{H}^3(a')}, \quad (3.13)$$

with  $D_0$  being the normalization constant that ensures  $D(a=1) = 1$  today. In the case of the matter only Universe, the case of an Einstein–de–Sitter (EdS) Universe,  $a \propto t^{2/3}$  so the growth factor is simply  $D(a) = a$ . From Eq. (3.9a), we find the linear solution for the velocity displacement

$$\theta^{(1)}(\mathbf{k}, \eta) = -\mathcal{H}(\eta)f(\eta)D(\eta)\delta_L(\mathbf{k}) \quad (3.14)$$

where we have introduced the growth rate  $f(\eta)$  as

$$f(\eta) \equiv \frac{d \log D(\eta)}{d \log a}. \quad (3.15)$$

For the case of EdS Universe, this factor reduces to Unity.

Before we move back to nonlinear equations, let us also calculate the linear order power spectrum

$$P^{(11)}(\mathbf{k}, \eta) \equiv \langle \delta^{(1)}(\mathbf{k}, \eta)\delta^{(1)}(\mathbf{k}', \eta) \rangle = (2\pi)^3 \delta_D(\mathbf{k} - \mathbf{k}') D^2(\eta) P_L(k), \quad (3.16)$$

where  $P_L$  is the power spectrum of the initial conditions which were set by inflation.

### 3.1.2 Nonlinear solution

Let us now return to nonlinear equations. Similar to the case in the case of linear equations, we can simplify things by separating the Eulerian equation (3.8b) into velocity divergence and rotation parts. For the velocity vorticity, we get the following

$$\boldsymbol{\omega}^{(1)} + \mathcal{H}\boldsymbol{\omega}^{(1)} + \nabla \times (\mathbf{u} \times \boldsymbol{\omega}) = 0. \quad (3.17)$$

This equation demonstrates that if there is no initial vorticity, nonlinear evolution will not generate it. Since we have also observed that any existing vorticity decays at early times, we are justified in neglecting it in our calculations.

Keeping only the velocity divergence produces the final form of the nonlinear equations for dark matter evolution

$$\dot{\delta} + \theta = -\delta\theta - \mathbf{u}\nabla\delta, \quad (3.18a)$$

$$\dot{\theta} + \mathcal{H}\theta + \nabla^2\Psi = -\mathbf{u}\nabla\theta - \nabla(\mathbf{u}\nabla)\mathbf{u}, \quad (3.18b)$$

$$\nabla^2\Psi = \frac{3}{2}\mathcal{H}^2\Omega(\eta)\delta. \quad (3.18c)$$

We start by rewriting them in the form of convolution in Fourier space

$$\dot{\delta} + \theta = \int_{\mathbf{p}_1, \mathbf{p}_2} \alpha(\mathbf{p}_1, \mathbf{p}_2)\theta(\mathbf{p}_1, \eta)\delta(\mathbf{p}_2, \eta)\delta_D(\mathbf{k} - \mathbf{p}_1 - \mathbf{p}_2), \quad (3.19a)$$

$$\dot{\theta} + \mathcal{H}\theta + \frac{3}{2}\mathcal{H}^2\Omega(\eta)\delta = - \int_{\mathbf{p}_1, \mathbf{p}_2} \beta(\mathbf{p}_1, \mathbf{p}_2)\theta(\mathbf{p}_1, \eta)\theta(\mathbf{p}_2, \eta)\delta_D(\mathbf{k} - \mathbf{p}_1 - \mathbf{p}_2), \quad (3.19b)$$

with the kernels

$$\alpha(\mathbf{p}_1, \mathbf{p}_2) = \frac{\mathbf{p}_1 \cdot \mathbf{k}}{p_1^2}, \quad \beta(\mathbf{p}_1, \mathbf{p}_2) = \frac{\mathbf{p}_1 \cdot \mathbf{p}_2}{2p_1^2 p_2^2} k^2. \quad (3.20)$$

These kernels originate from the nonlinear terms in Eq. (3.18) and hence capture the nonlinearity of dark matter evolution. By looking at Eq. (3.19), it is also clear that the evolution of  $\delta(\eta, \mathbf{k})$  and  $\theta(\eta, \mathbf{k})$  is governed by coupling of all modes whose wave vectors sum to  $\mathbf{k}$  as demanded by a homogeneous and isotropic Universe.

We assume the solution of the set of Eq. (3.19) can be found using the perturbative expansion

$$\delta(\mathbf{k}, \eta) = \sum_{n=1}^{\infty} D^n(\eta)\delta^{(n)}(\mathbf{k}), \quad \theta(\mathbf{k}, \eta) = -\mathcal{H}(\eta)f(\eta) \sum_{n=1}^{\infty} D^n(\eta)\theta^{(n)}(\mathbf{k}), \quad (3.21)$$

where the terms  $\delta^{(n)}$  and  $\theta^{(n)}$  contain  $n$  powers of the linear fields. Inserting Eq. (3.21) into Eq. (3.19), gives us the general form of the solution

$$\delta^{(n)}(\mathbf{k}) = \int_{\mathbf{p}_1 \dots \mathbf{p}_n} \delta_D(\mathbf{k} - \mathbf{p}_{12\dots n}) F_n(\mathbf{p}_1, \dots, \mathbf{p}_n) \delta_L(\mathbf{p}_1) \dots \delta_L(\mathbf{p}_n), \quad (3.22a)$$

$$\theta^{(n)}(\mathbf{k}) = \int_{\mathbf{p}_1 \dots \mathbf{p}_n} \delta_D(\mathbf{k} - \mathbf{p}_{12\dots n}) G_n(\mathbf{p}_1, \dots, \mathbf{p}_n) \delta_L(\mathbf{p}_1) \dots \delta_L(\mathbf{p}_n), \quad (3.22b)$$

with kernels  $F_n$  and  $G_n$ . These kernels can be computed recursively. First order kernels are trivial and equal to  $F_1 = G_1 = 1$ . To find the expression for the second order kernels, we insert the linear solution on the right hand side of Eq. (3.19) which leads us to

$$F_2(\mathbf{p}_1, \mathbf{p}_2) = \frac{5}{7}\alpha(\mathbf{p}_1, \mathbf{p}_2) + \frac{2}{7}\beta(\mathbf{p}_1, \mathbf{p}_2), \quad (3.23a)$$

$$G_2(\mathbf{p}_1, \mathbf{p}_2) = \frac{3}{7}\alpha(\mathbf{p}_1, \mathbf{p}_2) + \frac{4}{7}\beta(\mathbf{p}_1, \mathbf{p}_2). \quad (3.23b)$$

Continuing along these lines to higher and higher order, we find the general expression

$$F_n(\mathbf{p}_1, \dots, \mathbf{p}_n) = \sum_{m=1}^{n-1} \frac{G_m(\mathbf{p}_1, \dots, \mathbf{p}_m)}{(2n+3)(n-1)} [(2n+1)\alpha(\mathbf{p}_{1\dots m}, \mathbf{p}_{m+1\dots n})F_{n-m}(\mathbf{p}_{m+1}, \dots, \mathbf{p}_n)] \\ + 2\beta(\mathbf{p}_{1\dots m}, \mathbf{p}_{m+1\dots n})G_{n-m}(\mathbf{p}_{m+1}, \dots, \mathbf{p}_n), \quad (3.24a)$$

$$G_n(\mathbf{p}_1, \dots, \mathbf{p}_n) = \sum_{m=1}^{n-1} \frac{G_m(\mathbf{p}_1, \dots, \mathbf{p}_m)}{(2n+3)(n-1)} [3\alpha(\mathbf{p}_{1\dots m}, \mathbf{p}_{m+1\dots n})F_{n-m}(\mathbf{p}_{m+1}, \dots, \mathbf{p}_n)] \\ + 2n\beta(\mathbf{p}_{1\dots m}, \mathbf{p}_{m+1\dots n})G_{n-m}(\mathbf{p}_{m+1}, \dots, \mathbf{p}_n). \quad (3.24b)$$

A list of higher-order kernels can be found in [19]. For more details on the derivation of Eq. (3.24), refer to [55, 59]. Eqs. (3.22) and (3.24) together provide a method to describe the nonlinear evolution and the formation of structure. They also equip us with the tools necessary to calculate the statistics of the nonlinear density field at arbitrary order, expressed in terms of the statistics of the linear density field. The equal time power spectrum of  $\delta(\mathbf{k})$  can be written as

$$P^{\text{SPT}}(k, \eta) = D^2(\eta)P^{(11)}(k) + D^4(\eta) [2P^{(13)}(k) + P^{(22)}(k)] + \dots \quad (3.25)$$

The first term contains the linear contributions, while the second term contains the leading-order nonlinear correction to the linear matter power spectrum. Notice that we have dropped the terms which contain an uneven number of  $\delta_L$  since they vanish due to  $\delta_L$  being a Gaussian field. However, one of the effects of nonlinear corrections is that the terms containing an uneven number of evolved matter density field will no longer be zero. As an example of this, we take the bispectrum which is at the lowest order given by

$$\mathcal{B}(\mathbf{k}_1, \mathbf{k}_2, \mathbf{k}_3, \eta) \equiv \langle \delta(\mathbf{k}_1, \eta)\delta(\mathbf{k}_2, \eta)\delta(\mathbf{k}_3, \eta) \rangle' \\ = D^4(\eta)(2F_2(\mathbf{k}_1, \mathbf{k}_2)P_L(k_1)P_L(k_2) + 2 \text{ perms}). \quad (3.26)$$

## 3.2 Effective Field Theory of Large Scale Structure

Problems with SPT start to arise when we look at the so-called loop contributions. Those are the nonlinear corrections that contain an integral over the moment. Let us for example take a look at the  $P_{13}(k)$  term

$$P_{13}(k) = 3P_L(k) \int_{\mathbf{p}} F_3(\mathbf{k}, \mathbf{p}, -\mathbf{p})P_L(p). \quad (3.27)$$

If we now let  $p \rightarrow \infty$  and use the fact that in this limit  $F_3 \rightarrow k^2/p^2$ , we will get the following integral:

$$P_{13}(k) \xrightarrow{p \rightarrow \infty} P_L(k)k^2 \int_0^\infty p^2 dp \frac{P_L(p)}{p^2}. \quad (3.28)$$

Here we are integrating over *initial* perturbations which are Gaussian with power spectrum  $P_L(p)$ . From Eq. (3.28), it is evident that contributions from arbitrarily small scales are

being included in our calculations. As  $p \rightarrow \infty$ , we probe progressively smaller scales, moving from the scale of galaxy clusters down to scales comparable to everyday objects. Since Standard Perturbation Theory (SPT) becomes unreliable on such small scales, it becomes necessary to regulate the scales considered in our analysis. Fortunately, the Effective Field Theory of Large Scale Structure (EFTofLSS) provides a perturbative framework to address this issue. The following section will focus on this approach, drawing primarily from Sec. 3 of [13], as well as from [17, 31, 32].

The central concept of EFTofLSS is the introduction of a cut-off scale,  $\Lambda$ , which represents the maximum wavenumber of the modes considered in the calculations. While the exact value of  $\Lambda$  is arbitrary, its upper limit in EFTofLSS corresponds to the nonlinearity scale—the scale at which perturbation theory breaks down. This nonlinearity scale can be estimated by calculating the variance of density perturbations:

$$\Sigma_\Lambda^2(a) = \frac{1}{2\pi^2} \int_0^\Lambda d \ln q q^3 P_{\text{lin}}(q, a) \approx \frac{\Lambda^3 P_{\text{lin}}(\Lambda, a)}{2\pi^2}. \quad (3.29)$$

Notice we apply the cutoff to the *linear* density field. When  $\Sigma_\Lambda^2 \ll 1$ , perturbations are small, and PT theory holds. However, when  $\Sigma_\Lambda^2 \gtrsim 1$ , perturbations become large, and non-linearities dominate. By setting  $\Sigma_\Lambda^2 \approx 1$ , we can determine the nonlinearity scale. For the present-day universe ( $a = 1$ ), this scale is approximately  $\Lambda_{\text{NL}} \approx 0.25 h\text{Mpc}^{-1}$ . As we look further back in time, structures are less evolved, and the nonlinearity scale increases.

### 3.2.1 Equations of Motion in EFT

The starting point of EFTofLSS is to integrate out all the modes below  $\Lambda$  (short-wavelength modes) which will leave us with the long-wavelet theory with all the modes above  $\Lambda$ . This procedure is known as *coarse graining*. Integrating out small-scales in real space corresponds to a convolution of fields with a window function  $W_\Lambda$

$$D_\Lambda(\mathbf{x}) = \int_{\mathbf{y}} W_\Lambda(|\mathbf{x} - \mathbf{y}|) D(\mathbf{x}), \quad (3.30)$$

which in Fourier space reduces to multiplication

$$D_\Lambda(\mathbf{k}) = W_\Lambda(\mathbf{k}) D(\mathbf{k}). \quad (3.31)$$

The window function is normalized such that  $W_\Lambda(k=0) = \int d^3x W_\Lambda(x) \equiv 1$ . We split all the relevant physical quantities into long-wavelet modes and short-wavelength modes

$$D = D_l + D_s. \quad (3.32)$$

In the simplest case when dealing with a single operator,  $D_l = D_\Lambda$  and  $D_s$  is given by

$$D_s(\mathbf{k}) = (1 - W_\Lambda(\mathbf{k})) D(\mathbf{k}). \quad (3.33)$$

We introduce the filtered density and momentum as

$$\begin{aligned}\rho_l &= \int_p f_l(\mathbf{x}, \mathbf{p}, \eta), \\ \pi_l &= \rho_l \mathbf{v}_l = \frac{m}{a^3} \int_p \frac{\mathbf{p}}{ma} f_l(\mathbf{x}, \mathbf{p}, \eta).\end{aligned}\tag{3.34}$$

Finally, to find the equations of motion in Effective Field Theory (EFT), we start again from the set of equations in (3.18) and apply smoothing. This procedure leads us to the following set:

$$\dot{\delta}_l + \theta_l = -\delta_l \theta_l - \mathbf{u}_l \nabla \delta_l,\tag{3.35a}$$

$$\dot{\theta}_l + \mathcal{H} \theta_l + \nabla^2 \Psi_l = -\mathbf{u}_l \nabla \theta_l - \nabla(\mathbf{u}_l \nabla) \mathbf{u}_l - \frac{1}{\rho} \nabla \tau_{\Lambda, UV},\tag{3.35b}$$

Notice the additional term  $\tau_{\Lambda, UV}$  which captures the influence of small-wavelength fluctuations on the large-wavelength modes. It arises because the smoothing of the fields and their multiplication do not commute. In other words, a smoothed product of two fields is different from the product of two smoothed fields. This difference occurs because the smoothed product of the fields contains additional terms arising from the small-scale modes.

The full form of  $\tau$  has been derived in the Appendix A of [17]

$$\tau_{\Lambda, UV}^{ij} = \rho u_s^i u_s^j + \frac{1}{4\pi G} \left( \partial^i \Psi_s \partial^j \Psi_s - \frac{1}{2} \delta^{ij} \partial_k \Psi_s \partial^k \Psi_s \right).\tag{3.36}$$

These small-scale perturbations are very large, making it impossible to describe their exact behavior within perturbation theory. To still be able to make meaningful predictions about their influence, we work with the expectation value of these modes on a long-wavelength background. Since this way the result depends only on the large scale perturbations, which are small, we can use Taylor expansion to write [31]

$$\tau_{\Lambda, UV}^{ij} \equiv \langle \tau_{\Lambda, UV}^{ij} \rangle_{\delta_l} = \langle \tau_{\Lambda, UV}^{ij} \rangle_{\delta_l=0} + \frac{\partial \langle \tau_{\Lambda, UV}^{ij} \rangle}{\partial \delta_l} + \dots\tag{3.37}$$

The result will be the stress tensor of an imperfect fluid. From the RHS of Eq. (3.35b) it is clear that we need the divergence of  $\tau_{\Lambda, UV}$ , which to linear order equals to

$$\begin{aligned}\nabla \left( \frac{1}{\rho_\Lambda} \nabla \tau_{\Lambda, UV} \right) &= \tilde{c}_{s, \Lambda}^2 \nabla^2 \delta_\Lambda - \frac{1}{\mathcal{H}} \left( \tilde{c}_{v, s, \Lambda}^2 + \tilde{c}_{v, b, \Lambda}^2 \right) \nabla^2 \theta_\Lambda + \Delta \tau_{\epsilon, m} \\ &= \left[ \tilde{c}_{s, \Lambda}^2 + f(\eta) (\tilde{c}_{v, s, \Lambda}^2 + \tilde{c}_{v, b, \Lambda}^2) \right] \nabla^2 \delta_\Lambda + \Delta \tau_{\epsilon, m},\end{aligned}\tag{3.38}$$

where  $c_{s, \Lambda}^2$  represents the sound speed. The terms  $c_{v, b, \Lambda}^2$  and  $c_{v, s, \Lambda}^2$  correspond to the bulk and shear viscosities, respectively. The coefficients  $c_{s, \Lambda}^2$ ,  $c_{v, b, \Lambda}^2$ , and  $c_{v, s, \Lambda}^2$  are all sourced by small-scale effects. The EFTofLSS cannot predict their values. Instead, these values need

to be determined either from N-body simulations or from observations. The term  $\Delta\tau_{\epsilon,m}$  represents the stochastic contribution, capturing the discrepancy between the expectation values and the actual realizations. The stochastic contribution arises from integrating out modes below  $\Lambda$ . Since this contribution is the result of the superposition of many independent modes, the central limit theorem ensures that the stochastic field is Gaussian to the leading order. Additionally, due to the local nature of tracer formation, its power spectrum is constant at the leading order, with corrections scaling as  $k^2$ .

### 3.2.2 EFT Power spectrum and renormalization

Once the divergence of the stress tensor has been found in (3.38), all the necessary components are in place to solve the EFTofLSS equations from (3.35b). The process of solving these equations follows a similar approach as in Standard Perturbation Theory (SPT). Further details can be found in [31]. Here, we will simply present the solution for the 1-loop power spectrum.

$$P_{1\text{-loop}}^\Lambda(k, \eta) = D^2(\eta)P_L(k) + D^4(\eta)\left[2P_\Lambda^{13}(k) + P_\Lambda^{22}(k)\right] - 2c_{s,\Lambda}^2(\eta)D^2(\eta)k^2P_L(k) + D^4(\eta)P_{\tau_{\epsilon,m}\tau_{\epsilon,m},\Lambda}(k), \quad (3.39)$$

where we have defined  $c_{s,\Lambda}^2 = \tilde{c}_{s,\Lambda}^2 + f(\eta)(\tilde{c}_{v,s,\Lambda}^2 + \tilde{c}_{v,b,\Lambda}^2)$ . When introducing the cut-off scale  $\Lambda$ , we emphasized that our results should not depend on it, as  $\Lambda$  is simply a tool used to address issues in perturbation theory and carries no physical meaning. At first glance, the 1-loop power spectrum might seem problematic, as it includes terms that explicitly depend on  $\Lambda$ . However, upon closer inspection, it becomes clear that all contributions involving  $\Lambda$  cancel out.

Specifically, the  $\Lambda$ -dependent contributions in  $P_\Lambda^{13}$  exactly cancel out with those in  $c_{s,\Lambda}^2$ . Similarly, the cut-off dependency in  $P_\Lambda^{22}$  cancels with the one in the stochastic contribution  $P_{\tau_{\epsilon,m}\tau_{\epsilon,m},\Lambda}$ , rendering  $P_{1\text{-loop}}^\Lambda$  free from any explicit dependence on  $\Lambda$ . A detailed derivation of these cancellations can be found in [13].

This cancellation is not limited to the 1-loop power spectrum; it can be extended to any n-point function of interest (for some examples see [8, 20, 131]). The theoretical framework behind the removal of divergences is called *renormalization*. Renormalization is a procedure that is not specific to EFTofLSS and it has been widely spread in quantum field theories for decades (see for example [100, 143]). For a deeper understanding of renormalization in the context of EFTofLSS, one may refer to [1, 17, 31].

## 3.3 Lagrangian Perturbation Theory

In the previous sections, we have discussed Standard Perturbation Theory (SPT), where the perturbation variables were matter overdensity and bulk velocity, both expressed in Eulerian space. An alternative approach to this method is Lagrangian Perturbation Theory (LPT) [25–27, 34, 35, 47, 79, 86, 106, 109, 139], in which all perturbation variables are expressed

in the frame of the fluid (Lagrangian space). One significant advantage of LPT is that it converges faster and agrees better with the fully nonlinear density field compared to SPT [133, 134]. Furthermore, as we will see in later chapters, implementing the general bias expansion is much simpler in LPT than in the Eulerian case.

The LPT description tracks the fluid element displacement from its initial Lagrangian position  $\mathbf{q}$  to its final Eulerian position  $\mathbf{x}$  using the displacement vector  $\boldsymbol{\psi}(\mathbf{q}, \eta)$ :

$$\mathbf{x}(\eta) = \mathbf{q} + \boldsymbol{\psi}(\mathbf{q}, \eta). \quad (3.40)$$

From Eq. (3.40), it is straightforward to find the Jacobian  $\mathcal{J}$  of this coordinate transformation

$$\mathcal{J} = \left| \frac{d^3x}{d^3q} \right| = \det(\mathbb{I}_{ij} + \partial_{q,i}\psi_j). \quad (3.41)$$

Mass conservation provides the change in matter density between the coordinates:

$$1 + \delta(\mathbf{x}) = 1/\mathcal{J}. \quad (3.42)$$

To find the perturbative solution in LPT we treat the components of the displacement vector as small parameters, which allows us to write

$$\boldsymbol{\psi}(\mathbf{q}, \eta) = \sum_{n=1}^{\infty} \boldsymbol{\psi}^{(n)}(\mathbf{q}, \tau). \quad (3.43)$$

Furthermore, it is convenient to use the standard vector calculus result, which allows us to separate the displacement field into its curl-free and divergence-free components:

$$\boldsymbol{\psi}(\mathbf{q}, \tau) = \frac{\nabla}{\nabla^2}\sigma - \frac{1}{\nabla^2}\nabla \times \boldsymbol{\xi}, \quad (3.44)$$

where  $\sigma \equiv \nabla \cdot \boldsymbol{\psi}$  is the divergence of the displacement, while  $\boldsymbol{\xi} = \nabla \times \boldsymbol{\psi}$  is the displacement's curl. This separation is useful because it allows us to derive recursion relations for the solutions of  $\sigma$  and  $\boldsymbol{\xi}$ , and consequently for  $\boldsymbol{\psi}$ , at any desired order in PT [80, 106, 150].

A recursive solution can be obtained for any expansion history, provided it begins from an initial epoch of matter domination [47, 109]. Such solutions keep only the fastest-growing mode; however, in more general cosmologies, other modes may become significant and cannot be neglected. If another component, such as radiation, dominates, perturbations in that component must also be considered, rendering the original equation of motion invalid, which is why the initial condition of matter domination is necessary. Nonetheless, by employing the Einstein-de Sitter (EdS) approximation and neglecting the curl component, the problem becomes significantly simpler. The price we pay for this approximation is very low since the curl component only enters into consideration at the third order, and the error introduced by using EdS instead of  $\Lambda$ CDM is below one percent [109].

To derive the equation that governs the evolution of the displacement vector, we begin with the equation that describes the evolution of the cosmological fluid in the Newtonian limit:

$$\frac{d^2\mathbf{x}}{d\eta^2} + \mathcal{H}\frac{d\mathbf{x}}{d\eta} = -\nabla\Psi, \quad (3.45)$$

where  $\Psi$  is the gravitational potential, and its evolution is governed by the Poisson equation

$$\nabla^2 \Psi = \frac{3}{2} \mathcal{H}^2 \Omega_m(\eta) \delta. \quad (3.46)$$

If we take the divergence of Eq. (3.45) and combine it with the Poisson equation, we get

$$\nabla_{\mathbf{x}} \left[ \frac{d^2 \mathbf{x}}{d\eta^2} + \mathcal{H} \frac{d\mathbf{x}}{d\eta} \right] = \frac{3}{2} \Omega_m \mathcal{H}^2 (\mathcal{J}^{-1} - 1), \quad (3.47)$$

where we have used the Eq. (3.42) to connect the matter density and Jacobian. This equation was first derived in [44].

To fully express the equation in terms of Lagrangian coordinates, we use the relation  $\nabla_{\mathbf{x}} = \mathcal{J}^{-1} \nabla_{\mathbf{q}}$ , where  $\mathcal{J}$  is the Jacobian. Additionally, to solve the equation perturbatively, we need to expand the Jacobian

$$\mathcal{J} = 1 + \mathcal{J}^{(1)} + \mathcal{J}^{(2)} + \mathcal{J}^{(3)} + \dots \quad (3.48)$$

At first order, we have

$$\mathcal{J}^{(1)} = \sum_i \partial_{q^i} \nabla \psi_i^{(1)} = \sigma^{(1)}. \quad (3.49)$$

This leads us to the following differential equation for  $\sigma^{(1)}$

$$\left( \frac{d^2}{d\eta^2} + \mathcal{H} \frac{d}{d\eta} - \frac{3}{2} \Omega_m \mathcal{H}^2 \right) \sigma^{(1)} = 0. \quad (3.50)$$

Here we recognize the linear equation that we have already encountered in Eq. (3.11). As in the previous case, we will keep only the growth mode and disregard the decaying one. From Eq. (3.42) and Eq. (3.12), we find

$$\psi^{(1)}(\mathbf{k}, \eta) = i \frac{\mathbf{k}}{k^2} \delta_L(\mathbf{k}) D(\eta). \quad (3.51)$$

This solution is known as Zel'dovich approximation [149]. Despite its simplicity, the Zel'dovich approximation provides accurate predictions for the early nonlinear stages of gravitational collapse and compares quite well with respect to the full N-body solution [24, 144].

To proceed to higher orders, we exploit the fact that in the EdS approximation higher orders of the growth factor are simply powers of  $a$  so derivatives of  $\psi$  are given by

$$\frac{d^2 \psi^{(n)}}{da^2} = \frac{n(n-1)}{a^2} \psi^n, \quad \frac{d\psi^{(n)}}{da} = \frac{n}{a} \psi^n. \quad (3.52)$$

This brings us to the  $n$ -th order equation

$$\mathcal{J}(\mathbb{I} + \partial_{\mathbf{q}} \psi)^{-1} \left[ n^2 + \frac{n}{2} \right] \mathcal{H}^2 \psi_{i,j}^{(n)} = \frac{3}{2} \mathcal{H}^2 (\mathcal{J} - 1). \quad (3.53)$$

To solve this equation at the desired order, one would have to proceed in the similar manner as we did for the first order by expanding both  $\mathcal{J}$  and  $\psi$  to the desired order and then integrating to find the solution. We will not be giving more details here, but interested reader may refer to Appendix A of [109] to find the recursion formula for all orders of  $\sigma$  and  $\xi$  for all order solutions in EdS approximation.

Once we have found the displacement at the desired order, we can easily find the final overdensity

$$\delta(\mathbf{k}) = \int_{\mathbf{x}} e^{-i\mathbf{k}\cdot\mathbf{x}} \delta(\mathbf{x}) = \int_{\mathbf{q}} e^{-i\mathbf{k}\cdot\mathbf{q}} \left( e^{-i\mathbf{k}\cdot\psi(\mathbf{q})} - 1 \right). \quad (3.54)$$

Expanding this equation, we can see that SPT and LPT are equivalent order by order in the region of validity of both theories [24].

Finally, let us note that although LPT is not limited by the condition of small overdensity, it still has a point where it breaks down. LPT primarily fails at the point of shell crossing. This occurs when different layers or shells of matter, initially described by smooth trajectories, start to overlap due to gravitational collapse. Additionally, LPT suffers from treating nonlinear scales as perturbative. Similarly to SPT, these limitations can be addressed using techniques from effective field theory, where we solve the equations that depend only on the smoothed fields. This approach introduces counterterms that represent the effects of small-scale physics not described by the smoothed theory and absorb all the cut-off dependent terms of the theory. For more details on EFTofLSS techniques for LPT, refer for example to [104, 138, 139, 148].

# Chapter 4

## From evolved matter to biased tracers

In the previous chapter, we discussed the evolution of the matter density field from the initial conditions set by inflation to the late-time matter distribution. However, the matter density field itself is not directly observable. Instead, we observe the positions of so-called biased tracers of the matter density field, such as halos, galaxies, and galaxy clusters. By measuring their number density in different regions of the universe and comparing it to their average density, we can determine the tracer overdensity:

$$\delta_g(\mathbf{x}, \eta) \equiv \frac{n_g(\mathbf{x}, \eta)}{\bar{n}_g(\eta)} - 1. \quad (4.1)$$

Here,  $n_g(\mathbf{x}, \eta)$  denotes the comoving rest-frame tracer density, and  $\bar{n}_g(\eta)$  is its position-independent mean.

The key question we aim to answer in this section is how to connect the tracer density to the matter density. On very large scales, we can use a linear approximation [66]:

$$\delta_g(\mathbf{x}, \eta) \approx b_1 \delta(\mathbf{x}, \eta), \quad (4.2)$$

where  $b_1$  is an unknown coefficient referred to as the *bias*. However, this linear approximation breaks down at smaller scales, where non-linearities must be accounted for. To describe this non-linear relationship, we will rely on the EFTofLSS. Details of this theory can be found in various sources. This chapter draws mainly from the following key references: [42, 82, 101, 118].

### 4.1 General Bias Expansion

The simplest way we can approach the bias problem is to assume that  $\delta_g(\mathbf{x}, \eta)$  is a local function of  $\delta(\mathbf{x}, \eta)$ . We can formally write this connection as a Taylor expansion

$$\delta_g(\mathbf{x}, \eta) = \sum_{n=1}^{\infty} \frac{b_n(\eta)}{n!} [\delta_\Lambda(\mathbf{x}, \eta)]^n, \quad (4.3)$$

where  $b_n(\eta)$  are the bias coefficients and  $\delta_\Lambda$  is the matter density field smoothed on a scale  $\Lambda$ . The smoothing is applied to ensure that only contributions from scales under perturbative control are considered. The role of the bias coefficients is to encapsulate our ignorance of small scales, as we cannot predict their values but must measure them from N-body simulations or observations. This kind of bias expansion is called *local-in-matter-density bias expansion*. However, it is incomplete, since  $\delta_g$  may depend on  $\delta$  in more complex ways than a straightforward power expansion. One such example would be tidal field  $K_{ij}$ , defined as:

$$K_{ij}(\mathbf{x}, \eta) \equiv \left( \frac{\partial_i \partial_j}{\nabla^2} - \frac{1}{3} \delta_{ij} \right) \delta(\mathbf{x}, \eta). \quad (4.4)$$

Furthermore, the dark matter fluid has been described in terms of both the density field  $\delta$  and the velocity field  $u^i$ , making it possible for  $\delta_g$  to also depend on scalars constructed from  $u^i$ . Therefore, we will introduce a more general expansion for the tracer density field in terms of operators  $O$ , which are called *bias operators*:

$$\delta_g(\mathbf{x}, \eta) = \sum_O b_O(\eta) O(\mathbf{x}, \eta). \quad (4.5)$$

This expansion makes no assumptions about the underlying physics of tracer formation; instead, all information about small-scale effects is captured in the bias coefficients. The choice of operators  $\{O\}$  to include in the expansion is determined by the symmetries of the problem. Tracer formation occurs over very long time scales [83] and in very small spatial regions [39], on the order of a few Mpc. The scale of the region involved in tracer formation is characterized by the comoving length scale  $R_*$ , known as the *non-locality scale*. We will assume that we are working with scales much larger than  $R_*$ , which allows us to approximate the bias relation as local in space. According to the equivalence principle, the leading observable is the second derivative of the Newtonian potential,  $\partial_i \partial_j \Phi$ . Therefore, all bias operators  $\{O\}$  must be constructed using the Newtonian potential and at least two derivatives. Additionally, the trace part of this tensor can be related to  $\delta$  through the Poisson equation, while the traceless part is represented by the tidal tensor  $K_{ij}$ . Another local observable we can use to construct the bias operators is the derivative of  $u_i$ . Furthermore, we will assume that there is no velocity bias, meaning that the tracer velocity is equal to the matter velocity  $\mathbf{u}_g = \mathbf{u}$ . This is guaranteed by the equivalence principle for velocities induced by gravity; only baryonic pressure forces can produce a velocity bias.

We have already mentioned that the formation of halos is not local in time as it happens over a large fraction of the age of the Universe. This means that  $\delta_g$  does not depend only on  $\eta$ , instead it needs to be integrated over the entire past geodesic of the fluid [118]. For a case in which a single bias operator is involved, this implies

$$\delta_g(\mathbf{x}, \eta) \supset \int_{\eta_{\text{in}}}^{\eta} d\eta' f_O(\eta', \eta) O(\mathbf{x}(\eta'), \eta'), \quad (4.6)$$

where  $\mathbf{x}(\eta')$  are positions of the fluid element for  $\eta' < \eta$  and  $\mathbf{x} = \mathbf{x}(\eta)$ . We can further use

the Taylor expansion in time of the operator  $O$

$$O(\mathbf{x}(\eta'), \eta') = \sum_{n=0}^{\infty} \frac{1}{n!} (\eta - \eta') \frac{D^n}{D\eta^n} O(\mathbf{x}(\eta), \eta), \quad (4.7)$$

where  $D/D\eta$  is the convective derivative along the fluid flow, defined as

$$\frac{D}{D\eta} \equiv \frac{\partial}{\partial \eta} + \mathbf{u} \cdot \nabla. \quad (4.8)$$

This step allowed us to remove all the dependence on  $\eta'$  from the operators  $O$  and move it into coefficients instead

$$\delta_g(\mathbf{x}, \eta) \supset \sum_n \left( \int_{\eta_{\text{in}}}^{\eta} d\eta' f_O(\eta', \eta) \frac{1}{n!} (\eta - \eta') \right) \frac{D^n}{D\eta^n} O(\mathbf{x}(\eta), \eta). \quad (4.9)$$

However, we see that to account for the time non-locality, we also need to include the time derivatives along the fluid flow.

Therefore, the operators in Eq. (4.5) can be constructed using combinations of  $\partial_i \partial_j \Phi$ , and their time derivatives. At each order of the expansion, we obtain a finite set of independent operators  $O$ . These sets are referred to as the basis of the bias expansion, and their selection is not unique. In the following sections, we will employ the basis constructed from operators in the Lagrangian frame (Lagrangian bias) as well as the basis constructed using operators at the time of observation (Eulerian bias). In the sections below, we will discuss each of these two sets of bases in more detail.

## 4.2 Lagrangian Bias Expansion

In the Lagrangian frame, the basis can be conveniently constructed using the Lagrangian deformation tensor, defined as:

$$M_{ij}(\mathbf{q}, \eta) \equiv \partial_{q,i} \psi_j(\mathbf{q}, \eta). \quad (4.10)$$

The components of  $M_{ij}$  can be treated as small perturbative parameters, allowing for an expansion as:

$$M_{ij}(\mathbf{q}, \eta) = \sum_n M_{ij}^{(n)}(\mathbf{q}, \eta). \quad (4.11)$$

These components can be determined iteratively using a recursion relation. The starting point for this relation is given by [109]:

$$M_{ij}^{(1)}(\mathbf{q}, \eta) = \frac{\partial_{q,i} \partial_{q,j}}{\nabla_q^2} \delta^{(1)}(\mathbf{q}, \eta), \quad (4.12)$$

where  $\delta^{(1)}(\mathbf{q}, \eta)$  represents the first-order density perturbation.

In the following, we omit the time argument for clarity. It is easy to show that we can express all local observables in terms of  $M_{ij}$  [82, 150]. For example, if we want to express  $\partial u_i(\mathbf{x})/\partial x_j$  in terms of  $M_{ij}(\mathbf{q})$ , we would start from the relation

$$u_i(\mathbf{x}) = \frac{ds_i(\mathbf{q})}{d\eta} \equiv \dot{s}_i(\mathbf{q}). \quad (4.13)$$

If we take derivative  $\partial_j$  of this relation, we get

$$\frac{\partial u_i(\mathbf{x})}{\partial x_j} = \frac{\partial q_k}{\partial x_j} \frac{\partial \dot{s}_i(\mathbf{q})}{\partial q_k} \quad (4.14)$$

Using the relation

$$\frac{\partial q_k}{\partial x_j} = \epsilon_{kmn} \epsilon_{jpl} \frac{1}{2\mathcal{J}} \frac{\partial x_p}{\partial q_n} \frac{\partial x_l}{\partial q_m}, \quad (4.15)$$

and exploiting the fact that  $\frac{\partial x_l}{\partial q_m} = \delta_{lm} + M_{lm}(\mathbf{q})$ , we find that  $\partial_j u_i(\mathbf{x})$  can fully be expressed in terms of  $M_{ij}(\mathbf{q})$  and its time derivative:

$$\frac{\partial u_i(\mathbf{x})}{\partial x_j} = \frac{\epsilon_{kmn} \epsilon_{jpl}}{2\mathcal{J}} [\delta_{pn} + M_{pn}(\mathbf{q})] [\delta_{lm} + M_{lm}(\mathbf{q})] \dot{M}_{ik}(\mathbf{q}). \quad (4.16)$$

A similar procedure can be applied to other local observables. Therefore, it makes sense to choose  $M$  as the building block of the bias basis. Furthermore, since the bias basis needs to be built out of scalars, we will work with trace of powers of  $M$ . In that case, we can write the galaxy density as

$$\delta_g^L = \sum_{O_L} b_{O}(\eta) O_L(\mathbf{q}, \eta), \quad (4.17)$$

where operators  $O_L$  are Lagrangian operators built out of different combinations of  $\text{tr}M$  and its covariant derivative  $D/D\eta$  ( $\text{tr}M$ ). In Lagrangian space, this simplifies a bit since convective derivatives reduce to partial derivatives  $d/d\eta$ .

To build a better intuition about these operators, let us take a closer look at one of the, for example  $O_L = \text{tr}M^2$ .

$$\text{tr}M^2(\mathbf{q}, \eta) = \text{tr} [M(\mathbf{q}, \eta)M(\mathbf{q}, \eta)] \quad (4.18a)$$

$$= \text{tr} [(M^{(1)}(\mathbf{q}, \eta) + M^{(2)}(\mathbf{q}, \eta) + \dots)(M^{(1)}(\mathbf{q}, \eta) + M^{(2)}(\mathbf{q}, \eta) + \dots)] \quad (4.18b)$$

$$= \text{tr} [M^{(1)}(\mathbf{q}, \eta)M^{(1)}(\mathbf{q}, \eta)] + 2\text{tr} [M^{(1)}(\mathbf{q}, \eta)M^{(2)}(\mathbf{q}, \eta)] + \dots, \quad (4.18c)$$

where to get from the first to the second line, we used the expansion for  $M$  defined in Eq. (4.11). We can simplify things further by using the fact that  $M(\mathbf{q}, \eta)$  can be written as:

$$M(\mathbf{q}, \eta) = \sum_{n=0}^{\infty} D^n(\eta) M^{(n)}(\mathbf{q}). \quad (4.19)$$

Here  $D(\eta)$  is the linear growth factor normalized to some  $\eta_0$ . Operator  $M^{(n)}$  represents the  $n$ -th order contribution to  $M(\mathbf{x}, \eta)$  evaluated at some reference time  $\eta_0$ . We have also used the EdS approximation in assuming that  $n$ -th order of the growth factor is given as powers of the linear growth factor. By employing Eq. (4.19), we can express  $\text{tr}M^2(\mathbf{q}, \eta)$  as:

$$\text{tr}M^2(\mathbf{q}, \eta) = D^2(\eta)\text{tr}[M^{(1)}(\mathbf{q})M^{(1)}(\mathbf{q})] + 2D^3(\eta)\text{tr}[M^{(1)}(\mathbf{q})M^{(2)}(\mathbf{q})] + \dots \quad (4.20)$$

Thus, the operator  $\text{tr}M^2$  contains terms that are second order in perturbation and higher. A similar result can be derived for other bias operators, allowing us to generally express:

$$O_L(\mathbf{q}, \eta) = \sum_{n=0}^{\infty} D^{d_O+n}(\eta)O_L^{(d_O+n)}(\mathbf{q}). \quad (4.21)$$

We have constructed this in such way that  $d_O$  is the perturbative order of the leading contribution to  $O_L$ .

From Eq. (4.21) it is evident that the time derivative of any operator  $O_L$  is a linear combination of the operators  $O_L^m$  with  $m \leq n$ . Therefore, in constructing the Lagrangian basis, we need to count all the distinct scalars that can be formed using  $\text{Tr}(M)$ . This task is simplified by the fact that any terms involving  $\text{Tr}(M^{(n)})$  for  $n > 1$  can be expressed in terms of lower-order operators. Additionally, only the symmetric part of the displacement field derivative needs to be considered, as the anti-symmetric part can be expressed through the symmetric component [80, 150].

The Lagrangian bias basis up to the 4th order is [42]:

$$\begin{aligned} 1^{\text{st}} & \text{tr}[M^{(1)}] \\ 2^{\text{nd}} & \text{tr}[(M^{(1)})^2], \quad (\text{tr}[M^{(1)}])^2 \\ 3^{\text{rd}} & \text{tr}[(M^{(1)})^3], \quad (\text{tr}[(M^{(1)})^2]\text{tr}[M^{(1)}]), \quad (\text{tr}[M^{(1)}])^3, \quad \text{tr}[M^{(1)}M^{(2)}] \\ 4^{\text{th}} & \text{tr}[(M^{(1)})^4], \quad (\text{tr}[(M^{(1)})^2])^2, \quad (\text{tr}[(M^{(1)})^3]\text{tr}[M^{(1)}]), \quad (\text{tr}[(M^{(1)})^2]\text{tr}[(M^{(1)})^2]), \\ & \text{tr}[M^{(1)}]\text{tr}[M^{(2)}], \quad \text{tr}[M^{(1)}M^{(3)}], \quad \text{tr}[M^{(2)}M^{(2)}]. \end{aligned} \quad (4.22)$$

The operators listed here are derived using the EdS (Einstein-de Sitter) approximation. As shown in Appendix B.6 of [42], deviations from  $\Lambda$ CDM operators only begin to appear at fourth order. Since our calculations are limited to operators up to third order, the EdS approximation is sufficient for our purposes. However, an interested reader can find a more general list of operators and their derivation in [109].

### 4.3 Eulerian Bias Expansion

Eulerian basis for bias expansion is constructed using operators at the observation time. As the main building block of the Eulerian basis, we introduce the tensor

$$\Pi_{ij}^{[1]}(\mathbf{x}, \eta) = \frac{2}{3\Omega_m(\eta)\mathcal{H}^2(\eta)}\partial_i\partial_j\Phi(\mathbf{x}, \eta), \quad (4.23)$$

which can be used to find all the basis elements [42,61,74]. It is easy to see that  $\Pi_{ij}^{[1]} = \delta^{(1)}$ . The procedure is now similar to the Lagrangian case, one needs to find all the independent scalar that can be constructed from  $\Pi_{ij}^{[1]}$ . Higher order terms can be constructed using the recursion relation

$$\Pi_{ij}^{[n]} = \frac{1}{(n-1)!} \left[ (\mathcal{H}f)^{-1} \frac{D}{D\eta} \Pi_{ij}^{[n-1]} - (n-1)\Pi_{ij}^{[n-1]} \right]. \quad (4.24)$$

$\Pi_{ij}^{[n]}$  contains perturbative terms of order  $n$  and higher. Using Eq. (4.9), we demonstrated that to address the lack of time locality, it is necessary to include both the bias operators and their convective derivatives to construct a complete basis for bias expansion. The basis formed using  $\Pi_{ij}^{[n]}$  is complete because, at  $n$ -th order in perturbation theory,  $\Pi_{ij}^{[1]}$  depends on time through only  $n$  quantities:  $D(\eta), D^2(\eta), \dots, D^n(\eta)$ . Consequently, any higher-order convective time derivative  $D^m/D\eta^m$  with  $m > n$  can be expressed in terms of lower-order derivatives, starting from the first to the  $n$ -th derivative, when neglecting terms of higher than  $n$ -th order in perturbation theory. This result is analogous to what we observed with Lagrangian operators, although in the Lagrangian frame, the convective derivatives simplify to ordinary time derivatives, making the situation more intuitive.

Using all the combination of these tensors, we find the Eulerian basis up to the third order

$$\begin{aligned} \text{1st} & \quad \text{tr} [\Pi^{(1)}] \\ \text{2nd} & \quad \text{tr} [(\Pi^{(1)})^2], (\text{tr} [\Pi^{(1)}])^2 \\ \text{3rd} & \quad \text{tr} [(\Pi^{(1)})^3], \text{tr} [(\Pi^{(1)})^2] \text{tr} [\Pi^{(1)}], (\text{tr} [\Pi^{(1)}])^3, \text{tr} [\Pi^{(1)}\Pi^{(2)}] \end{aligned} \quad (4.25)$$

We listed bias operators only up to the third order; however, we can continue using the recursion relation to find higher-order operators.

Although this basis is complete, it does not offer an intuitive physical interpretation of the bias terms. Luckily, we can connect this to a basis that is constructed from matter density field  $\delta$  and tidal field. To complete this basis, at the third order, we need to introduce an additional operator

$$O_{\text{td}}^{(3)} \equiv \frac{8}{21} K_{ij}^{(1)} D^{ij} \left[ (\delta^{(1)})^2 - \frac{3}{2} (K^{(1)})^2 \right]. \quad (4.26)$$

We define the relationship between two basis to be [82]

$$\begin{aligned} K_{ij}(\mathbf{x}, \eta) &\equiv \Pi_{ij}^{[1]} - \frac{1}{3} \delta_{ij} \text{Tr}(\Pi^{[1]}), \\ O_{\text{td}}^{(3)} &\equiv \frac{21}{10} K^{ij} \left( \Pi_{ij}^{[2]} - \Pi_{ik}^{[1]} \Pi_{jk}^{[1]} \right), \end{aligned} \quad (4.27)$$

where we have used the shorthand notation  $K^n = \text{tr}(K^n)$ . After careful calculations, one can find the following expression for the tracer density field up to the third order

$$\begin{aligned} \delta_g(\mathbf{x}, \eta) &= b_1(\eta) \delta(\mathbf{x}, \eta) \\ &+ \frac{1}{2} b_2(\eta) \delta^2(\mathbf{x}, \eta) + \frac{1}{2} b_{K^2}(\eta) K^2(\mathbf{x}, \eta) \\ &+ \frac{1}{6} b_3(\eta) \delta^3(\mathbf{x}, \eta) + \frac{1}{6} b_{K^3}(\eta) K^3(\mathbf{x}, \eta) + \frac{1}{6} b_{\delta K^2} \delta K^2 + \frac{1}{6} b_{\Gamma_3}(\eta) \Gamma_3(\mathbf{x}, \eta). \end{aligned} \quad (4.28)$$

## 4.4 Higher-derivative bias

So far we have assumed the formation of tracers to be perfectly local in space. However, we are well aware that this is just an approximation since the matter that forms the tracer will come from a finite area of space. To account for this non-locality, we need to replace the operators  $\{O(\mathbf{x}, \eta)\}$  with functionals [36, 78]. If we take  $O = \delta$ , expression in the terms of functional will be

$$b_\delta(\eta) \delta(\mathbf{x}, \eta) \rightarrow \int d^3 y F_\delta(\mathbf{y}, \eta) \delta(\mathbf{x} + \mathbf{y}, \eta), \quad (4.29)$$

where  $F_\delta(\mathbf{y}, \eta)$  is a time dependent kernel. Since the Universe is homogeneous, we know that  $F_\delta(\mathbf{y}, \eta)$  can not depend on  $\mathbf{x}$ . We can further Taylor expand  $\delta(\mathbf{x} + \mathbf{y}, \eta)$  around  $\mathbf{x}$

$$\begin{aligned} b_\delta(\eta) \delta(x, \eta) &\rightarrow \left[ \int d^3 y F_\delta(y, \eta) \right] \delta(x, \eta) + \left[ \frac{1}{6} \int d^3 y |y|^2 F_\delta(y, \eta) \right] \nabla_x^2 \delta(x, \eta) + \dots \\ &= b_\delta(\eta) \delta(x, \eta) + b_{\nabla^2 \delta}(\eta) \nabla_x^2 \delta(x, \eta) + \dots \end{aligned} \quad (4.30)$$

To derive this expression, we have used the assumption of isotropy, which ensures that no preferred directions exist with which the derivative operators could be contracted. Consequently, the leading *higher-derivative* operator that accounts for the non-locality of halo formation is  $\nabla_x^2 \delta$ . The coefficients of higher-derivative operators are related to the spatial scale  $R_*$ , which quantifies the size of the region involved in the halo formation process. On large scales, their contribution to  $\delta_{h,\text{det}}$  is suppressed by powers of  $k^2 R_*^2$ . Since  $\nabla_x^2 \delta$  is a local observable, it should also be included in the general bias expansion given by Eq. (4.5).

## 4.5 Renormalized galaxy bias

In Sec. 3.2.2, we discussed how renormalization is applied to handle both the large and nonphysical (i.e.,  $\Lambda$ -dependent) contributions to the matter density field,  $\delta$ . A similar approach is required for the tracer density. The bias expansion, used to express the tracer density  $\delta_g$  in terms of local observables, includes composite operators (products of fields evaluated at the same point), such as  $\delta^2$ . These types of operators can introduce additional divergences that cannot be removed through the renormalization of dark matter alone. To better understand this issue, consider the expression for  $\delta_g^{(2)}$ , which is given by

$$\delta_g^{(2)} = b_\delta \delta^{(2)} + b_{\delta^2} (\delta^{(1)})^2. \quad (4.31)$$

Taking the expectation value, we find:

$$\begin{aligned} \langle \delta_g^{(2)} \rangle &= b_\delta \langle \delta^{(2)} \rangle + b_{\delta^2} \langle (\delta^{(1)})^2 \rangle \\ &= b_{\delta^2} \langle \delta^2 \rangle \propto \int_0^\Lambda dq q^2 P(q) \equiv \sigma^2(\Lambda), \end{aligned} \quad (4.32)$$

where we used that  $\langle \delta^{(2)} \rangle = 0$ . Here we are met with two issues; not only is  $\langle \delta_g^{(2)} \rangle$  different from zero, but it also clearly has a  $\Lambda$  dependence. These issues are not limited to  $\langle \delta_g^{(2)} \rangle$  alone; similar problems arise when moving to higher orders in perturbation theory. To resolve these issues, we employ renormalization theory.

There are several approaches one can adopt for renormalization. The most widely used method for galaxy bias renormalization involves the introduction of local counterterms, whose primary role is to eliminate nonphysical contributions [9, 98]. Composite operators constructed from  $\delta^n(\mathbf{x}, \eta)$ , as shown in [9], can be made finite through the use of renormalized operators, which are defined as:

$$[\delta^n](\mathbf{x}, \eta) \equiv \delta^n(\mathbf{x}, \eta) + \sum_{\tilde{\mathcal{O}}} Z_{\tilde{\mathcal{O}}}^{(\delta^n)} \tilde{\mathcal{O}}(\mathbf{x}, \eta) \ll 1, \quad (4.33)$$

where  $\tilde{\mathcal{O}}(\mathbf{x}, \eta)$  are counterterms introduced to cancel UV divergences, and  $Z_{\tilde{\mathcal{O}}}$  are their associated coefficients. These counterterms,  $\tilde{\mathcal{O}}(\mathbf{x}, \eta)$ , are typically constructed from any operators that respect the symmetries of the dark matter equations of motion. These counterterms are precisely the set of operators in the general bias expansion; hence we say that this bias expansion is closed under renormalization.

Returning to the example of  $\delta_h^{(2)}$ , we derive the following expression

$$[\delta^2](\mathbf{x}, \eta) \equiv \delta^2(\mathbf{x}, \eta) - \sigma^2(\Lambda), \quad (4.34)$$

where  $\sigma^2(\Lambda)$  accounts for the contribution from small-scale fluctuations. With this renormalized operator  $[\delta^2]$ , it becomes evident that in the expectation value  $\langle \delta_g^{(2)} \rangle$ , the dependence on  $\Lambda$  is eliminated, and the result is indeed zero.

In general, once renormalization has been properly carried out, i.e. when all relevant counterterms have been included, the result is a bias expansion in terms of renormalized bias operators:

$$\delta_g(\mathbf{x}, \eta) = \sum_{\mathcal{O}} b_{\mathcal{O}}^{[R]}(\eta) \mathcal{O}(\mathbf{x}, \eta), \quad (4.35)$$

where the coefficients  $b_{\mathcal{O}}^{[R]}$  are renormalized bias coefficients that no longer depend on the cutoff scale  $\Lambda$ .

An alternative approach, based on the usage of renormalization-group, has been presented first for matter in [33] and recently for biased tracers in [107]. The renormalization group technique was introduced by Wilson [146] and Polchinski [103]. In this case, one starts from the partition function for biased tracers which was introduced in [29]. By integrating out small-scale modes, one can find RG equations that govern the running of the bias coefficients. This method has recently been expanded to account for stochasticity in [108] and non-Gaussian initial conditions in [91].

In this section we only briefly outlined why normalization of bias parameters is necessary and in which ways it can be performed. Details of this procedure are much more complex and beyond the scope of this thesis. A reader interested in learning more about the topic can consult one of the references listed in the paragraph above.



# Chapter 5

## Baryon Acoustic Oscillations

Baryon acoustic oscillations (BAO) are an oscillatory feature in the matter power spectrum [49]. The same feature is visible in the correlation function as a bump located at the characteristic BAO scale  $r_s$ . The origin of the BAO can be found in the early Universe era when photons and baryons were tightly coupled by Compton scattering, forming the baryon-photon fluid. During this era, the gravitational force acting on the baryon perturbations was balanced by the radiation pressure resulting in acoustic oscillations of the baryon-photon fluid [49]. As the Universe expands and cools down, photons decouple. Traces of these sound waves remain visible as the acoustic oscillations in the CMB temperature anisotropies with the characteristic scale of the sound horizon at decoupling,  $r_s$ . Essentially the same scale is imprinted as the acoustic density perturbations in the baryon distribution. Since baryons are coupled to dark matter gravitationally, and both jointly evolve under gravitational evolution after decoupling, the imprint of these early-time oscillations is visible at fixed comoving scale in the late-time clustering of matter. Given that the size of the sound horizon at decoupling has been well measured through CMB experiments, determining its apparent size in the late-time matter distribution allows us to estimate the angular-diameter distance and the Hubble parameter as a function of redshift.

In the first section of this chapter, we will focus on understanding the physics of BAO. We will begin with linear theory and then introduce the effects of non-linear evolution. In the second section, we will present and discuss the BAO reconstruction algorithm. Finally, in the last section, we will demonstrate how the BAO scale can be used as a standard ruler. This chapter is based on a large number of references, the main ones are Chapter 9 and Chapter 11 in [45] together with [16, 48, 95].

### 5.1 Physics of Baryon Acoustic Oscillations

The goal of this section is to derive the equation that describes the evolution of the baryon-photon fluid, particularly during the period before and around decoupling. Before we proceed to the main analysis, it is important to cover some relevant background information.

### 5.1.1 Boltzmann equation for Photons

Photons are relativistic particles, and as such, the Boltzmann equation they obey differs from the one applied to non-relativistic matter, as shown in Eq. 3.2. Furthermore, in the early Universe, the Boltzmann equation for photons cannot ignore collisions, as photons interact with baryons through Compton scattering:

$$e^-(\mathbf{p}_1) + \gamma(\mathbf{q}_1) \leftrightarrow e^-(\mathbf{p}_2) + \gamma(\mathbf{q}_2). \quad (5.1)$$

Consequently, the photon distribution function,  $f_\gamma$ , satisfies the following form of the Boltzmann equation:

$$\frac{df_\gamma}{dt} = C[f_\gamma], \quad (5.2)$$

where  $C[f_\gamma]$  is a collision term. By expanding the total derivative and using geodesic equation, one can show that the left hand side of this equation equals to

$$\frac{df_\gamma}{dt} = \frac{\partial f_\gamma}{\partial t} + \frac{\hat{p}^i}{a} \frac{\partial f_\gamma}{\partial x^i} - p \frac{\partial f_\gamma}{\partial p} \left[ H + \dot{\Phi} + \frac{\hat{p}^i}{a} \frac{\partial \Psi}{\partial x^i} \right]. \quad (5.3)$$

In a homogeneous Universe, the photon distribution function follows a Bose-Einstein distribution, with the photon temperature  $T$  depending solely on time. However, the actual Universe deviates from perfect homogeneity. To account for these deviations, we introduce perturbations to the distribution function, described by a fractional temperature perturbation  $\Theta(\mathbf{x}, \hat{\mathbf{p}}, t)$ , which modifies the photon distribution as follows:

$$f_\gamma(\mathbf{x}, p, \hat{\mathbf{p}}, t) = \left[ \exp \left\{ \frac{p}{T(t)[1 + \Theta(\mathbf{x}, \hat{\mathbf{p}}, t)]} \right\} - 1 \right]^{-1}. \quad (5.4)$$

Fractional temperature  $\Theta(\mathbf{x}, \hat{\mathbf{p}}, t)$  reflects the fact that the temperature also depends on the photon's position  $\mathbf{x}$  and its direction of motion  $\hat{\mathbf{p}}$ . Using the fact that the perturbation  $\Theta$  is small, we can expand  $f_\gamma$  to first order in  $\Theta$ :

$$f_\gamma(\mathbf{x}, p, \hat{\mathbf{p}}, t) \approx f_\gamma^{(0)}(p, t) - p \frac{\partial f_\gamma^{(0)}(p, t)}{\partial p} \Theta(\mathbf{x}, \hat{\mathbf{p}}, t), \quad (5.5)$$

where  $f^{(0)}$  is a Bose-Einstein distribution with zero chemical potential. Inserting this expansion back into Boltzmann equation 5.3 leads to:

- 0th order

$$\frac{df_\gamma}{dt} = \frac{\partial f^{(0)}}{\partial t} - Hp \frac{\partial f^{(0)}}{\partial p} = 0 \quad (5.6)$$

- 1st order

$$\frac{df_\gamma}{dt} = -p \frac{\partial f^{(0)}}{\partial p} \left[ \Theta' + \frac{\hat{p}^i}{a} \frac{\partial \Theta}{\partial x^i} + \Phi' + \frac{\hat{p}^i}{a} \frac{\partial \Psi}{\partial x^i} \right], \quad (5.7)$$

where we have used prime to represent the derivative with respect to  $t$ . Total derivative at the 0th order is set to zero. Therefore, all the collision terms will be proportional to  $\Theta$  and all other perturbations to homogeneous Universe.

Before we give the Boltzmann equation for photons which accounts for the Compton scattering, let us stress it is often more convenient to work in terms of the multipole moments of  $\Theta$  rather than  $\Theta$  itself. These moments are defined as

$$\Theta_l(k, t) \equiv \frac{1}{(-i)^l} \int_{-1}^1 \frac{d\mu}{2} \mathcal{P}_l(\mu) \Theta(\mu, k, t), \quad (5.8)$$

where  $\mu$  is the cosine of the angle closed by the wavenumber  $\mathbf{k}$  and the photon direction  $\hat{\mathbf{p}}$ :

$$\mu \equiv \frac{\mathbf{k} \cdot \hat{\mathbf{p}}}{p}. \quad (5.9)$$

With  $\mathcal{P}_l$  we denote the Legendre polynomial of order  $l$ . We will mostly be interested in the monopole ( $l = 0$ ) and the dipole ( $l = 1$ ), as higher-order multipoles capture information about the small-scale anisotropies of radiation. Describing photon perturbations in terms of the hierarchy of moments  $\Theta_l$  is completely equivalent to using  $\Theta$ .

Now we are ready to discuss the Boltzmann equation for photons with Compton scattering, which is given by:

$$\Theta' + \hat{p}^i \frac{\partial \Theta}{\partial x^i} + \Phi' + \hat{p}^i \frac{\partial \Psi}{\partial x^i} = n_e \sigma_T [\Theta_0 - \Theta + \hat{\mathbf{p}} \cdot \mathbf{u}_b], \quad (5.10)$$

where  $n_e$  is number density of free electrons,  $\sigma_T$  is Compton scattering cross section and  $\mathbf{u}_b$  is baryon velocity. Notice that we have switched from derivatives with respect to  $t$  to derivatives with respect to  $\eta$ , which we denote with a dot. The first two terms in this equation on their own would exist in the collisionless case and they describe the derivatives along light rays in homogeneous Universe. The second two terms on the left side describe the effects gravitational perturbations have on the photon. Finally, the right hand side describes interaction with baryons. It will be more convenient to have this equation in Fourier space:

$$\dot{\Theta} + ik\mu\Theta + \dot{\Phi} + ik\mu\Psi = -\dot{\tau} [\Theta_0 - \Theta + \mu\mathbf{u}_b] \quad (5.11)$$

Here we have introduced the optical depth

$$\tau(\eta) \equiv \int_{\eta}^{\eta_0} d\eta' n_e \sigma_T a. \quad (5.12)$$

Optical depth measures the transparency of the Universe to photons, indicating the likelihood that a photon will be scattered by an electron. In the early Universe, the number of free electrons is high, so the chances of a photon being scattered are also high, corresponding to  $\tau \gg 1$ . We refer to this as strong coupling condition. Conversely, at later times, the number of free electrons is small so  $\tau \ll 1$ . Note that  $\tau$  is defined such that

$$\dot{\tau} = \frac{d\tau}{d\eta} = -n_e \sigma_T a. \quad (5.13)$$

### 5.1.2 Boltzmann Equation For Baryons

The word baryons has wider meaning in cosmology than it does in particle physics. In particle physics, baryons are subatomic particles made from three quarks, such as protons and neutrons. However, in cosmology, baryons refer to all forms of ordinary matter made up of protons and neutrons. This includes atomic nuclei (protons and neutrons bound together) as well as their associated electrons, even though electrons are not technically baryons in the particle physics sense. Results listed here can be applied to all the baryons. Electrons and protons are coupled together through Coulomb scattering.

$$e^-(\mathbf{p}_1) + p(\mathbf{q}_1) \leftrightarrow e^-(\mathbf{p}_2) + p(\mathbf{q}_2). \quad (5.14)$$

This scattering ensures that:

$$\frac{\rho_{e^-} - \bar{\rho}_{e^-}}{\rho_{e^-}} = \frac{\rho_p - \bar{\rho}_p}{\rho_p} \equiv \delta_b. \quad (5.15)$$

Similarly, their velocities are also the same

$$\mathbf{u}_{e^-} = \mathbf{u}_p \equiv \mathbf{u}_b. \quad (5.16)$$

Since baryons are non-relativistic, similar to dark matter, the total derivative of their distribution function follows the same form as in Eq. (3.2):

$$\frac{\partial f_b}{\partial t} + \frac{\partial f_b}{\partial x^i} \frac{p^i}{m_b a} - \frac{\partial f_b}{\partial p^i} \left( H p^i + \frac{m_b}{a} \frac{\partial \Psi}{\partial x^i} \right) = 0, \quad (5.17)$$

where  $f_b$  represents the baryon distribution function and  $m_b$  is the baryon mass.

However, due to interactions such as Compton scattering with photons and Coulomb scattering among baryons, the total derivative is no longer zero. These scattering processes conserve the number of baryons, and any other processes that could alter the baryon number are negligible during this epoch. By taking the zeroth moment of the Boltzmann equation, we obtain the continuity equation for baryons:

$$\dot{\delta}_b + i k u_b + 3\dot{\Phi} = 0, \quad (5.18)$$

To find the Euler equation for baryons, we need to take the first moment of Eq. (5.17) for each baryon and add them together. Since the proton mass is much larger than the electron ones, it will dominate this equation and we will arrive to

$$m_p \frac{\partial (n_b u_b^j)}{\partial t} + 4H m_p n_b u_b^j + \frac{m_p n_b}{a} \frac{\partial \Psi}{\partial x_j} = C^j(x, t), \quad (5.19)$$

where  $C$  is the collision term. While the number of baryons is conserved during Compton scattering, momentum is transferred between the particles and  $C$  is the force term that accounts for this. Since the overall momentum is conserved,  $C$  needs to have the same

magnitude and the opposite sign from the force term in Boltzmann equation for photons. By taking the first moment of the Boltzmann equation for photons (5.3) and applying some algebra, we arrive to the Euler equation for baryons:

$$\dot{u}_b + \mathcal{H}u_b + ik\Psi = \frac{\dot{\tau}}{R} [3i\Theta_1 + u_b], \quad (5.20)$$

where we have introduced  $R$  to be the ratio of photon and baryon density:

$$\frac{1}{R(\eta)} \equiv \frac{4\rho_\gamma}{3\rho_b}. \quad (5.21)$$

### 5.1.3 Linear Theory of BAO

#### Acoustic Oscillations Equation

Before decoupling photons and baryons are tightly coupled together into baryon-photon fluid. To derive the equation describing this fluid, we will start with the Boltzmann equation for photons (5.3). By multiplying this equation with  $\mathcal{P}_0(\eta)/2$  and integrating over  $\mu$ , we find the zeroth moment of this equation to be

$$\dot{\Theta}_0 + k\Theta_1 = -\dot{\Phi}. \quad (5.22)$$

Similarly, by multiplying the Eq. (5.3) with  $\mathcal{P}_1(\eta)/2$  and integrating over  $\mu$ , we arrive to the first moment of the equation

$$\dot{\Theta}_1 - \frac{k\Theta_0}{3} = \frac{k\Psi}{3} + \dot{\tau} \left[ \Theta_1 - \frac{iu_b}{3} \right], \quad (5.23)$$

where  $u_b$  is baryon velocity described with Eq. (5.20). To eliminate the velocity from the equation, we can rewrite it as

$$u_b = -3i\Theta_1 + \frac{R}{\dot{\tau}} [\dot{u}_b + \mathcal{H}u_b + ik\Psi]. \quad (5.24)$$

The second term in this equation is going to be suppressed. Reason for this is that we have terms proportional to  $1/\tau$  and  $k/\tau$  with  $\tau \gg 1$ . Therefore, at the leading order  $u_b = -3i\Theta_1$ . To find  $u_b$  at the next order, we simply insert the leading order solution back into Eq. (5.24):

$$u_b = -3i\Theta_1 + \frac{R}{\dot{\tau}} \left[ -3i\dot{\Theta}_1 - 3i\mathcal{H}\Theta_1 + ik\Psi \right]. \quad (5.25)$$

Inserting Eq. (5.25) into Eq. (5.23) lead us to

$$\dot{\Theta}_1 + \mathcal{H}\Theta_1 - \frac{1}{3} \frac{k}{1+R} \Theta_0 = \frac{k\Psi}{3} \quad (5.26)$$

To eliminate  $\Theta_1$ , we substitute its expression from Eq. (5.22), which relates  $\Theta_1$  to  $\dot{\Theta}_0$  and  $\dot{\Phi}_0$ . Similarly, to eliminate  $\dot{\Phi}_1$ , we differentiate Eq. (5.22) with respect to  $\eta$ . This finally leads to the equation describing the photon evolution during the strong coupling era:

$$\ddot{\Theta}_0 + \mathcal{H} \frac{R}{1+R} \dot{\Theta}_0 + k^2 c_s^2 \Theta_0 = F(k, \eta), \quad (5.27)$$

where we have defined

$$F(k, \eta) \equiv -\frac{k^2}{3} \Psi - \mathcal{H} \frac{R}{1+R} \dot{\Phi} - \ddot{\Phi}. \quad (5.28)$$

We have also defined the sound speed of the combined baryonphoton fluid as

$$c_s(\eta) \equiv \sqrt{\frac{1}{3[1+R(\eta)]}}. \quad (5.29)$$

Equation (5.26) corresponds to a differential equation that describes the behavior of a forced harmonic oscillator. In this analogy,  $F(k, \eta)$  serves as the external driving force that influences the evolution of temperature perturbations  $\Theta_0$ . This term encapsulates the combined effects of gravitational potential fluctuations and other perturbative forces acting on the photon-baryon fluid. Gravity drives oscillations, similar to a force applied to a mass-spring system. Additionally, the frequency and speed of these oscillations are governed by the sound speed  $c_s$ , which depends on the relative densities of photons and baryons. As the number of baryons increases relative to photons, the increased mass of the baryons adds inertia to the system, providing greater resistance to motion. This increased resistance slows the oscillations. Thus, the presence of more baryons effectively damps the oscillatory behavior, reducing both the frequency and speed of the oscillations. Finally, the term  $\mathcal{H} \frac{R}{1+R} \dot{\Theta}_0$  corresponds to a drag term, and it is a consequence of the expansion of the Universe.

For comparison, we could also express the same dynamics in terms of baryon density, as shown in [46, 77, 99]:

$$\frac{d}{d\eta} [(1+R)\delta] + \frac{k^2}{3} \delta = -k^2(1+R)\Phi - \frac{d}{d\eta} [3(1+R)\Psi]. \quad (5.30)$$

This equation also describes a forced harmonic oscillator, demonstrating consistency between perturbations in baryons and photons. The growth of the amplitude of baryon perturbations is constrained by their interactions with photons. Instead of exhibiting unbounded growth, these perturbations undergo harmonic motion, with the amplitude decaying as  $(1+R)^{-1/4}$  [56, 57]. This decay depends on the photon density. As the baryon density increases, the damping effect becomes more and more pronounced.

This oscillatory motion will continue until photons and baryons decouple. This happens when  $\tau(\eta)$  reaches a value close to one. After this, photons and baryons go their separate ways and oscillations in baryons remain frozen-in. Expanding the Eq. (5.30) to higher order in  $k/\dot{\tau}$ , reveals that photon-baryon diffusion causes an exponential damping of these

perturbations, a phenomenon known as Silk damping [126]. This suppression becomes significant at small scales, with the characteristic damping scale approximately given by the geometric mean of the horizon size and the photon mean free path at the time of decoupling. The same result can be obtained by considering photon perturbations. For a comprehensive derivation of this result from the perspective of photon perturbations, see Sec. 9.4 in [45].

### Physical picture of fluid evolution

To gain a clearer understanding of this phenomenon, let us examine the evolution of an initial point-like overdensity within the fluid. Gravity tries to intensify this overdensity, causing photons to be drawn closer together. As the density increases, the temperature and pressure of the photons rise correspondingly. This rising pressure initiates the propagation of a spherical sound wave through the baryon-photon plasma, aiming to reach equilibrium. The sound wave travels at the speed of sound  $c_s$ , and the dynamic interplay between gravitational compression and pressure-driven expansion continues until decoupling. At decoupling, the photons and baryons are no longer tightly coupled, and the oscillations stop. Photons then begin to free-stream, eventually forming what we observe today as CMB. Baryons are left with a higher density organized into a spherical shell at a specific radius from the initial overdensity. After decoupling, baryons primarily interact gravitationally with dark matter. This interaction draws dark matter particles toward the same radius as the overdense shell of baryons. As a result, the probability of galaxy formation increases in these regions, giving rise to the large-scale structure of the Universe that we observe today. This characteristic radius, where the probability of galaxy formation is enhanced, is commonly referred to as the *Baryon Acoustic Oscillation (BAO) scale*. It corresponds to the distance the sound wave traveled by the time of decoupling:

$$r_s = \int_{z_{rec}}^{\infty} \frac{c_s dz}{H(z)} = \frac{1}{\sqrt{\Omega_m H_0^2}} \frac{2c}{\sqrt{3z_{eq} R_{eq}}} \ln \left[ \frac{\sqrt{1 + R_{rec}} + \sqrt{R_{rec} + R_{eq}}}{1 + \sqrt{R_{eq}}} \right], \quad (5.31)$$

where  $R_{rec}$  is the baryon photon ratio at the time of decoupling and  $R_{eq}$  is their ratio at the time of matter and radiation equality. The value of BAO scale is around  $150\text{Mpc}^1$ . The BAO scale manifests as a characteristic feature in the matter correlation function. If a galaxy had formed at the center of the initial perturbation, a distinct bump would appear in the correlation function at the distance  $r_s$ . The same feature is visible in the power spectrum as a series of wiggles.

This process is well-illustrated in the famous Figure 5.1, originally published in [51], which also provides a more rigorous analysis of overdensity evolution.

---

<sup>1</sup>Note the different unit convention used here compared to the rest of the thesis: we use Mpc instead of  $h^{-1}\text{Mpc}$

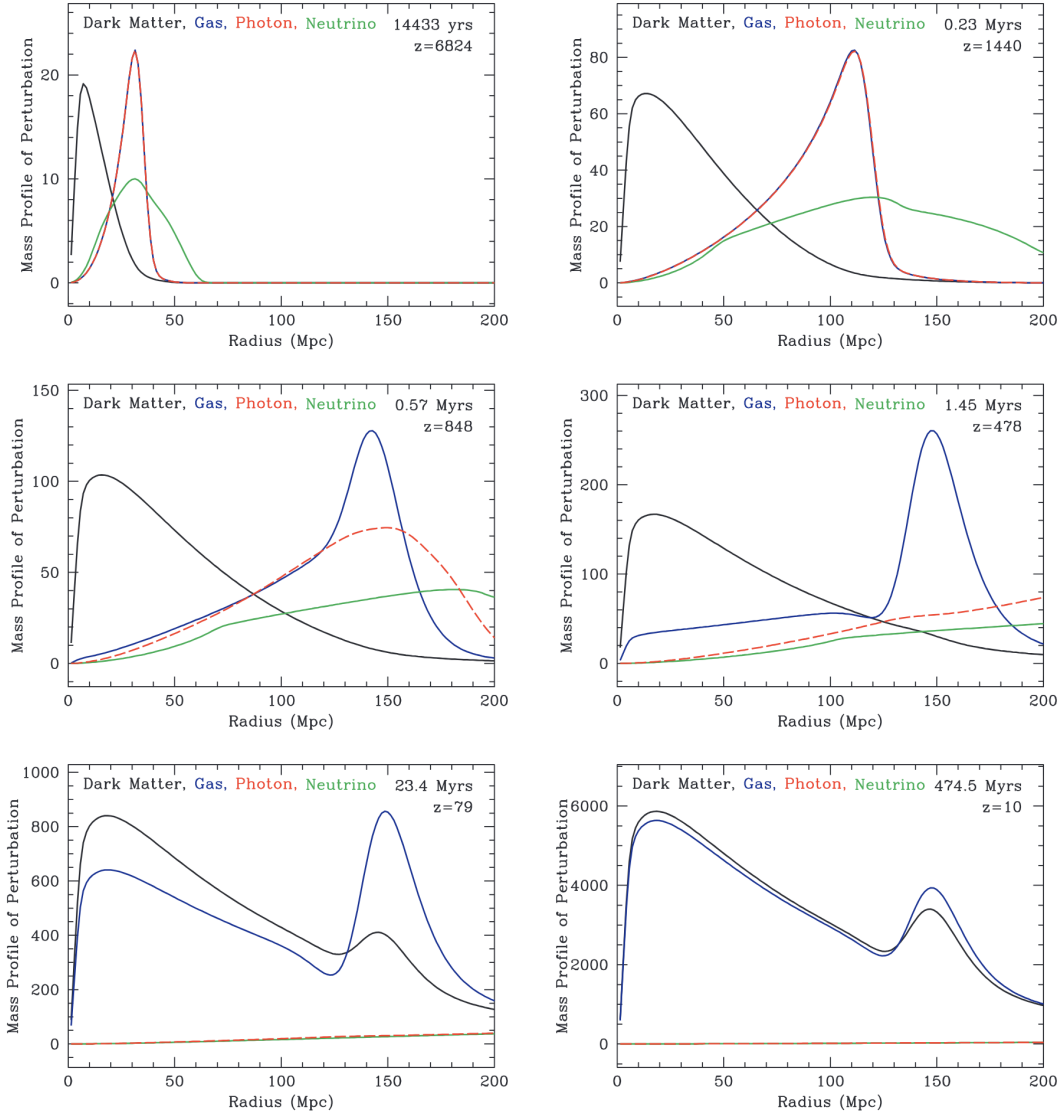


Figure 5.1: Evolution of the radial mass profile of a point-like overdensity initially positioned at  $r = 0$ . Dark matter perturbations are shown in black, baryon perturbations in blue, photon perturbations in red, and neutrino perturbations in green. Time progresses from higher redshift at the top to lower redshift at the bottom, and redshift also decreases from left to right. In the top-left panel, we observe that photon and baryon perturbations evolve together. In the top-right panel, we see that this evolution causes the cold dark matter to respond due to its gravitational interaction with the photon-baryon fluid. As recombination approaches, photons begin to decouple and leak away (middle-left panel), eventually leaving the baryon perturbations behind at the characteristic scale  $r_s$ . In the bottom panels, gravity takes over, pulling both baryons and dark matter into the overdense regions  $r = 0$  and  $r = r_s$ . This image was first published by Eisenstein et al. in [51].

### 5.1.4 Non-linear Evolution and Galaxy Clustering Bias

As we have seen in Sec. 3 and Sec. 4 structure formation is a highly non-linear process. This nonlinear evolution moves galaxies away from their original positions which shifts and broadens the peak in the correlation function [6, 7, 58, 65, 81, 123, 128, 140]. This will result in reduced precision with which we can measure the BAO scale from galaxy clustering data [23, 119] and introduce a bias in the measurement.

To understand better how non-linear evolution affects the BAO, we go back to considering initial point-like perturbation whose evolution we have discussed in the Sec. 5.1. There, we have explained the peak in the correlation function as arising from baryon overdensity that was left once the acoustic wave staled at the decoupling. If we were then to consider the later evolution of such a spherical shell, we would expect it to go through some gravitational collapse caused by its interaction with the galaxy formed in the center and due to its own self-gravity. This kind of collapse would slightly shrink the size of the BAO.

In addition to slightly shifting the position of the peak in the correlation function, non-linearities also lead to the broadening of this peak. This effect can be intuitively understood using the same simplified model. Suppose a galaxy forms at a specific location on a shell of radius  $r_s$ . The position of this galaxy will be influenced by interactions with other overdensities in the vicinity. These interactions can displace the galaxy in various directions, either closer to or further from the center. Since the correlation function averages over the positions of all galaxies, the cumulative effect of these displacements is to broaden the peak in the correlation function. To estimate the RMS displacement, we begin by smoothing the observed density field using a smoothing scale  $R$ . Next, we calculate the displacement by applying the Zel'dovich approximation to the smoothed density field. In particular, [51] demonstrates that these displacements typically shift particles by approximately  $10 h^{-1}\text{Mpc}$ .

Non-linearities also affect the power spectrum. The broadening of the peak in the configuration space will correspond to damping of the wiggles at higher  $k$  values in the Fourier space. Naturally, this affects the measurement precision of BAO from the galaxy power spectrum.

In this section, we have presented a simplified view of how non-linearities affect the BAO scale. For a more comprehensive discussion on this topic, we refer to [51]. This reference demonstrates that the primary source of the broadening in the BAO feature arises from large-scale modes. Large-scale modes are not as affected by non-linear evolution and can nicely be modeled using perturbation theory. This insight has led to the development of methods which can be used to reverse these broadening effects in the correlation function and the damping in the power spectrum. These methods are called *BAO reconstruction* methods, and they will be the topic of the next section.

## 5.2 BAO reconstruction

### 5.2.1 Reconstruction Algorithm

In the previous section, we discussed how non-linear evolution impacts the precision of BAO measurements from galaxy clustering. Specifically, non-linear effects widen the peak in the correlation function and erase the higher harmonics in the power spectrum. The goal of the reconstruction is to exploit the fact that these effects come from large scale gravitational effects. By correcting these effects, the reconstruction enhances the accuracy of our BAO measurements and mitigates systematic shift in BAO scale size.

BAO reconstruction procedure was first introduced in [50]. This technique was based on the fact that Zel'dovich approximation captures important aspects of non-linear evolution at large scales. By applying the the reversed Zel'dovich approximation to an observed galaxy field, it can estimate the displacement caused by non-linearities. The algorithm for this technique is as follows:

1. Smooth the observed tracer density field,  $\delta_g$ , by applying a filter  $S(k, R)$  with a smoothing scale  $R$ :

$$\delta_g(\mathbf{k}) \rightarrow S(k, R)\delta_g(\mathbf{k}).$$

This step removes high- $k$  non-linearities.

2. Compute the negative Zel'dovich displacement from the smoothed density field:

$$\mathbf{s}(\mathbf{k}) \equiv -i \frac{\mathbf{k}}{k^2} S(k) \frac{\delta_g(\mathbf{k})}{b_1},$$

where the tracer density field has been divided by the linear bias  $b_1$  to obtain the matter density field.

3. Shift the original particles by  $\mathbf{s}$  and compute the *displaced* density field,  $\delta_d$ .
4. Shift a spatially uniform grid of particles by  $\mathbf{s}$  to get the *shifted* density field,  $\delta_s$ .
5. Find the *reconstructed* density field as the difference between the displaced and shifted density fields,  $\delta_r$ :

$$\delta_r = \delta_d - \delta_s.$$

The effects of the reconstruction are nicely illustrated in the Fig. 5.2 which was first published by Padmanabhan et al. in [95].

The first application of BAO reconstruction to any observed data was on galaxy catalogues from the Sloan Digital Sky Survey (SDSS) [147] in [96]. Ever since then, almost every large scale survey in the past decade, such as Baryon Oscillation Spectroscopic Survey [41], the extended Baryon Oscillation Spectroscopic Survey [40], WiggleZ [22] and DESI [76], has used the BAO reconstruction as a part of their BAO analysis. The gain

in the statistical precision depended on the survey, but it was up to 45% reduction in the error bar size in certain samples [3, 5, 37, 68, 85, 97, 136].

When it comes to applying BAO reconstruction to survey data, one has to additionally account for the redshift-space distortions (RSD) which arise due to the peculiar motion of galaxies [67]. Peculiar motion affects the measurements of cosmological redshifts by introducing additional Doppler shift, which results in change of the broad band of the power spectrum or the correlation function. Depending on the way RSD is treated during the reconstruction, we differentiate between the isotropic BAO reconstruction [5, 96] and anisotropic BAO reconstruction [50, 121, 122]. The anisotropic reconstruction tries to keep the RSD signal in the reconstructed density field, while the isotropic reconstruction attempts to remove it. In later chapters, we will be looking into BAO analysis in the rest frame of galaxies only. Therefore, RSD will not have any effect in our case so we will not be giving any more details on it.

### 5.2.2 Understanding BAO Reconstruction Using Lagrangian Perturbation Theory

While this reconstruction method is straightforward to implement, its intuitive understanding is challenging due to the non-linear mapping of the observed density field. However, the Lagrangian perspective on reconstruction, initially introduced for the matter density field in [95] and subsequently extended to biased tracers in [93], can provide valuable insights into the function of each step in the reconstruction process.

We will assume that the particles have been observed at some position  $\mathbf{x}$ , which is displaced from their initial position  $\mathbf{q}$  by the vector field  $\boldsymbol{\psi}$ :

$$\mathbf{x} = \mathbf{q} + \boldsymbol{\psi}(\mathbf{q}). \quad (5.32)$$

Then the observed density is given by:

$$\delta(\mathbf{k}) = \int_{\mathbf{q}} e^{-i\mathbf{k}\cdot\mathbf{q}} \left( e^{-i\mathbf{k}\cdot\boldsymbol{\psi}(\mathbf{q})} - 1 \right). \quad (5.33)$$

Note that we have dropped the time argument for clarity.

The first step in the reconstruction is to smooth the density field with the filter  $S(k, R)$ . Then we use that smoothed density field to estimate the negative Zel'dovich displacement:

$$\mathbf{s}(\mathbf{k}) \equiv -i \frac{\mathbf{k}}{k^2} S(k) \frac{\delta_g(\mathbf{k})}{b_1}. \quad (5.34)$$

Since the displacement field  $\mathbf{s}$  is derived using the smoothed density field and the Zel'dovich approximation only captures linear information,  $\mathbf{s}$  does not fully recover all the information contained in  $\boldsymbol{\psi}$ .

Now we use the vector  $\mathbf{s}$  to move the particles closer to their initial position:

$$\mathbf{x} \rightarrow \mathbf{x} = \mathbf{q} + \boldsymbol{\psi} + \mathbf{s}. \quad (5.35)$$

This gives us the displaced density field, which can be written as

$$\delta_d(\mathbf{k}) = \int_{\mathbf{q}} e^{-i\mathbf{k}\cdot\mathbf{q}} \left( e^{-i\mathbf{k}\cdot[\boldsymbol{\psi}(\mathbf{q})+\mathbf{s}(\mathbf{q})]} - 1 \right). \quad (5.36)$$

If we use the expansion for  $\boldsymbol{\psi}$  introduced in Eq. (3.43), we can easily find the physical interpretation of  $\delta_d$ :

$$\begin{aligned} \delta_d(\mathbf{k}) &= \int_{\mathbf{q}} e^{-i\mathbf{k}\cdot\mathbf{q}} \left( e^{-i\mathbf{k}\cdot[\boldsymbol{\psi}^{(1)}(\mathbf{q})+\boldsymbol{\psi}^{(2)}(\mathbf{q})+\boldsymbol{\psi}^{(3)}(\mathbf{q})+\dots+\mathbf{s}(\mathbf{q})]} - 1 \right) \\ &= \int_{\mathbf{q}} e^{-i\mathbf{k}\cdot\mathbf{q}} \left( e^{-i\mathbf{k}\cdot(+\boldsymbol{\psi}^{(2)}(\mathbf{q})+\boldsymbol{\psi}^{(3)}(\mathbf{q})+\dots)} - 1 \right), \end{aligned} \quad (5.37)$$

where we have also used that  $\mathbf{s} \approx -\boldsymbol{\psi}^{(1)}$ . Note that a more precise approach to this calculation involves decomposing the displacement vector  $\boldsymbol{\psi}$  into long- and short-wavelength contributions, where short-wavelength contributions are removed by the smoothing on the scale  $R$ . Then this step in reconstruction removes the long-wavelength contribution to  $\boldsymbol{\psi}^{(1)}$ . However, even if we were able to reverse smaller-scale displacements, they would remain irrelevant if they occur on scales smaller than the intrinsic width of the BAO feature in the linear correlation function, as it is impossible to make the BAO feature narrower than this limit. Note that if we had used  $S(k, R) = 1$  and assumed the observed density field was perfectly linear, the displacement would move the particles back to their exact initial positions, resulting in  $\delta_d = 0$ .

Next, we generate a uniform grid of particles and displace them by  $\mathbf{s}$ . This brings us to the shifted field:

$$\delta_s(\mathbf{k}) = \int_{\mathbf{q}} e^{-i\mathbf{k}\cdot\mathbf{q}} \left( e^{-i\mathbf{k}\cdot\mathbf{s}(\mathbf{q})} - 1 \right). \quad (5.38)$$

Assuming again that  $\delta$  is linear and  $S = 1$ , we would find that  $\delta_s = -\delta$ . This result arises because  $\delta_s$  is obtained using the negative Zel'dovich displacement, which effectively reverses the original displacement. Consequently, the shifted density field  $\delta_s$  becomes the negative of the observed density field  $\delta$ .

Finally, the reconstructed density field is obtained by taking the difference between the displaced and shifted density fields:  $\delta_r = \delta_d - \delta_s$ . From the structure of  $\delta_s$  and  $\delta_d$ , it is evident that the reconstructed density field  $\delta_r$  will not be purely linear. It will also contain non-linear corrections, as can be seen from Eq. (5.37).

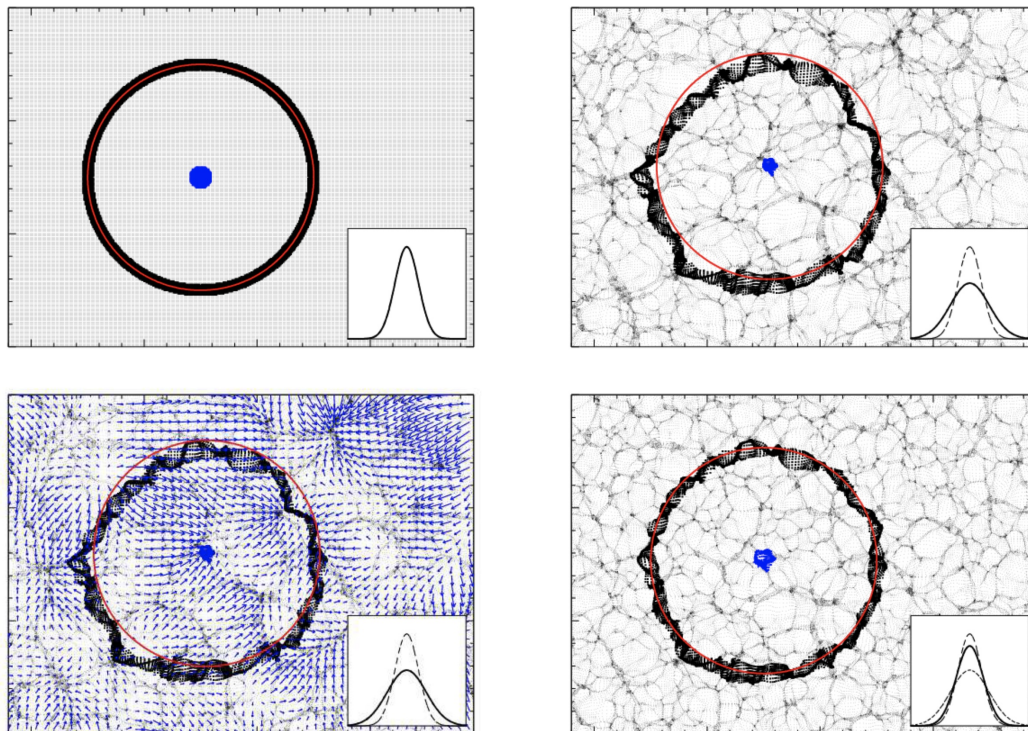


Figure 5.2: In this image, each panel shows a thin slice of the cosmological density field. The blue dot represents the point at the origin, while the thick black ring marks the particles around the BAO radius, which is depicted in red. The upper-left panel corresponds to a period close to decoupling, when the density field was still very uniform. At this stage, the black ring of points, which is a 2D representation of the Green's function shown in Fig. 5.1, is perfectly centered around the BAO radius. This panel also shows a Gaussian curve, representing the root mean square (rms) distance between the black points and the centroid marked by the blue point. In the upper-right panel, we advance to the present day. At this point, structure formation has occurred (as described by the Zel'dovich approximation), introducing non-linearities into the density field. These non-linear effects have displaced particles from their original positions, causing the once-uniform black ring to become distorted and no longer perfectly centered around the BAO radius. This displacement of particles leads to a broadening of the BAO peak in the correlation function. Additionally, in the corner of the panel, we observe that the root mean square (rms) distance between particles has increased compared to its original value. The lower-left panel displays the same image, but now includes arrows that indicate the particle displacements caused by the Zel'dovich approximation. The lower-right panel shows the results of the reconstruction process. The density field has been smoothed, and the reversed Zel'dovich displacement has been applied. As a result, the black ring now closely resembles its original form, as seen in the upper-left panel. However, it is not perfectly centered around BAO radius, as the reconstruction is not perfect. This image was first published by Padmanabhan et al. in [95].

### 5.3 Baryon Acoustic Oscillations as a Cosmological Probe

The significance of baryon acoustic oscillations (BAO) lies in their application as a standard ruler for cosmological measurements. In this section, we will derive the connection between BAO, the Hubble parameter, and the angular diameter distance. This section closely follows Sec. 11 in [45].

Galaxy redshift surveys provide the most direct measurements of the galaxy density field. These surveys map the angular positions and redshifts of galaxies, allowing us to study their 3D distribution. However, translating redshifts into distances requires assuming a fiducial cosmology, and we do not know the true cosmological model with certainty. If we assume the wrong cosmology, the BAO feature will appear at slightly different locations along the line of sight and in the transverse direction. This apparent shift allows us to measure both the Hubble parameter and the angular diameter distance by comparing the BAO positions in these two directions.

We start by expressing the observed galaxy redshift  $z$  and observed position  $(\theta, \phi)$  in terms of the 3D position vector

$$\mathbf{x}_{\text{obs}}(z, \theta, \phi) = \chi(z) \hat{\mathbf{n}}(\theta, \phi), \quad (5.39)$$

where  $\hat{\mathbf{n}}$  is a unit vector indicating galaxy position. To get the distance  $\chi(z)$ , we have to assume a cosmological model for the universe. For practical purposes, we choose a fiducial cosmology, which serves as the basis for all calculations. However, because the true cosmology of the universe is unknown, the fiducial model will inevitably differ from the true cosmology. This discrepancy can be expressed as:

$$\chi_{\text{fid}}(z) = \chi_{\text{true}}(z) + \delta\chi_{\text{true}}(z). \quad (5.40)$$

The observed and the true position of a galaxy are related as

$$\mathbf{x}_{\text{obs}} = \frac{\chi_{\text{fid}}(z)}{\chi_{\text{true}}(z)} \mathbf{x}_{\text{true}}. \quad (5.41)$$

For simplicity, we assume that we are working in the rest frame of the galaxies, where the peculiar velocity of galaxies,  $\mathbf{u}_g$ , is set to zero. This allows us to ignore the effects of redshift-space distortions (RSD) and focus solely on the issues arising from assuming the wrong cosmology. To learn more about the RSD effects on the observed power spectrum, refer to Chapter 11 in [45].

To make the rest of this section easier to follow, we break it down in a couple of steps.

#### Step 1: Connecting the coordinates

We start by making use of several approximations. First, by considering galaxies within a narrow redshift range centered on the value  $\bar{z}$ , we can simplify  $x$  to  $\hat{\chi} = \chi(\hat{z})$ , representing

the distance corresponding to the mean redshift  $\bar{z}$  of this slice. We can simplify things further by using the flat sky approximation. This approximation allows us to express the galaxy position as a 2D vector  $\boldsymbol{\theta} = (\theta^1, \theta^2)$ . We chose the origin such that  $\mathbf{x}_{\text{obs}} = 0$  corresponds to  $\boldsymbol{\theta} = 0$ ,  $z = \bar{z}$ . Note that  $\boldsymbol{\theta} = 0$  represents a point in the sky close to the center of the survey footprint.

Let us start with the observed transverse components  $(x_{\text{obs}}^1, x_{\text{obs}}^2)$ , which can be expressed as

$$(x_{\text{obs}}^1, x_{\text{obs}}^2) = \chi_{\text{fid}}(z) \times (\theta^1, \theta^2). \quad (5.42)$$

In a similar manner, we can express the true transverse components  $(x^1, x^2)$  as

$$(x_{\text{true}}^1, x_{\text{true}}^2) = \chi_{\text{true}}(z) \times (\theta^1, \theta^2). \quad (5.43)$$

To establish the relationship at linear order between the two sets of coordinates, we express  $(\theta^1, \theta^2)$  in terms of  $(x_{\text{obs}}^1, x_{\text{obs}}^2)$  and use Eq. (5.40) to find the expression

$$(x_{\text{true}}^1, x_{\text{true}}^2) = \frac{\chi_{\text{true}}(z)}{\chi_{\text{fid}}(z)} (x_{\text{obs}}^1, x_{\text{obs}}^2). \quad (5.44)$$

From this equation, it is evident that an incorrect choice of cosmology directly influences the transverse coordinates. Specifically, when  $\chi_{\text{fid}} > \chi_{\text{true}}$ , the comoving distance is overestimated, meaning the galaxy's true transverse position is closer to us than the observed position suggests. Conversely, if  $\chi_{\text{fid}} < \chi_{\text{true}}$ , the comoving distance is underestimated, and the galaxy's true transverse coordinates will be farther away than the observed ones.

Moving on to the line-of-sight component, which is characterized by the redshift  $z$ . In the case of observed coordinates,  $x_{\text{obs}}^3$  can be expressed as:

$$x_{\text{obs}}^3(z) = \chi_{\text{fid}}(z) - \chi_{\text{fid}}(\bar{z}) \approx \frac{1}{H_{\text{fid}}(\bar{z})} (z - \bar{z}). \quad (5.45)$$

Here, we have used the fact that we are considering a thin slice around the redshift  $z$ , which allows us to expand to linear order in  $z - \bar{z}$ . Expression in the true coordinates has a similar form:

$$x_{\text{true}}^3(z) \approx \frac{1}{H_{\text{true}}(\bar{z})} (z - \bar{z}) = \frac{H_{\text{fid}}(\bar{z})}{H_{\text{true}}(\bar{z})} x_{\text{obs}}^3. \quad (5.46)$$

The deviation of the fiducial cosmology affects the line-of-sight differently than it did the transverse coordinates. This dependence is primarily driven by how the comoving distance  $\chi(z)$  changes with redshift around  $\bar{z}$ . In essence, the line-of-sight coordinate reflects changes in the Hubble parameter  $H(z)$ .

Finally, we can write down the full relationship between the observed and the true coordinate of a galaxy:

$$\mathbf{x}_{\text{true}}(\mathbf{x}_{\text{obs}}) = [\alpha_{\perp} x_{\text{obs}}^1, \alpha_{\perp} x_{\text{obs}}^2, \alpha_{\parallel} x_{\text{obs}}^3], \quad (5.47)$$

where we have introduced parameters

$$\alpha_{\perp} = \frac{\chi}{\chi_{\text{fid}}} \Big|_{\bar{z}}, \quad \alpha_{\parallel} = -\frac{H_{\text{fid}}}{H} \Big|_{\bar{z}}. \quad (5.48)$$

Parameters  $\alpha_{\perp}$  and  $\alpha_{\parallel}$  play a very important role in observational cosmology. From the way they are defined, we see that by measuring them, we can infer the true Hubble rate  $H_{\text{true}}(\bar{z})$ , and the true distance  $\chi_{\text{true}}(\bar{z})$  at the redshift  $\bar{z}$ . In the case of the Euclidean universe, which is the one we are assuming,  $\chi_{\text{true}}$  is equivalent to the angular diameter distance  $D_A$ . Therefore, from this point on, we will be using  $D_A$ . Now the obvious question is how do we actually measure them? To answer this question we need to connect the observed and the fiducial statistic.

### Step 2: True and Observed Power Spectrum

Let us now focus on understanding how the galaxy statistics measured using observed positions relate to the true underlying statistics. We will analyze this on the example of the power spectrum. The first step towards finding this connection is to recognize that the number of galaxies in the same region of space should be consistent, regardless of whether we use observed coordinates or true coordinates:

$$n_{g,\text{obs}}(\mathbf{x}_{\text{obs}}) d^3\mathbf{x}_{\text{obs}} = n_{g,\text{true}}(\mathbf{x}_{\text{true}}) d^3\mathbf{x}_{\text{true}}, \quad (5.49)$$

where  $n_{g,\text{obs}}$  and  $n_g$  are the observed number densities in terms of observed and true coordinates. Next, we introduce the Jacobian  $\mathcal{J}$  as

$$\mathcal{J} \equiv \left| \frac{d^3x_{\text{true}}}{d^3x_{\text{obs}}} \right|. \quad (5.50)$$

Expressing Eq. (5.49) using the Jacobian, leads to

$$n_{g,\text{obs}}(\mathbf{x}_{\text{obs}}) = n_{g,\text{true}}(\mathbf{x}_{\text{true}}) \mathcal{J}. \quad (5.51)$$

It can be shown that the Jacobian evaluated at  $\bar{z}$  in this case equals to<sup>2</sup>:

$$\bar{\mathcal{J}} = \alpha_{\perp}^2 \alpha_{\parallel}. \quad (5.52)$$

We can easily relate the number density to the overdensity, which is an essential step toward obtaining the power spectrum. In true coordinates, this relationship is expressed as  $n_{g,\text{true}} = \bar{n}(1 + \delta_{g,\text{true}})$ , where  $\bar{n}$  represents the average number density. For the observed number density, we similarly have  $n_{g,\text{obs}} = \bar{n}_{g,\text{obs}}(1 + \delta_{g,\text{obs}})$ . The observed number density can be related to the true number density by the following equation:

$$\bar{n}_{g,\text{obs}}(\mathbf{x}_{\text{obs}}) = \bar{n}_{g,\text{true}}(\mathbf{x}_{\text{true}}) \mathcal{J}. \quad (5.53)$$

Combining Eq. (5.51) and Eq. (5.53), gives the relationship between the observed and the true overdensity

$$\delta_{g,\text{obs}}(\mathbf{x}_{\text{obs}}) = \delta_{g,\text{true}}(\mathbf{x}_{\text{true}}). \quad (5.54)$$

---

<sup>2</sup>For more details on this derivation, take a look at the Sec. 11 in [45]

Let us now rewrite this expression in the Fourier space

$$\begin{aligned}
\delta_{g,\text{obs}}(\mathbf{k}_{\text{obs}}) &= \int d^3x_{\text{obs}} e^{-i\mathbf{k}_{\text{obs}}\cdot\mathbf{x}_{\text{obs}}} \delta_{g,\text{true}}(\mathbf{x}_{\text{true}}[\mathbf{x}_{\text{obs}}]) \\
&= (\alpha_{\perp}^2\alpha_{\parallel})^{-1} \int d^3x_{\text{true}} e^{-i\mathbf{k}_{\text{true}}[\mathbf{k}_{\text{obs}}]\cdot\mathbf{x}} \delta_{g,\text{true}}(\mathbf{x}_{\text{true}}) \\
&= \bar{\mathcal{J}}^{-1} \delta_{g,\text{true}}(\mathbf{k}_{\text{true}}[\mathbf{k}_{\text{obs}}]), \tag{5.55}
\end{aligned}$$

where we have defined

$$\mathbf{k}_{\text{true}}[\mathbf{k}_{\text{obs}}] = \left( \alpha_{\perp}^{-1}k_1, \alpha_{\perp}^{-1}k_2, \alpha_{\parallel}^{-1}k_3 \right). \tag{5.56}$$

Finally, we have everything we need to express the observed power spectrum in the terms of the true one

$$P_{g,\text{obs}}(|\mathbf{k}_{\text{obs}}|, \bar{z}) = \bar{\mathcal{J}}^{-1} \left[ b_1 P_L(|\mathbf{k}_{\text{true}}|, \bar{z}) \Big|_{\mathbf{k}_{\text{true}}=(\alpha_{\perp}^{-1}k_1, \alpha_{\perp}^{-1}k_2, \alpha_{\parallel}^{-1}k_3)} + P_N \right], \tag{5.57}$$

where we use the linear bias  $b_1$  to relate the observed power spectrum,  $P_{g,\text{obs}}$ , to the linear matter power spectrum,  $P_L(|\mathbf{k}_{\text{true}}|, \bar{z})$ . The reason we have  $\bar{\mathcal{J}}^{-1}$  instead of  $\bar{\mathcal{J}}^{-2}$  is the additional factor of  $\bar{\mathcal{J}}$  arising from the Dirac delta function. We have also introduced the constant noise term  $P_N$ , which is not affected by the incorrect cosmology choice, for completeness.

The deviation between the fiducial cosmology used in calculations and the true underlying cosmology introduces artificial anisotropies in the observed power spectrum. This anisotropy arises because the relationship between the true wavevector,  $\mathbf{k}_{\text{true}}$ , and the observed wavevector,  $\mathbf{k}_{\text{obs}}$ , depends on the angle that  $\mathbf{k}_{\text{obs}}$  forms with the line of sight, as the parameters  $\alpha_{\parallel}$  and  $\alpha_{\perp}$  differ. This effect, known as the Alcock-Paczynski (AP) effect [4], allows for constraints on  $H(z) \times D_A(z)$ .

To illustrate this, consider two limiting orientations of  $\mathbf{k}_{\text{obs}}$ . When  $\mathbf{k}_{\text{obs}}$  is parallel to the line of sight, we have  $|\mathbf{k}| = |\mathbf{k}_{\text{obs}}|/\alpha_{\parallel}$ . On the other hand, if  $\mathbf{k}_{\text{obs}}$  is perpendicular to the line of sight, we have  $|\mathbf{k}| = |\mathbf{k}_{\text{obs}}|/\alpha_{\perp}$ . It becomes evident that the power spectrum is no longer isotropic if  $\alpha_{\perp} \neq \alpha_{\parallel}$ , since in that case  $P_L(|\mathbf{k}_{\text{obs}}|/\alpha_{\perp}) \neq P_L(|\mathbf{k}_{\text{obs}}|/\alpha_{\parallel})$ . Therefore, by comparing the power spectrum along different orientations, we can constrain  $\alpha_{\parallel}\alpha_{\perp}$ , which gives us the product of  $H(z) \times D_A(z)$ .

To break the degeneracy between  $H(z)$  and  $D_A(z)$ , we require a feature of known size in the power spectrum. By comparing the known true size of this feature to its observed size along the line of sight, we can constrain  $H(z)$ . Similarly, comparing the feature's size perpendicular to the line of sight constrains  $D_A(z)$ .

The BAO scale,  $r_s$ , serves as an ideal candidate for these measurements. It acts as a cosmological standard ruler, providing a well-defined physical scale against which the expansion history of the Universe can be measured. Its size can be precisely predicted using big-bang nucleosynthesis [38] or constrained using CMB data [99,132]. By measuring its apparent size at a given redshift  $\bar{z}$  and comparing it to its true size, we can directly determine  $H(\bar{z})$  and  $\chi(\bar{z})$ .



# Chapter 6

## EFT Based Forward Model for BAO inference

This chapter synthesizes the results of the previous chapters to finally introduce the concept of forward modeling and establish the tools necessary to perform the inference of the BAO scale using this approach. This chapter is a setup for the following two in which we present the results of this inference.

We begin by introducing the key element of the field-level approach: the joint posterior distribution for cosmological and nuisance parameters. Following this, we will look into the individual components required to build this posterior. Given that previous chapters have covered the necessary background on perturbation theory and bias expansion, our focus here will be on the treatment of the initial density field and the specifics of the likelihood function.

A key benefit of the field-level approach is that it does not rely on any compression functions, instead, it extracts the information directly from the field. This is done by writing down a joint posterior for the initial density field, cosmological parameters, and nuisance parameters (bias parameters and stochastic amplitudes). A crucial ingredient in this posterior is the likelihood function of observing a tracer field  $\delta_h$  given the evolved matter density field. A likelihood function in the context of the effective field theory (EFT) of large scale structures [18, 30] has been derived in [29, 52, 112]. A significant feature of the EFT likelihood is that it allows us to constrain the parameter of interest at the field level. Furthermore, Ref. [112] has shown that the forward model combined with the EFT likelihood naturally includes the BAO reconstruction. In addition to the BAO scale, EFT-based field-level inference results have been applied to the  $\sigma_8$  parameter in [52, 71, 90, 110] as well as the growth rate  $f$  in [130]. Moreover, Ref. [21] (“Beyond-2pt challenge”) recently presented the results of a variety of inference methods applied to cosmology-blinded mock catalogs constructed by populating dark matter halos with a halo occupation distribution, where field-level inference based on `LEFTfield` showed very competitive results for  $\sigma_8$  inference.

In the final section of the chapter, we will briefly sketch how the forward model we are considering is implanted in the `LEFTfield` code. This chapter is based on [11] and [12].

## 6.1 EFT based Forward Model

The idea of forward modeling is involves starting from the initial conditions and then model the tracer overdensity field  $\delta_g$  at late times. The latter is defined as

$$\delta_g(\mathbf{x}, \eta) \equiv \frac{n_g(\mathbf{x}, \eta)}{\bar{n}_g(\eta)} - 1 = \delta_{g,\text{det}}(\mathbf{x}, \eta) + \epsilon(\mathbf{x}, \eta), \quad (6.1)$$

where  $\eta$  is the conformal time,  $n_g(\mathbf{x}, \eta)$  is the comoving rest-frame tracer density and  $\bar{n}_g(\eta)$  is its position-independent mean.  $\delta_{g,\text{det}}(\mathbf{x}, \eta)$  is the deterministic part predicted by the forward model and  $\epsilon(\mathbf{x}, \eta)$  is the stochastic (noise) contribution.

The forward model employed here was introduced in [112]. The main object of this model is a joint posterior for the initial density field  $\delta_{\text{in}}$ , cosmological parameters  $\theta$  and “nuisance” parameters (bias parameters  $\{b_O\}$  and stochastic amplitudes  $\sigma$ ) given the data, i.e.  $P(\delta_{\text{in}}, \theta, \{b_O\}, \sigma | \delta_g)$ . There are four ingredients to this posterior:

- Prior on the initial conditions
- Forward model for matter and gravity
- Bias model
- Likelihood.

The forward model we employ is based on EFTofLSS. Specifically, our forward model for matter and gravity uses third-order Lagrangian perturbation theory (see Sec. 3.3), which we combine with second- and third-order Lagrangian bias expansions (see Sec. 4).

Relying on the EFT approach means that we have a natural occurrence of a cutoff scale  $\Lambda$ . While in analytical loop calculations one typically sends this cutoff to infinity for convenience, it is necessary to keep it finite when using a field-level forward model [111], in close analogy to lattice field theory (see [107] for a discussion of the connection between both conventions). Thus, in our case,  $\Lambda$  denotes the maximum wave number included in the analysis, and  $\Lambda$  is restricted to be smaller than the nonlinearity scale at which the EFTofLSS breaks down. In practice, the cutoff  $\Lambda_{\text{in}}$  is applied in the initial conditions (i.e., *in the free field*), as well as in the likelihood evaluation to only include the modes in the data that are below the cutoff  $k_{\text{max}}^{\text{like}}$ ; specifically, throughout this paper we keep  $\Lambda_{\text{in}} = k_{\text{max}}^{\text{like}} = \Lambda$ .

In the following sections, we will elaborate on the treatment of the initial density field and provide more details about the likelihood model used in our analysis.

### 6.1.1 Initial density field

A single realization of the initial density field is of the form

$$\delta_{\text{in}}(\mathbf{k}, \hat{s}) = W_\Lambda(k) \sqrt{P_L(k)} \hat{s}(\mathbf{k}), \quad (6.2)$$

where  $W_\Lambda(k)$  is a sharp- $k$  filter which we use to ensure the proper renormalization of the evolution of large-scale modes,  $P_L$  is the linear power spectrum, and  $\hat{s}(\mathbf{k})$  is the unit Gaussian field which we use to represent the normalized initial conditions (sometimes loosely referred to as “phases”). Depending on the choice of prior for  $\hat{s}$ , we distinguish between two scenarios,

$$\hat{s}(\mathbf{x}) = \begin{cases} \delta_D(\hat{s} - \hat{s}_{\text{true}}), & \text{FixedIC,} \\ \mathcal{N}(0, 1), & \text{FreeIC.} \end{cases} \quad (6.3)$$

In the case when  $\hat{s}$  is fixed to ground truth, we are talking about FixedIC case. Alternatively, the case when the Gaussian prior for  $\hat{s}$  is chosen, we denote as FreeIC. In this chapter, we will focus exclusively on the FixedIC case.

### Changing the size of the BAO scale

As we have seen the Sec. 5.3, the BAO is normally used to infer the angular diameter distance to a given observed redshift by comparing the predicted scale of the BAO feature to the data for a given assumed distance. This kind of approach is not suitable in our case since we are working with simulations on a cubic box with periodic boundary conditions. Modifying the fiducial distance in such a case would result in changes to the comoving volume of the data, and violate the periodic boundary conditions of the simulated catalog. To avoid these significant complications, we adopt a different approach, essentially rescaling the predicted comoving sound horizon.

We want to constrain the BAO scale  $r_s$  just from the information available in the oscillatory part of the power spectrum, without referring to its broad-band part. This is because the broad-band power spectrum depends on other cosmological parameters as well. One possible way to constrain  $r_s$  from the power spectrum is by varying the baryon density  $\omega_b$  and checking which value agrees the best with the data. However, varying the value of  $\omega_b$  changes not only the oscillatory part of the power spectrum, but also its broad-band. Therefore, this approach is not suitable.

Instead, we approximate the linear matter power spectrum as<sup>1</sup>

$$P_L(k, \beta) = P_{L,\text{sm}}(k)[1 + A \sin(k\beta r_{\text{fid}} + \phi) \exp(-k/k_D)], \quad (6.4)$$

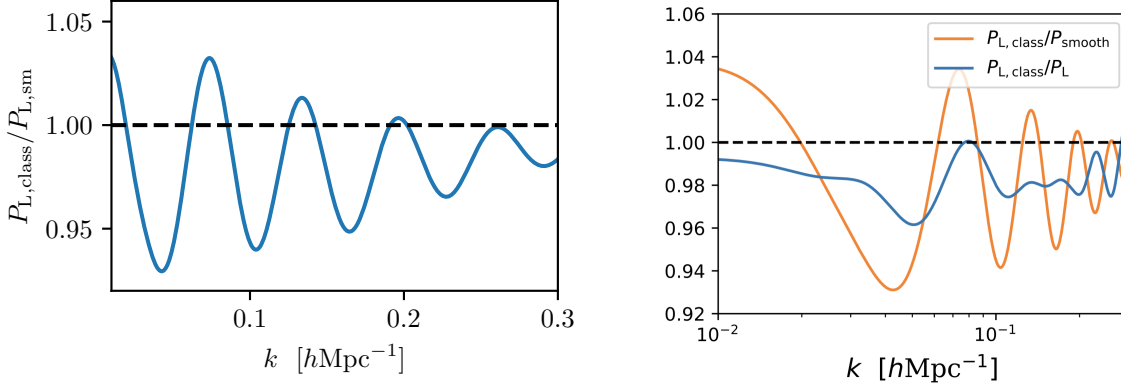
where  $A$ ,  $\phi$  and  $k_D$  are constants and  $r_{\text{fid}}$  is the fiducial BAO scale. Through this equation, we separate the broad band part of the power spectrum, described with the function  $P_{L,\text{sm}}(k)$ , from its oscillatory feature. In the oscillatory feature, we recognize the contribution  $\sin(k\beta r_{\text{fid}})$  describing the baryon acoustic oscillations and the exponential envelope corresponding to the primordial photon diffusion, or Silk damping. The Silk damping term absorbs all the physics that is not captured within the fluid approximation to the baryon-photon system before recombination.

Finally, we introduced the factor  $\beta$  as

$$\beta = \frac{r_s}{r_{\text{fid}}}. \quad (6.5)$$

---

<sup>1</sup>Inference results in this section were obtained with  $P_L(k, \beta) = P_{L,\text{sm}}(k)[1 + A \sin(k\beta r_{\text{fid}}) \exp(-k/k_D)]$



(a) Ratio of the linear power spectrum obtained from CLASS and the best fit for  $P_{L,\text{sm}}$ . (b) Ratio of the linear power spectrum from CLASS and the best fit for  $P_L$  from Eq. (6.4).

Figure 6.1: Comparing the linear power spectrum to the power spectrum approximation.

By changing  $\beta$ , we are changing the size of the BAO scale  $r_s$  to match the data while keeping the distances fixed. Most importantly, changing  $\beta$  will result in changes in the oscillatory part of the power spectrum while keeping its overall shape intact. It is worth nothing that, since the BAO scale was imprinted in the power spectrum during the early Universe, varying it in the initial (linear) density field is the physically correct approach.

The function  $P_{L,\text{sm}}(k)$  can be written in the form

$$P_{L,\text{sm}}(k) = N \left( \frac{k}{k_p} \right)^{n_s} T^2(k), \quad (6.6)$$

where  $N$  is a normalization constant that is proportional to the primordial normalization  $\mathcal{A}_s$  times the growth factor squared,  $k_p$  is the pivot scale, and  $T(k)$  is the “no-wiggle” transfer function which we take from Ref. [49]. We found the value of  $N$ ,  $k_D$ ,  $\phi$  and  $A$  by fitting Eq. (6.6) to the linear power spectrum produced by the CLASS code [75]. Fig. 6.1a shows the ratio of the CLASS power spectrum to  $P_{L,\text{sm}}(k)$ . We can clearly see the damped oscillation in the BAO range which indicates that  $P_{L,\text{sm}}$  really does describe the smooth power spectrum with no BAO wiggles. Fig. 6.1b shows the ratio of the CLASS power spectrum to the power spectrum approximated by Eq. (6.4). While some residual wiggles are visible in the plot, they are suppressed at high  $k$ , where most of the constraints come from. Therefore, we can conclude that Eq. (6.4) is a good approximation of the linear power spectrum and we can use it for the BAO scale inference.

Given the known fiducial power spectrum, i.e. the power spectrum from which the initial conditions of the N-body simulations were drawn, it is easy to find the power spectrum with a different BAO scale, using Eq. (6.4). We introduce the factor  $f(k, \beta)$  as

$$f^2(k, \beta) = \frac{P_L(k, \beta)}{P_{\text{fid}}(k)} = \frac{1 + A \sin(k\beta r_{\text{fid}}) \exp(-k/k_D)}{1 + A \sin(kr_{\text{fid}}) \exp(-k/k_D)}. \quad (6.7)$$

Notice that  $f(k, 1) = 1$ . From  $f(k, \beta)$ , it is straightforward to find the relationship between the fiducial and rescaled linear density fields

$$\delta_\beta(k, \beta) = f(k, \beta)\delta_{\text{fid}}(k). \quad (6.8)$$

To recap,  $\delta_\beta$  is the linear matter density field with all fiducial phases but for which the BAO scale is of the size  $r_s = \beta r_{\text{fid}}$ . Throughout the chapter we will be using different  $\delta_\beta$  as the initial fields for our forward model.

### 6.1.2 EFT likelihood

By construction, our model does not capture modes above the cutoff  $\Lambda$  in the initial conditions. These modes introduce scatter around the mean relation  $\delta_{g,\text{det}}$ , which is described by the stochastic contribution expressed as the field  $\epsilon$  in Eq. (6.1). The purpose of the field-level EFT likelihood is to absorb this stochastic contribution. Considering that  $\epsilon$  originates from integrating out numerous independent  $k$  modes, the central limit theorem ensures that this field is Gaussian at leading order. Furthermore, owing to the local nature of tracer formation, the power spectrum of  $\epsilon$  is constant at leading order, with corrections scaling as  $k^2$ . These properties lead to the formulation of the EFT likelihood

$$\ln \mathcal{L}_{\text{EFT}}(\delta_g | \hat{s}, \theta, \{b_O\}, \sigma) = -\frac{1}{2} \sum_{k \leq \Lambda} \left[ \ln[2\pi\sigma^2(k)] + \frac{1}{\sigma^2(k)} |\delta_g(\mathbf{k}) - \delta_{g,\text{det}}[\hat{s}, \theta, \{b_O\}](\mathbf{k})|^2 \right]. \quad (6.9)$$

where  $\sigma^2$  represents the noise power spectrum, formulated in a way that ensures its positive definiteness,

$$\sigma^2(k) = \sigma_\epsilon^2(k)(1 + k^2\sigma_{\epsilon,2})^2. \quad (6.10)$$

The parameter  $\sigma_\epsilon$  is the variance of the noise field  $\epsilon$  on the discrete grid. This quantity is dependent on both the grid size,  $N_g^\Lambda$ , and the box size  $L$ . Its relationship with the noise power spectrum  $P_\epsilon$  is then given by

$$P_\epsilon = \sigma_\epsilon^2 \frac{L^3}{(N_g^\Lambda)^3}. \quad (6.11)$$

The main feature to highlight in the EFT likelihood is that it compares the data  $\delta_g$  and the model  $\delta_{g,\text{det}}$  mode by mode, or voxel by voxel, up to the maximum scale at which we trust the model. This allows the likelihood to access the full spectrum of information within the field.

This likelihood offers a convenient feature: it can be marginalized analytically over the bias parameters. This is possible because under the assumption of Gaussian or uniform priors, the likelihood exhibits a quadratic dependence on the bias coefficients. We will refer to this as the marginalized likelihood. It can be shown that in the case of Gaussian priors (mean  $\mu_{b_O}$  and covariance  $C_{\text{prior}}$ ) on the bias parameters, this marginal likelihood is of the

form [71]

$$\begin{aligned}
-\ln \mathcal{L}(\delta_{d,\Lambda}|\beta, \hat{s}, \sigma_\epsilon) &= \frac{1}{2} \text{tr} \ln A_{OO'} + \frac{1}{2} \text{tr} \ln C_{\text{prior}} + \\
&\quad \frac{1}{2} \sum_{k \neq 0}^{k_{\text{max}}} \left( \ln \sigma_\epsilon^2 + \frac{1}{\sigma_\epsilon^2} |\delta_{d,\Lambda}(k)|^2 \right) - \frac{1}{2} \sum_{\{O, O'\}} B_O (A^{-1})_{OO'} B_{O'}, \\
B_O \equiv B_O[\hat{s}, \beta] &= \sum_{k \neq 0}^{k_{\text{max}}} \frac{\delta_{d,\Lambda}^*(k) O[\hat{s}, \beta](k)}{\sigma_\epsilon^2} + \sum_{O'} (C_{\text{prior}}^{-1})_{OO'} \mu_{b_{O'}}, \\
A_{OO'} \equiv A_{OO'}[\hat{s}, \beta] &= \sum_{k \neq 0}^{k_{\text{max}}} \frac{O^*[\hat{s}, \beta](k) O'[\hat{s}, \beta](k')}{\sigma_\epsilon^2} + (C_{\text{prior}}^{-1})_{OO'}.
\end{aligned} \tag{6.12}$$

Equivalent result can be found for uniform priors, see [52] for more details.

## 6.2 Code Implementation of the forward model

Our forward model is implemented in the `LEFTfield` code.

We start by sampling the initial conditions. We place those on a grid of size  $N_g^\Lambda$ , and multiply them with the square root of the linear power spectrum to obtain the initial field. The size of the initial grid,  $N_g^\Lambda$ , is determined by the requirement to represent all Fourier modes (for the given box size  $L$ ) up to the cutoff  $\Lambda$ . Next, we find the bias operators. This procedure slightly varies between the Eulerian and Lagrangian case.

In the Eulerian case, we construct the LPT displacement to the  $n$ -th order (nLPT). During the construction, to make sure all physical modes are accounted for, we employ a grid of size  $N_g^{n\Lambda}$ , where  $n$  is the maximum perturbative order. We then displace a uniform grid of pseudoparticles to Eulerian space. These pseudoparticles are then assigned (see below) to obtain the Eulerian density field  $\delta$ . This field is subsequently sharp- $k$  filtered as described above, after which the Eulerian bias operators are constructed. We resize the grid appropriately to ensure that all modes entering the likelihood are safe from aliasing.

In the Lagrangian bias case, the set of operators listed in Eq. (4.22) up to the desired order is constructed concurrently with the nLPT displacement. In addition to the uniform-weight grid used to obtain the Eulerian matter density, we also assign particles with weights given by the  $O_L(\mathbf{q})$ , effectively displacing the Lagrangian operators to Eulerian space [110].

The assignment schemes implemented in `LEFTfield` are nearest-grid-point (NGP), cloud-in-cell (CIC), triangular-shaped cloud (TSC), and non-uniform-to-uniform discrete Fourier transform (NUFFT) [14], which we employ as an assignment scheme. The quickest assignment scheme we have implemented is NUFFT, as it converges rapidly with Eulerian grid size thanks to the kernel deconvolution. NUFFT implements the non-uniform-to-uniform discrete Fourier transform [ $f(\mathbf{x}) \rightarrow \tilde{f}(\mathbf{k})$ ] by assigning particle positions  $\mathbf{x}_i$  with weights  $f(\mathbf{x}_i)$  to a supersampled grid (increasing the resolution by a factor typically in the range 1.2 to 2) using a suitable assignment kernel with compact support (of roughly 4 to 16

---

grid cells). It then performs an FFT on the supersampled grid, deconvolves the assignment kernel, and finally performs a grid reduction in Fourier space to yield the desired uniform discrete Fourier transform  $\tilde{f}(\mathbf{k})$ . This method is approximate, but accuracy close to machine precision can be obtained for very reasonable computational effort. When NUFFT is used, for the Eulerian grid size, we choose  $N_g^{\text{Eul}}$  such that the Nyquist frequency corresponds to  $(3/2)\Lambda$ , at which point the density assignment is converged to next-to-leading order [129]. When CIC is used, for the Eulerian grid size, we choose  $N_g^{\text{Eul}}$  such that the Nyquist frequency corresponds to  $2\Lambda$ .



# Chapter 7

## BAO scale inference from biased tracers using the EFT likelihood

*This chapter is adaptation of [11].*

### Abstract

The physical scale corresponding to baryon acoustic oscillations (BAO), the size of the sound horizon at recombination, is precisely determined by CMB experiments. Measuring the apparent size of the BAO scale imprinted in the clustering of galaxies gives us a direct estimate of the angular-diameter distance and the Hubble parameter as a function of redshift. The BAO feature is damped by non-linear structure formation, which reduces the precision with which we can infer the BAO scale from standard galaxy clustering analysis methods. Many methods to undo this damping via the so-called BAO reconstruction have so far been proposed; however, they all rely on backward modeling. In this chapter, we present the first results of isotropic BAO inference from rest-frame halo catalogs using forward modeling combined with the EFT likelihood, in the case where the initial phases of the density field are fixed. We show that the remaining systematic bias is less than 2% when we consider cutoff values of  $\Lambda \leq 0.25 h \text{Mpc}^{-1}$  for all halo samples considered, and below 1% and consistent with zero for all but the most highly biased samples. We also demonstrate that, when compared to the standard power spectrum likelihood approach under the same assumption of fixed phases, the  $1\sigma$  errors associated to the field level inference of the BAO scale are 1.1 to 3.3 times smaller, depending on the value of the cutoff and the halo sample. Our analysis therefore unveils another promising feature of using field-level inference for high-precision cosmology.

## 7.1 Introduction

In this chapter, we perform an unbiased inference of the isotropic BAO scale—referred to simply as the BAO scale—using rest-frame halo catalogs and the EFT likelihood. By relying on simulations, we are able to fix the initial conditions of the linear density field to their true values, effectively minimizing cosmic variance and reducing the size of the error bars.

To gauge what are the improvements from the field level likelihood over standard, power-spectrum-based approaches, we also determine the BAO scale value using a likelihood constructed from the power spectrum. For the predicted power spectrum we do not perform any additional BAO reconstruction; instead, we use the deterministic halo field found from the forward model. This means that the EFT likelihood is still used to constrain the bias parameters in the construction of the predicted power spectrum, but is not used to constrain the BAO scale. On the other hand, our power spectrum covariance takes into account that the phases are fixed to the ground truth, i.e. there is no cosmic variance. Thus, we perform a fair comparison between both methods.

This chapter is organized as follows. Section 7.2 offers an overview of the method used for inferring the BAO scale within the EFT-based approach. In Section 7.3, we apply this approach to determine the BAO scale and compare these results with those obtained from the power spectrum, as discussed in Section 7.4. We conclude in Section 7.5.

## 7.2 Inference method

All numerical results presented here were obtained for a spatially flat  $\Lambda$ CDM cosmology with parameters  $\Omega_m = 0.3$ ,  $\Omega_\Lambda = 0.7$ ,  $h = 0.7$ ,  $n_s = 0.967$  and a box with size  $L = 2000h^{-1}\text{Mpc}$ . We use four halo mass bins in the mass range  $10^{12.5}h^{-1}M_\odot$ – $10^{14.5}h^{-1}M_\odot$ . We present results on two simulation realizations, “run 1” and “run 2”, which differ in their initial phases. In Tab. 7.1, we present the number density of halos in run 1 at different redshifts.

For the forward model, we use third-order LPT combined with second- and third-order bias expansion. As mentioned earlier, we do not sample the initial density field; it is instead fixed to the exact initial conditions used in the N-body simulations within which the halos are identified. To get the initial density with different BAO scales, we apply Eq. (6.8) for a set of values  $\{\beta^i\}$ . The default set spans the range  $[0.8, 1.02]$ ; in all cases, we make sure that the maximum-a-posteriori (MAP) value of  $\beta$  is safely within the range. Fixing the initial phases not only saves the computational time, but it also minimizes the cosmic variance as much as possible resulting in smaller error bars for the inferred value of  $\beta$ .

To find the MAP estimate for  $\beta$ , which we denote as  $\hat{\beta}$ , we use the profile likelihood [145]. For a probability distribution  $P(\beta, \sigma_\varepsilon|\delta_h)$  (recall that the bias coefficients are analytically marginalized over) and parameter  $\beta$ , the profile likelihood is defined as

$$P^{\text{prof}}(\beta) = \max_{\sigma_\varepsilon} [P(\beta, \sigma_\varepsilon|\delta_h)], \quad (7.1)$$

$z$	Mass range [ $\log_{10}(M/h^{-1}M_{\odot})$ ]	$\bar{n}_h$ [(Mpc/h) $^{-3}$ ]
0.0	[12.5 – 13.0]	$7.056\,88 \times 10^{-4}$
0.5	[12.5 – 13.0]	$6.001\,05 \times 10^{-4}$
1.0	[12.5 – 13.0]	$4.744\,83 \times 10^{-4}$
0.0	[13.0 – 13.5]	$3.509\,70 \times 10^{-4}$
0.5	[13.0 – 13.5]	$2.766\,35 \times 10^{-4}$
1.0	[13.0 – 13.5]	$1.884\,50 \times 10^{-4}$
0.0	[13.5 – 14.0]	$1.149\,82 \times 10^{-4}$
0.5	[13.5 – 14.0]	$7.426\,65 \times 10^{-5}$
1.0	[13.5 – 14.0]	$3.767\,61 \times 10^{-5}$
0.0	[14.0 – 14.5]	$2.965\,94 \times 10^{-5}$
0.5	[14.0 – 14.5]	$1.331\,26 \times 10^{-5}$
1.0	[14.0 – 14.5]	$3.941\,75 \times 10^{-6}$

Table 7.1: Number density of halos in run 1 at different redshifts.

where the parameter  $\sigma_{\varepsilon}$  has been profiled out.

For a fixed  $\Lambda$ , halo sample, redshift and  $\beta^i$  we maximize the profile likelihood using the MINUIT minimizer [60]. In this way we obtain a set  $\{\beta^i, -2 \ln P^{\text{prof}}(\beta^i)\}$  which is nicely fit by a parabola for all halo samples and all cutoffs. An example of this parabola for two different cutoffs is shown in Fig. 7.1, where the elements of the set  $\{\beta^i, -2 \ln P^{\text{prof}}(\beta^i)\}$  are represented with orange dots and the blue line corresponds to the parabolic fit. The MAP value  $\hat{\beta}$  is located at the minimum of the best fit parabola. The estimated 68% confidence-level error on  $\hat{\beta}$  is given by the inverse square root curvature of the parabolic fit.

## 7.3 Field-Level Results

In this section, we show the results of applying the EFT likelihood to the halo catalogs. We start by comparing the results for two different bias orders—second and third order—at fixed redshift  $z = 0$ . Fig. 7.2 shows the deviation of the MAP values  $\hat{\beta}$  from 1 as a function of  $\Lambda$  for different halo mass ranges. For all of halo mass bins except the highest one,  $\hat{\beta}$  is consistent with being unbiased within the error bar obtained from the profile likelihood. Moreover,  $\hat{\beta}$  is moving closer to 1 as  $\Lambda$  is increased, consistent with the shrinking error bar as more  $k$  modes are being included in the likelihood and forward model. We notice that the MAP values  $\hat{\beta}$  are closer to 1 for the third order bias expansion than in the case of second order, for every halo sample. This indicates that the systematic error in  $\hat{\beta}$  in the 3rd order bias case is reduced, as expected if one is in the converging regime of the EFT. Therefore, in the rest of the chapter, we focus only on the 3rd order bias expansion.

Fig. 7.3 depicts the value of the  $1\sigma$  error bar,  $\sigma_F(\hat{\beta})$ , for the field-level inference (as

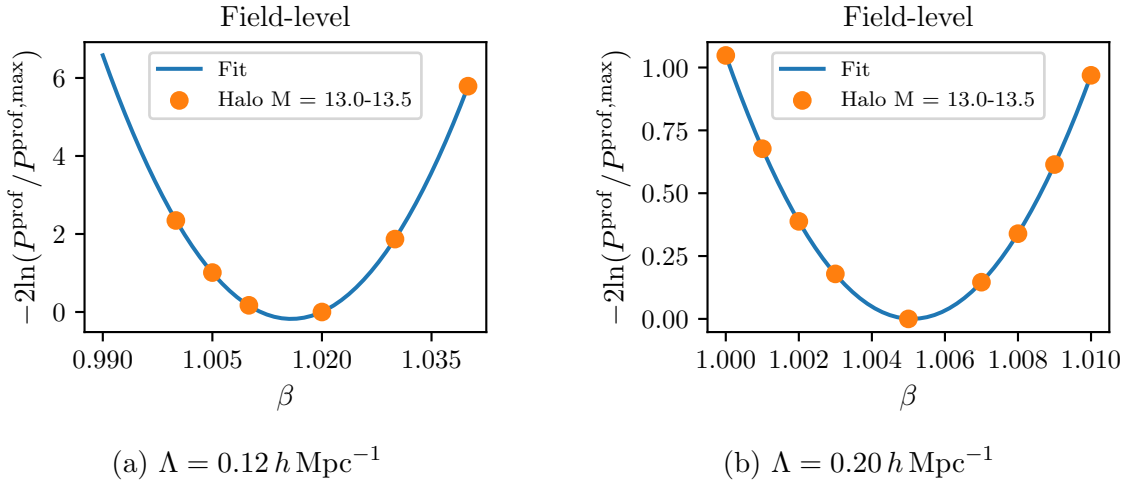


Figure 7.1: Profile likelihood  $-2 \ln P^{\text{prof}}$  plotted as a function of  $\beta$  for two different cut-offs  $\Lambda$  at  $z = 0$ . The blue line shows the parabolic fit which was used to find the maximum-a-posteriori value  $\hat{\beta}$  and its error  $\sigma(\hat{\beta})$ .

emphasized by the subscript  $F$ ) as a function of  $\Lambda$  for the 3rd bias order for both runs 1 and 2. We see that  $\sigma_F(\hat{\beta})$  is smoothly decreasing with increasing  $\Lambda$ . Since our initial conditions are exactly the ones used in the halo simulations, the statistical uncertainty  $\sigma_F(\hat{\beta})$  is only sourced by the halo stochasticity which appears in the EFT likelihood. Note that we do expect the  $\sigma_F(\hat{\beta})$  results to change once we start sampling the initial phases instead of keeping them fixed.

We also notice that the  $\sigma_F(\hat{\beta})$  values do not change much between the different halo samples. This trend can be understood by inspecting how the numerator and denominator of Eq. (6.9) change with halo mass. On the one hand, more massive halos are rarer, and hence have larger noise (stochasticity), i.e. larger  $\sigma_\varepsilon^2$  in the denominator. On the other hand, higher-mass halos are more biased, and hence show a stronger clustering signal. Hence the numerator also increases with halo mass. As a consequence, the ratio of both quantities is actually roughly constant, so that we get a similar  $\sigma_F(\hat{\beta})$  for all halo bins considered. Notice that this result only applies to the *fixed-phase* study done here.

Next, we look at the results found at different redshifts. Fig. 7.4 and Fig. 7.5 show the value of  $\hat{\beta}$  as a function of  $\Lambda$  at redshifts  $z = 0.0, 0.5, 1.0$  for run 1 and run 2, respectively. For run 1, these results are also summarized in Tab. 7.2 for a fixed cutoff,  $\Lambda = 0.16 h \text{ Mpc}^{-1}$ . We find that the remaining systematic bias is very low across all the redshifts and mass ranges. Even for this cutoff, the bias is less than 1% at  $z = 0$  for all mass ranges and the results generally keep improving with growing  $\Lambda$ . If we look across all redshifts, it is clear that the remaining bias is still below 2%, and in fact consistent with zero, for most of the cases. It goes over 2% only for the most massive halos which are very rare at higher redshifts. Those halo samples would most likely benefit from going to higher bias orders in the bias expansion.

$z$	Mass range $\log_{10}(M/h^{-1}M_{\odot})$	$100(\hat{\beta} - 1)$	$\sigma_{\varepsilon}$
0.0	[12.5 – 13.0]	$1.08 \pm 0.74$	0.463
0.5	[12.5 – 13.0]	$-0.47 \pm 0.71$	0.471
1.0	[12.5 – 13.0]	$-0.09 \pm 0.68$	0.494
0.0	[13.0 – 13.5]	$0.56 \pm 0.78$	0.625
0.5	[13.0 – 13.5]	$0.40 \pm 0.70$	0.647
1.0	[13.0 – 13.5]	$0.43 \pm 0.67$	0.735
0.0	[13.5 – 14.0]	$-0.89 \pm 0.86$	0.992
0.5	[13.5 – 14.0]	$-0.28 \pm 0.72$	1.163
1.0	[13.5 – 14.0]	$0.86 \pm 0.75$	1.582
0.0	[14.0 – 14.5]	$0.80 \pm 0.80$	1.785
0.5	[14.0 – 14.5]	$-2.73 \pm 0.80$	2.572
1.0	[14.0 – 14.5]	$-2.29 \pm 0.97$	4.926

Table 7.2: Summary of the results found using the field-level EFT likelihood at the cutoff  $\Lambda = 0.16 h \text{ Mpc}^{-1}$  for different redshifts and halo mass bins.

From Fig. 7.4 and Fig. 7.5 we notice that the remaining systematic bias in  $\hat{\beta}$  is increasing with growing redshift. This occurrence is counter-intuitive, since from perturbation theory we would expect a better performance at higher redshifts where perturbation theory extends to higher wavenumbers. A similar trend was noticed with inference of  $\sigma_8$  from the halo catalogues described in [111]. It was found there that this trend is caused by the higher-order bias terms. Although the higher-order bias terms are suppressed by powers of the normalized growth factor  $D_{\text{norm}}(z) = D(z)/D(0)$  at higher redshifts, it is possible that the increase in their coefficients with redshift more than compensates for this suppression. To check if this was the case for us as well, we use the test suggested in [111] which was based on the assumption from [43] that the higher order bias terms can be approximated as being a function of  $(b_1 - 1)D_{\text{norm}}(z)$ . Results are shown in Fig. 7.6, where we plotted the  $|\hat{\beta} - 1|$  values for all halo mass bins and redshifts against  $(b_1 - 1)D_{\text{norm}}(z)$ . There is a hint of a correlation between  $|\hat{\beta} - 1|$  and  $(b_1 - 1)D_{\text{norm}}(z)$ , although all but one points are consistent with  $\hat{\beta} = 1$  within one sigma.

Let us also comment on the limits of the cutoff we are using. For matter, the EFT is under perturbative control for  $\Lambda \lesssim 0.25 h \text{ Mpc}^{-1}$  at  $z = 0$ . For highly biased tracers, the cutoff is reduced due to the growing size of bias parameters at higher orders. Thus, we are going beyond that limit, and not all of our values of  $\Lambda$  are strictly under perturbative control. However, because the BAO is an oscillatory feature, while higher-order corrections are expected to be smooth functions of  $k$ , the BAO inference seems to be still robust at these high  $k$ . We leave a more systematic investigation of this important issue to future work.

## 7.4 Comparing the field-level results to the power spectrum approach

Having presented the results of constraining the BAO scale using the EFT likelihood, we now turn to comparing these results to a more traditional BAO inference approach based on the power spectrum.

### 7.4.1 Power spectrum likelihood

Care is needed in order to ensure that the comparison we are making is valid, since in the EFT approach we use fixed phases in the matter density field. Therefore, we adopt the following Gaussian likelihood for the halo power spectrum:

$$-2 \ln \mathcal{L}[P_h(k)|\delta_{\text{in}}, \{b_O\}, P_\varepsilon] = \sum_k^{k_{\text{max}}} \frac{[P_h(k) - P_\varepsilon - P_{\text{det}}(k|\delta_{\text{in}}, \beta, \{b_O\})]^2}{\text{Var}_{\text{fix}}[P_h(k)]}. \quad (7.2)$$

Here,  $P_{\text{det}}(k|\delta_{\text{in}}, \beta, \{b_O\})$  is the power spectrum of the deterministic halo field found using the same forward model as in EFT case for a fixed  $\beta$  value;  $P_h(k)$  is the measured halo power spectrum,  $m_k$  is the number of modes in a wavenumber bin, and  $P_\varepsilon$  is the noise spectrum. Notice that the covariance appearing in the numerator of the likelihood,  $\text{Var}_{\text{fix}}[P_h(k)]$ , is modified to reflect the fact that we are using fixed phases. The derivation of the power spectrum covariance for fixed phases can be found in Appendix A and its final form is given in Eq. (A.18). It is also important to note that we are not performing any additional BAO reconstruction on the halo data, but comparing the halo power spectrum directly with the theory predictions from the full forward model. Therefore the comparison we are making is at the level of likelihoods: the EFT likelihood is performing at the level of the field, while the likelihood in Eq. (7.2) compresses the data to the power spectrum in bins of  $k$ . Both likelihoods however consistently assume fixed initial conditions.

To find the best fit for  $\beta$ , we use the following procedure for different values  $\beta_i$ . We start by finding the initial matter fields with the BAO scales  $r_s = \beta_i r_{\text{fid}}$  using Eq. (6.8) as in the field-level likelihood calculations. Once we have the linear matter density field  $\delta_{\text{in}}(k, \beta_i)$ , we use the 3LPT forward model to generate the evolved matter field  $\delta(k, \beta) = \delta_{\text{fwd}}[\delta_{\text{in}}(k, \beta_i)]$ , where we set all modes with  $k > \Lambda$  to zero. For the bias operators, we use the same bias model as in the field-level case. The MAP for the bias parameters is found by maximizing the EFT likelihood. We keep one bias parameter free at a time and marginalize over all other bias coefficients. Once we found the MAP value for that parameter, we move on and repeat the procedure for the remaining ones. This gives us the deterministic halo field whose power spectrum  $P_{\text{det}}(k|\delta_{\text{in}}, \beta, \{b_O\})$  is straightforward to measure in the same  $k$  bins as the halo sample.

We now turn to the determination of  $P_\varepsilon$ . Ideally, one would fit for this together with  $\beta$  and the bias parameters. In our simplified analysis, we only fit  $P_\varepsilon$ , and use the same noise spectrum value  $P_\varepsilon$  across all  $\Lambda$  and  $\beta$  values. This value is found for  $\Lambda = 0.2 h\text{Mpc}^{-1}$

$z$	Mass range $\log_{10}(M/h^{-1}M_{\odot})$	$100(\hat{\beta} - 1)$	$b_1$
0.0	[12.5 – 13.0]	$1.20 \pm 0.90$	0.833
0.5	[12.5 – 13.0]	$1.87 \pm 0.79$	1.266
1.0	[12.5 – 13.0]	$1.32 \pm 0.73$	1.901
0.0	[13.0 – 13.5]	$4.80 \pm 0.96$	1.236
0.5	[13.0 – 13.5]	$0.79 \pm 0.94$	1.973
1.0	[13.0 – 13.5]	$-2.01 \pm 0.81$	2.892
0.0	[13.5 – 14.0]	$2.27 \pm 1.27$	1.996
0.5	[13.5 – 14.0]	$1.77 \pm 1.01$	3.129
1.0	[13.5 – 14.0]	$1.41 \pm 0.88$	3.994
0.0	[14.0 – 14.5]	$1.18 \pm 1.46$	3.416

Table 7.3: MAP values of  $\beta$  for cutoff  $\Lambda = 0.16 h \text{ Mpc}^{-1}$  inferred from the power spectrum likelihood, at different redshifts for different halo mass ranges.

and  $\beta = 1.00$  by fitting the difference  $P_h(k) - P_{\text{det}}(k|\delta_{\text{in}}, \beta = 1, \{b_O\})$  to a constant, using  $w = 1/\sigma_w$  as the weight where  $\sigma_w = |P_h - P_{\text{det}}|/\sqrt{2/m_k}$ . Fitting the noise separately from bias terms and  $\beta$  leaves us with some uncertainties in its estimate. We roughly estimate this uncertainty by repeating the same analysis for run 2 halo samples, resulting in values of  $P_{\varepsilon}$  that differ by around 20%, which results in a corresponding 20% shift in the  $1\sigma$  error for  $\hat{\beta}$ . We conclude that our results for the latter carry an uncertainty of  $\sim 20\%$ . This is sufficient for the approximate comparison we are aiming for in this chapter. We aim to improve this in future work.

Finally, by inserting  $P_{\text{det}}(k|\delta_{\text{in}}, \beta_i, \{b_O\})$  and  $P_{\varepsilon}$  in Eq. (7.2), we find the likelihood value for each  $\beta_i$ . Repeating this procedure at fixed halo sample, redshift and  $\Lambda$ , leads to a set  $\{\beta^i, -2 \ln P^{\text{prof}}(\beta^i)\}$ , which is nicely fit by a parabola. An example of this parabola fit is shown in Fig. 7.7.  $\hat{\beta}$  and  $\sigma_{PS}(\hat{\beta})$ , the value of the  $1\sigma$  error bar for the power spectrum inference, are found as the location of the minimum and the inverse square root of the parabolic fit, respectively.

## 7.4.2 Results

We now turn to the results for MAP.  $\hat{\beta}$  is found using the likelihood given in Eq. (7.2). The residual values of  $\hat{\beta}$  as a function of  $\Lambda$  at the three different redshifts are shown in Fig. 7.8. For the most massive halo range  $\log_{10}(M/h^{-1}M_{\odot}) = 14.0 - 14.5$ , we show results only at redshift zero. For this halo range at higher redshifts, the set  $\{\beta^i, -2 \ln P^{\text{prof}}(\beta^i)\}$  does not yield a well-defined maximum. We also exclude all the samples for which the MINUIT algorithm does not converge for the bias coefficients due to a poor signal to noise ratio.

The quantitative results are summarized in Tab. 7.3. We see that, for most of the samples, the residual bias in  $\hat{\beta}$  is between 1.20% and 2.3%. The MAP values of the linear bias parameter  $b_1$  are also listed in the table. We notice that, for a fixed mass bin,  $b_1$  is increasing with halo mass and redshift as is expected. In Fig. 7.9, we show  $\sigma_{PS}(\hat{\beta})$  as a

function of  $\Lambda$  at redshift  $z = 0$ . While for the field-level likelihood  $\sigma_F(\hat{\beta})$  reduces about 2.4 times from  $\Lambda = 0.1 h \text{ Mpc}^{-1}$  to  $\Lambda = 0.2 h \text{ Mpc}^{-1}$ , here we do not see such a trend. Instead,  $\sigma_{PS}(\hat{\beta})$  stays fairly constant across all  $\Lambda$  for the power spectrum likelihood. This is presumably because the field-level likelihood can still make use of the phase information at wavenumbers for which the power spectrum likelihood is already dominated by the noise  $P_\varepsilon$ .

The most interesting result is Fig. 7.10, which compares the error on  $\hat{\beta}$  from the power spectrum approach,  $\sigma_{PS}(\hat{\beta})$ , to the one from the field level approach,  $\sigma_F(\hat{\beta})$ . This ratio is shown for three different halo mass ranges at three different redshifts. For smaller cutoffs, both likelihoods give similar results, which is the expected result if the data ( $\delta_h$ ) are well approximated as a Gaussian random field. However, as  $\Lambda$  grows, the EFT likelihood starts outperforming the power spectrum based likelihood. At the highest  $\Lambda$  considered, the  $\sigma_F(\hat{\beta})$  value is around 2.5 times smaller than  $\sigma_{PS}(\hat{\beta})$ . The field-level EFT likelihood performs better because it operates at the level of the field. This means that it includes not only all the information coming from the power spectrum, but also information from the  $N$ -point functions of arbitrarily high orders. Concretely in the case of the BAO, the field-level likelihood knows about the bulk flow field, and can thus compare the expected BAO scale at a given location with the data. The power spectrum on the other hand is averaged over all locations, and thus suffers from the damping of the BAO peak [94, 124]. Thus, the fact that the field-level likelihood outperforms the power spectrum based one comes as no surprise.

Finally, note that we have fixed the bias coefficients in the theory prediction for the power spectrum to the values obtained from the field-level likelihood. In practice, those would have to be marginalized over in a power spectrum analysis.

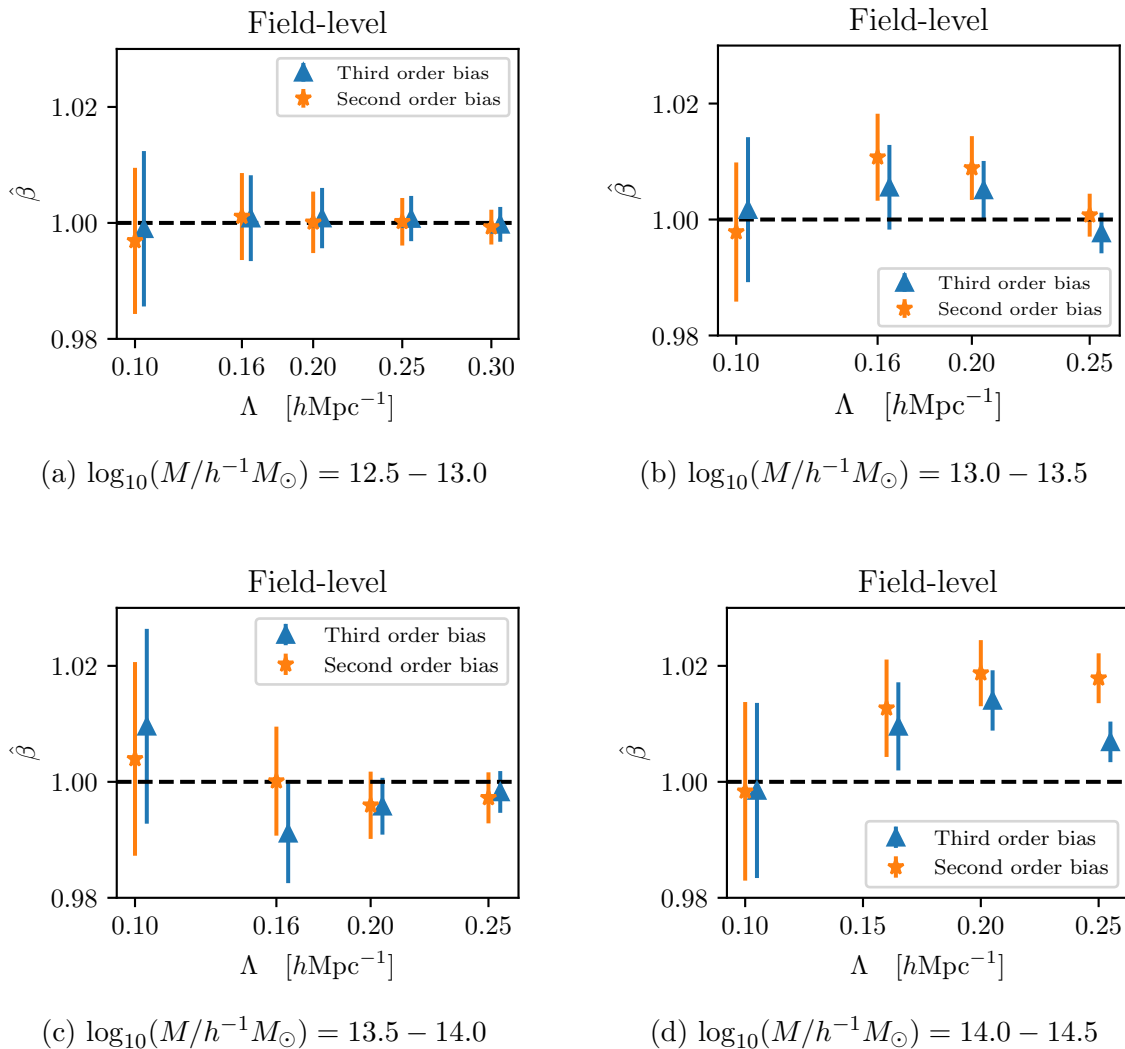


Figure 7.2: MAP value  $\hat{\beta}$  found using the EFT likelihood for two bias orders at  $z = 0$ . The different sub-figures show four different mass ranges.

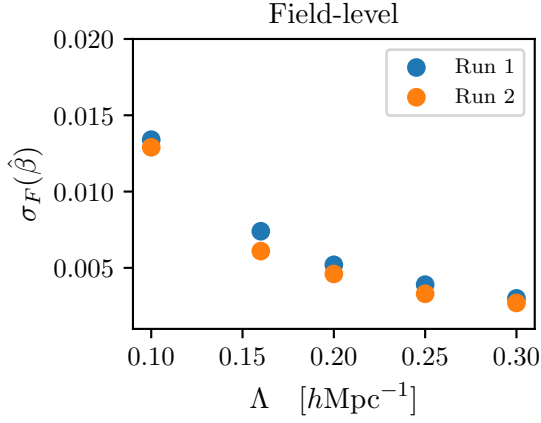
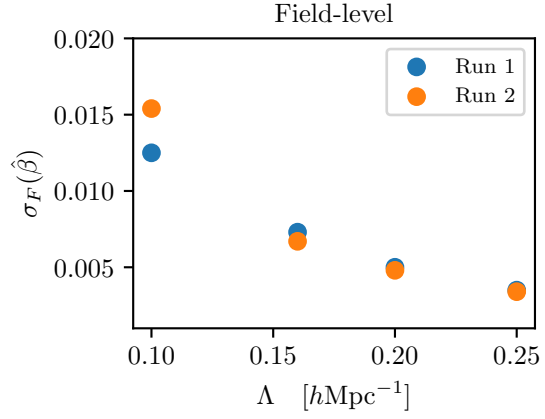
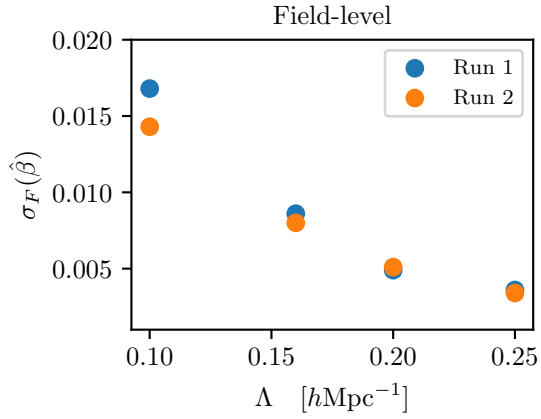
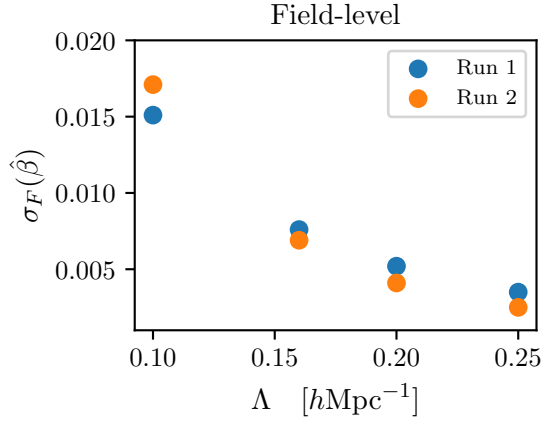
(a)  $\log_{10}(M/h^{-1}M_{\odot}) = 12.5 - 13.0$ (b)  $\log_{10}(M/h^{-1}M_{\odot}) = 13.0 - 13.5$ (c)  $\log_{10}(M/h^{-1}M_{\odot}) = 13.5 - 14.0$ (d)  $\log_{10}(M/h^{-1}M_{\odot}) = 14.0 - 14.5$ 

Figure 7.3:  $\sigma_F(\hat{\beta})$  values as a function of  $\Lambda$  at  $z = 0$ . Different sub-figures show four different mass ranges.

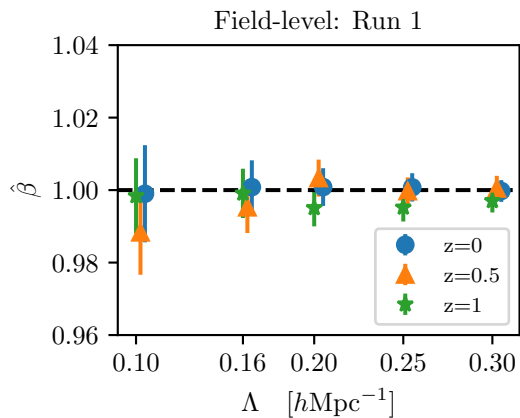
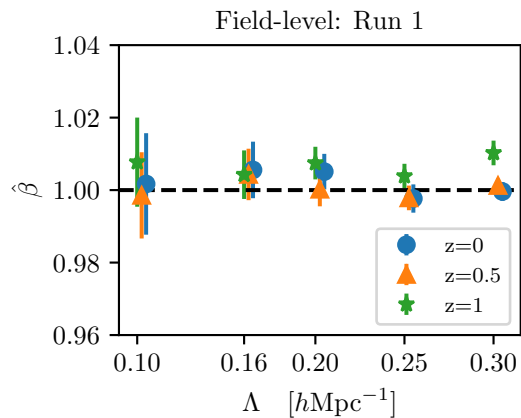
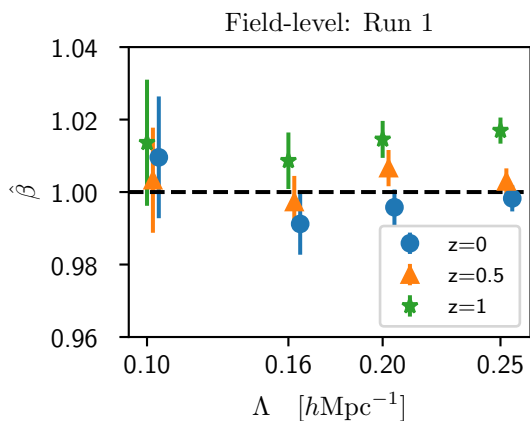
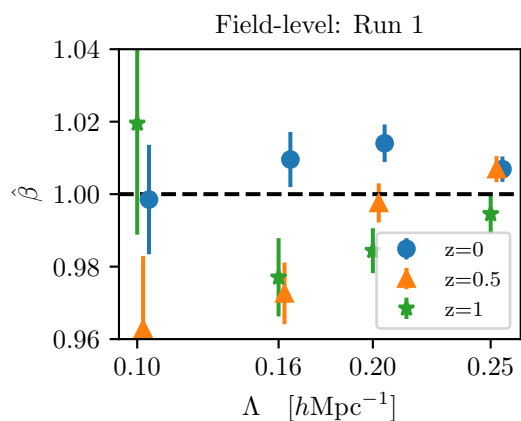
(a)  $\log_{10}(M/h^{-1}M_{\odot}) = 12.5 - 13.0$ (b)  $\log_{10}(M/h^{-1}M_{\odot}) = 13.0 - 13.5$ (c)  $\log_{10}(M/h^{-1}M_{\odot}) = 13.5 - 14.0$ (d)  $\log_{10}(M/h^{-1}M_{\odot}) = 14.0 - 14.5$ 

Figure 7.4: MAP values for  $\beta$  using the EFT likelihood found at different redshifts for run 1. Different panels show four different mass ranges at three different redshifts each.

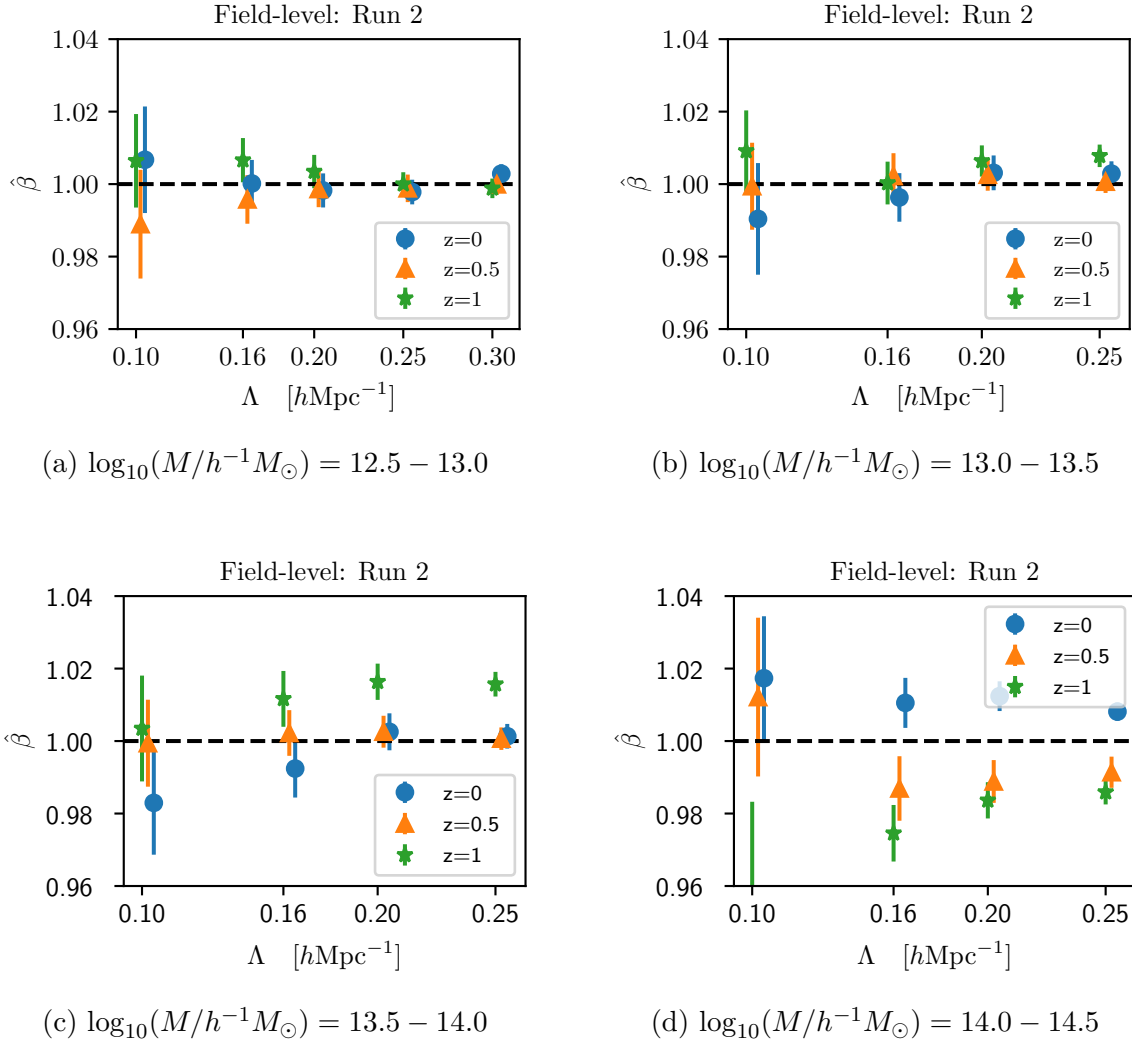


Figure 7.5: MAP values for  $\beta$  using the EFT likelihood found at different redshifts for run 2. Different panels show four different mass ranges at three different redshifts each.

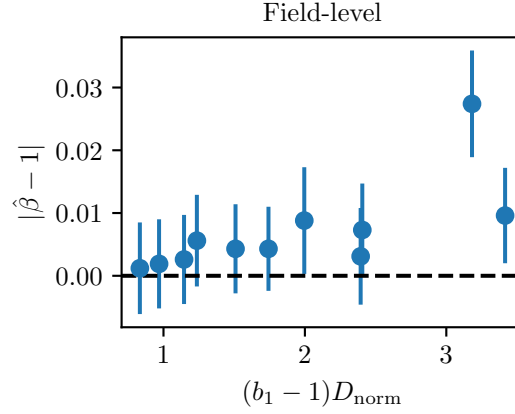


Figure 7.6: MAP values for  $|\hat{\beta} - 1|$  found at the cutoff  $\Lambda = 0.16 h \text{ Mpc}^{-1}$  for all halo mass bins and redshifts against  $(b_1 - 1)D_{\text{norm}}(z)$ , where  $D_{\text{norm}}(z) = D(z)/D(0)$ .

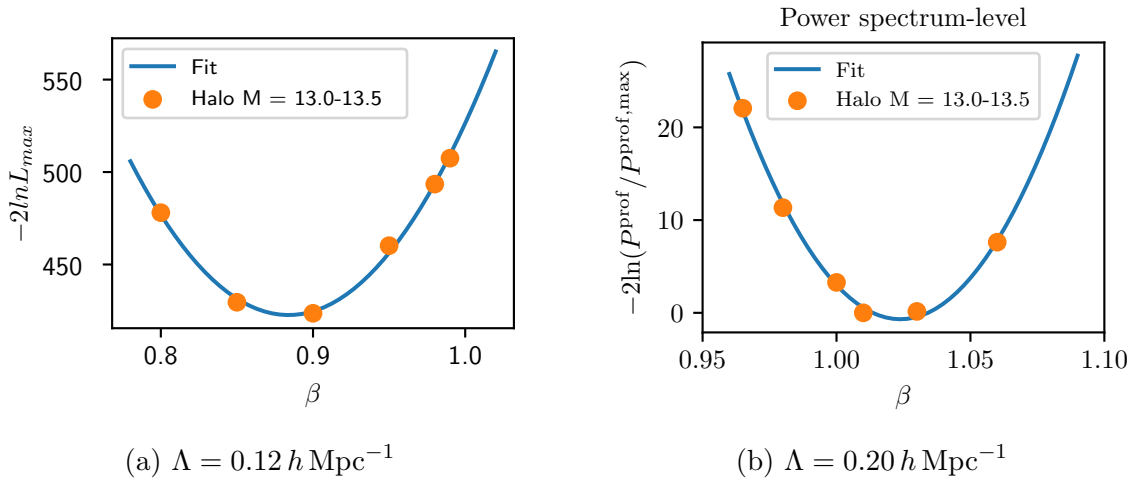


Figure 7.7: Profile likelihood  $-2 \ln P^{\text{prof}}$  for the power spectrum, plotted as a function of  $\beta$  for two different cutoffs  $\Lambda$  at  $z = 0$ . The blue line shows the parabolic fit which was used to find MAP  $\hat{\beta}$  and  $\sigma_{PS}(\hat{\beta})$  error.

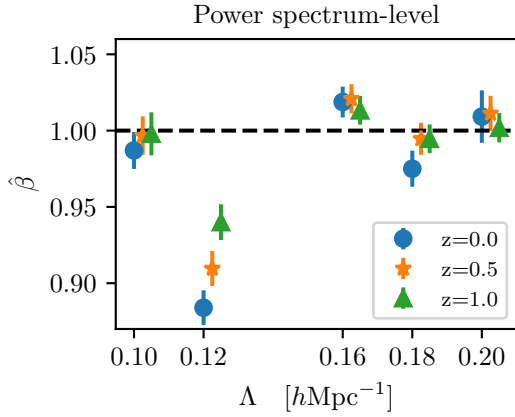
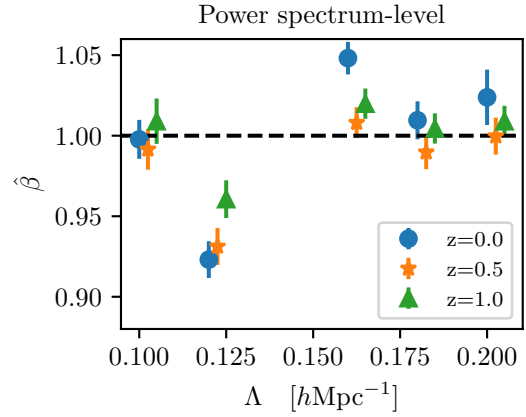
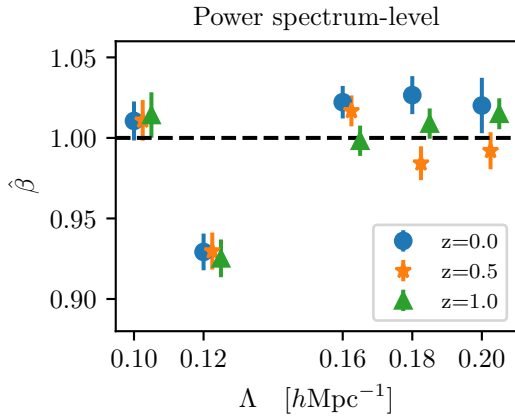
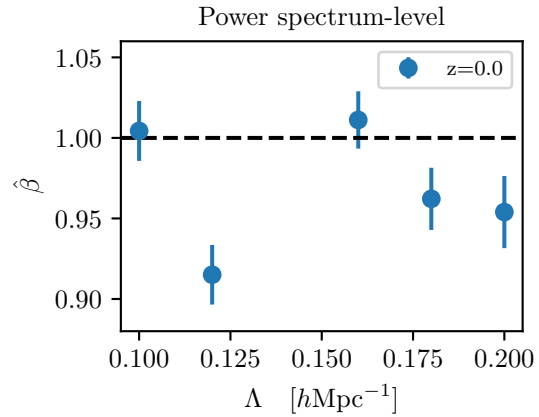
(a)  $\log_{10}(M/h^{-1}M_{\odot}) = 12.5 - 13.0$ (b)  $\log_{10}(M/h^{-1}M_{\odot}) = 13.0 - 13.5$ (c)  $\log_{10}(M/h^{-1}M_{\odot}) = 13.5 - 14.0$ (d)  $\log_{10}(M/h^{-1}M_{\odot}) = 14.0 - 14.5$ 

Figure 7.8: MAP values for  $\beta$  using the power spectrum likelihood for different  $\Lambda$ . Different panels show four different mass ranges at three different redshifts.

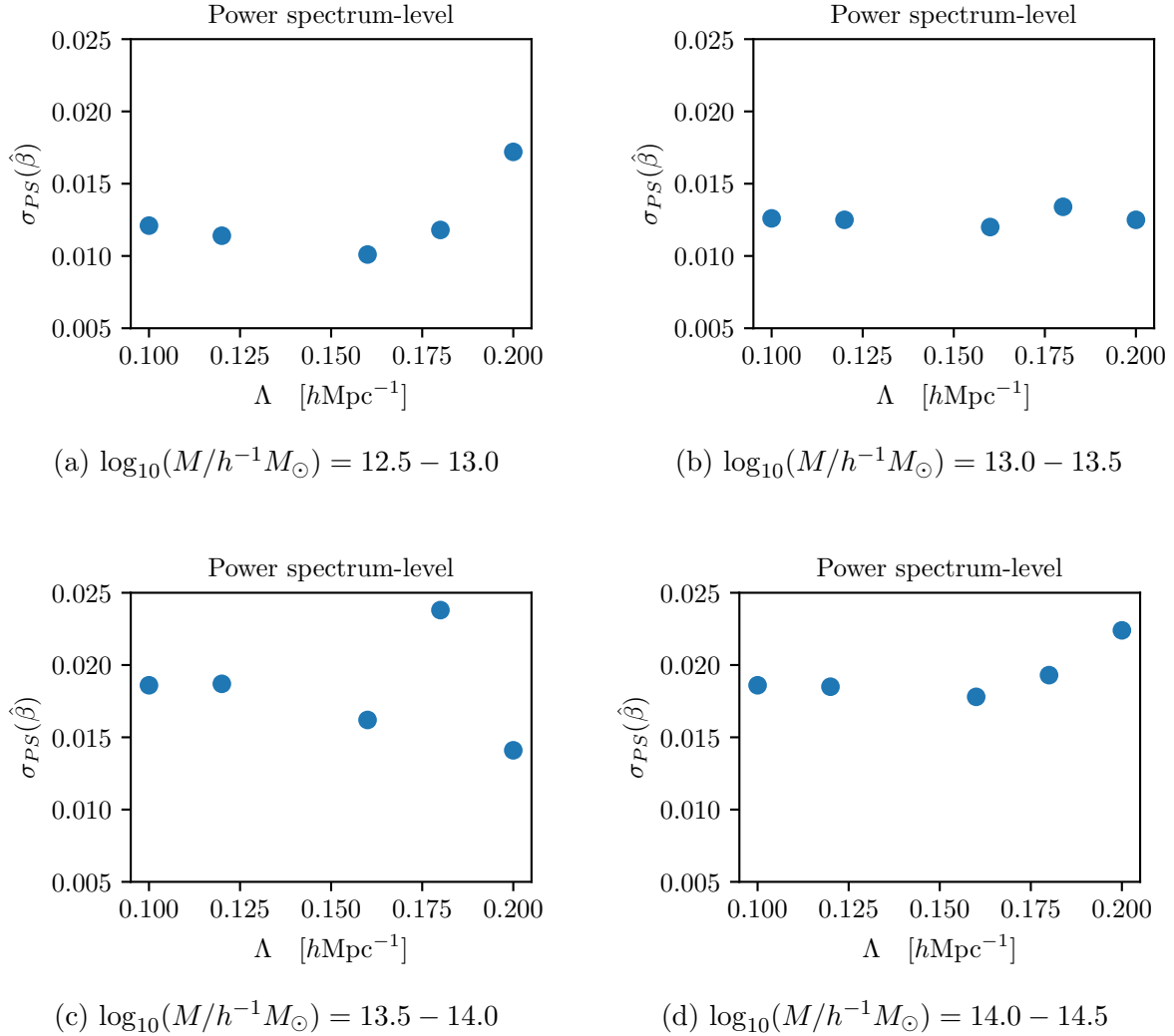


Figure 7.9:  $\sigma_{PS}(\hat{\beta})$  values found using the power spectrum likelihood for different  $\Lambda$ . Different panels show four different mass ranges at the redshift  $z = 0$ .

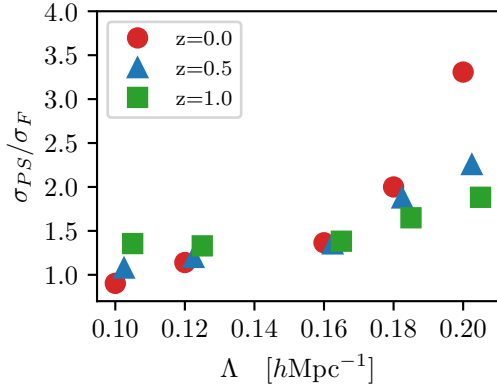
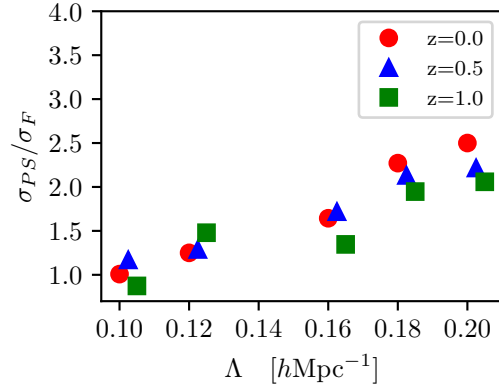
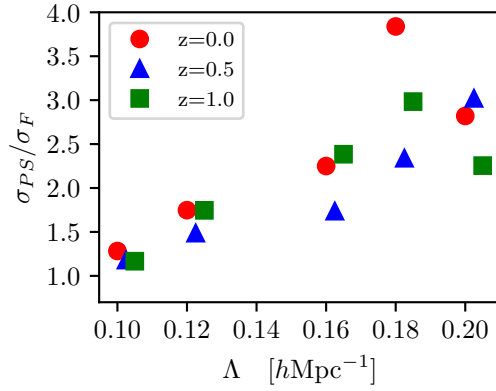
(a)  $\log_{10}(M/h^{-1}M_{\odot}) = 12.5 - 13.0$ (b)  $\log_{10}(M/h^{-1}M_{\odot}) = 13.0 - 13.5$ (c)  $\log_{10}(M/h^{-1}M_{\odot}) = 13.5 - 14.0$ 

Figure 7.10: Ratio of the uncertainty on the BAO scale inferred from the power spectrum likelihood,  $\sigma_{PS}(\hat{\beta})$ , to that from the field-level likelihood,  $\sigma_F(\hat{\beta})$ , as a function of cutoff for different redshifts. Each panel corresponds to a different halo mass range.

## 7.5 Summary and Conclusions

In this chapter we compared the inference of the BAO scale from the halo catalogs using an LPT-based forward model combined with the EFT likelihood with the standard approach which compresses the data to the power spectrum. The forward model uses a combination of 3LPT expansion for the matter field and a third-order bias expansion. Our results were expressed in the terms of the parameter  $\beta$ , defined as the ratio of the measured value of the BAO scale to its fiducial value.

The field-level inference results are summarised in Fig. 7.4 and Tab. 7.2. From these it is clear that the remaining systematic error in  $\hat{\beta}$  is at most  $\sim 2\%$  for all samples. If we ignore the most biased sample ( $\log_{10}(M/h^{-1}M_{\odot}) > 14.0$  at  $z = 0.5$  and  $z = 1.0$ ), at  $\Lambda = 0.16 h \text{ Mpc}^{-1}$ , the remaining bias in  $\beta$  is less than 1% for all remaining samples, which is remarkably low. Moreover,  $\hat{\beta}$  is statistically consistent with being unbiased for all halo samples except the highest mass one. It is also interesting to notice that the bias in  $\hat{\beta}$  is under control for all halo mass ranges, even for  $\Lambda = 0.25 h \text{ Mpc}^{-1}$ , which is close to the nonlinear scale. For the lighter halos,  $\log_{10}(M/h^{-1}M_{\odot}) < 13.5$ , this even applies to  $\Lambda = 0.3 h \text{ Mpc}^{-1}$ .

While we consider halos here, the EFT approach is equally applicable to galaxies. This is confirmed by the results of [15], who demonstrated an unbiased inference of the linear power spectrum normalization  $\sigma_8$  on fully hydrodynamical simulated galaxies.

In order to assess the performance of the field-level inference of the BAO scale, we compare it to the more traditional approach of the BAO inference from the power spectrum. For this we utilized the likelihood defined in Eq. (7.2), where the theory model for the power spectrum is based on the same forward model as in the EFT likelihood approach (in particular, the field-level likelihood was still used to find the best-fit values for the bias parameters). We modified the covariance in this likelihood to reflect the fact that we are using fixed phases, so that we can compare the two approaches on the same footing. Results found using this likelihood are shown in Fig. 7.8 and Tab. 7.3. For a fixed  $\Lambda = 0.16 h \text{ Mpc}^{-1}$ , the remaining systematic error  $\hat{\beta}$  is between 1.2% and 2.3% for those halo samples that yielded converged profile likelihoods.

Fig. 7.10 shows the relative performance of the field-level and power spectrum based likelihoods. Across all halos samples, we notice a similar trend. For smaller cutoffs, both likelihoods show similar performance. However, for  $\Lambda > 0.12 h \text{ Mpc}^{-1}$ , the field-level likelihood gives better results across all the halo masses and redshifts. For the highest cutoff value considered in both likelihoods,  $\Lambda = 0.2 h \text{ Mpc}^{-1}$ , the error on the BAO scale inferred from the power spectrum is between 2.47 – 3.3 times larger than that obtained from the field-level likelihood, depending on the halo sample. Since the field-level likelihood contains all the information that would come from the higher order correlation functions, including the precise bulk-flow field, while the information available in the likelihood from Eq. (7.2) are only those from the power spectrum, a better performance of the EFT likelihood was to be expected.

In future work we will investigate how well we can constrain the BAO from the EFT

likelihood in the cases when the initial conditions are not fixed, but sampled. This will allow for a realistic comparison of the constraining power on the BAO scale that can be obtained from the field-level inference as compared to that based on the galaxy power spectrum.

# Chapter 8

## Straightening the Ruler: Field-Level Inference of the BAO Scale with LEFTfield

*This chapter is an adaptation of [12].*

### Abstract

Current inferences of the BAO scale from galaxy clustering employ a reconstruction technique at fixed cosmology and bias parameters. Here, we present the first consistent joint Bayesian inference of the isotropic BAO scale, jointly varying the initial conditions as well as all bias coefficients, based on the EFT-based field-level forward model `LEFTfield`. We apply this analysis to mock data generated with a much higher cutoff (resolution), resulting in a significant model mismatch between mock data and the model used in the inference. We demonstrate that the remaining systematic bias in the BAO scale is below 2% for all data considered and below 1% when Eulerian bias is used for inference. Furthermore, we find that the inferred error on the BAO scale is up to 1.6 times smaller compared to that from a replication of the standard power-spectrum reconstruction approach, using the same scales as in the field-level inference, with the improvement growing towards smaller scales (higher  $k$ ). Thus, a field-level approach to BAO not only allows for a consistent inference of the BAO scale, but promises to achieve more precise measurements on the same data as well.

### 8.1 Introduction

In the previous chapter, we performed BAO scale inference on the dark matter halo samples in N-body simulations, but in the scenario of fixed initial conditions. Our analysis revealed that the error bars for the BAO scale were between 1.1 and 3.3 times smaller when using

the field-level likelihood as compared to the power spectrum without BAO reconstruction, where this range corresponds to the range of scales considered,  $\Lambda = [0.1 - 0.25] h \text{ Mpc}^{-1}$ , as well as different halo samples and redshifts.

In this chapter, we go a significant step further and use the field-level likelihood to perform a joint inference of the BAO scale and the initial conditions, which of course is necessary in the application to real data. Sampling initial conditions is challenging since the dimensionality of the parameter space is of the order of  $10^5 - 10^6$ . To deal with this challenge, we follow the lead of [61] and use the Hamiltonian Monte Carlo (HMC) [88] sampling method to sample the initial conditions and slice sampler [89] to sample the cosmological parameters. We apply this analysis to mock data generated with the `LEFTfield` code, a Lagrangian EFT-based forward model [109], which we also use for the inference. Importantly, our mock data are generated with a substantially higher cutoff than that used in the inference, as well as different bias models (with bias parameters representative of actual halo samples), so that we can test the robustness against model mis-specifications.

Apart from demonstrating the feasibility and robustness of BAO scale inference at the field level with `LEFTfield`, the second main goal of this work is to quantify the information gain relative to the standard reconstruction algorithm [50]. To this end, we adapt the reconstruction pipeline to deal with our mock data, and then perform an inference using, as closely as possible, the same cutoffs and scales as used in the field-level inference. This allows us to perform a consistent comparison of the two methods. The results of this comparison are presented in Sec. 8.4.2.

Section 6.2 provides details of the implementation within the `LEFTfield` code. Section 8.2 elaborates on the generation of mock data. Finally, in Section 8.3.2, we present the results from the joint inference of BAO along with the initial conditions, and compare to the power-spectrum analysis with and without reconstruction applied in Section 8.4.

## 8.2 Synthetic Data sets

The data sets used in this chapter were generated using the `LEFTfield` code, which we denote as Mock A and Mock B. Both data sets were generated in a box of side length  $L = 2000 h^{-1} \text{ Mpc}$  and with fiducial cosmology fixed to  $\sigma_8 = 0.85$ ,  $\Omega_m = 0.3$ ,  $\Omega_\Lambda = 0.7$ ,  $h = 0.7$  and  $n_s = 0.967$ . We emphasize that both mocks contain nonlinear information, as they were generated using second-order LPT, while the distinguishing factor between them lies in the choice of the bias model. Mock A was created using the second-order Lagrangian bias, while Mock B utilized the second-order Eulerian bias. For the bias parameters, we adopted values obtained through fixed-phase inference on realizations of halo catalogues (see for example [73]), specifically the halo mass range  $\log_{10}(M/h^{-1}M_\odot) = 13.0 - 13.5$  at redshift  $z = 0$ . In order to increase the signal to noise ratio, we used a slightly lower noise level than in the halos sample for both mocks. Ground truth  $\beta_0$  values were deliberately selected to be different from 1 to verify unbiased inference even in the case of a nontrivial rescaling of the fiducial power spectrum. Furthermore, the mocks were generated at the

Mock	Bias basis	$P_\epsilon [h^{-3} \text{Mpc}^3]$	$\beta$	$b_\delta$	$b_{\nabla^2\delta}$	$b_{\sigma\sigma}$	$b_{\text{Tr}[M^{(1)}M^{(1)}]}$	$b_{\delta^2}$	$b_{K^2}$
A	Lagrangian	553.83	0.99	1.21	0	-0.26	-0.18	-	-
B	Eulerian	915.53	0.98	1.67	-0.07	-	-	-0.19	0

Table 8.1: Values of parameters used to produce mock datasets A and B. For both mocks, we use second order LPT combined with second order bias expansion and cutoff  $\Lambda_0 = 0.3 h \text{Mpc}^{-1}$ .

cutoff  $\Lambda_0 = 0.3 h \text{Mpc}^{-1}$ , while the inference was performed at lower  $\Lambda$  values, allowing us to test the impact of model mismatch in this dimension as well. The values of all parameters used to generate these mocks are summarized in Table 8.1.

## 8.3 Field level BAO inference

### 8.3.1 Sampling method and data analysis

In this section, we provide a detailed account of how we sample from the posterior defined in Sec. 6.1. To achieve this, we employ a combination of the HMC sampler for initial conditions and the slice sampler for all other parameters.

The initial step involves selecting a prior for the initial field  $\hat{s}$ . Depending on this choice, we distinguish between two scenarios,

$$\hat{s}(\mathbf{x}) = \begin{cases} \delta_D(\hat{s} - \hat{s}_{\text{true}}), & \text{FixedIC,} \\ \mathcal{N}(0, 1), & \text{FreeIC.} \end{cases} \quad (8.1)$$

In the case when  $\hat{s}$  is fixed to ground truth, we are talking about FixedIC case. Alternatively, the case when the Gaussian prior for  $\hat{s}$  is chosen, we denote as FreeIC. FixedIC case has been extensively studied in our previous work [11], while here we are focused on the FreeIC case and use the FixedIC case only as a consistency check.

The FreeIC case is challenging in particular due to the dimensionality of the parameter space of  $\hat{s}$  which is of the order of  $10^6$ . To perform the sampling of such a large parameter space, we use the HMC sampler which is well suited for sampling in large dimensions. While the execution time in standard MCMC techniques typically scales linearly with the dimension of the problem  $N_{\text{dim}}$ , in the case of the HMC it scales as  $N_{\text{dim}}^{1/4}$  [88]. Because of the way HMC generates new proposals, it requires a forward model which is differentiable with respect to the initial conditions. Fortunately, our forward model is differentiable, and the structure of the LEFTfield code allows us to find its analytical derivative by performing successive applications of the chain rule.

Apart from the initial conditions, we also sample  $\beta, \sigma_\epsilon$  and  $\sigma_{\epsilon,2}$ . The priors used for

these parameters are

$$\begin{aligned}\mathcal{P}(\beta) &= \mathcal{U}(0.8, 1.2), \\ \mathcal{P}(\sigma_\epsilon) &= \mathcal{U}(0.05, 100), \\ \mathcal{P}(\sigma_{\epsilon,2}) &= \mathcal{U}(-10^5, 10^5),\end{aligned}\tag{8.2}$$

where  $\mathcal{U}$  denotes the uniform distribution.

When employing the likelihood marginalized over bias parameters, one MCMC chain used Gaussian priors for bias parameters. More specifically, the priors used were  $\mathcal{N}(0.01, 5)$  for  $b_\delta$  and  $\mathcal{N}(0, 5)$  for the other bias parameters. In addition to this, we operated two other chains that employed uniform priors:  $\mathcal{U}(0.01, 10)$  for  $b_\delta$ , and  $\mathcal{U}(-30, 30)$  for the remaining bias parameters. However, the bias coefficients are well constrained by the data, and the posteriors are likelihood-dominated for both chains. Hence, despite the different priors, all chains are found to yield consistent posteriors in  $\beta, \sigma_\epsilon$  and  $\sigma_{\epsilon,2}$ . Therefore, we aggregated the results from all three chains in the analysis. For comparison, we have also performed inferences using a likelihood that was not marginalized over bias parameters; the results of this inference are shown in App. B, and provide evidence for the above statement.

To sample cosmological parameters, we employ the univariate slice sampling technique. This involves drawing samples from the one-dimensional probability density function associated with these parameters, considering the present state of the initial conditions,  $\hat{s}$ . For each data set, we run a set of three chains: one starting from true initial conditions and two starting from random initial conditions. We continue running these chains until we achieve at least 100 effective samples of the  $\beta$  parameter.

### 8.3.2 Field-level results

In this section, we present inference results obtained using the marginalized EFT likelihood for both Mock A and Mock B.

Mock A was generated using the second-order Lagrangian bias expansion which we also use for the inference. In Fig. 8.1, we present a trace plot for the parameter  $\beta$  corresponding to a specific value of  $\Lambda = 0.2 h \text{ Mpc}^{-1}$ . The figure shows the trajectories of all three Markov chains utilized in our analysis. Despite starting from different  $\beta$  values, the chains exhibit rapid convergence towards a consistent value of  $\beta$ , indicating robustness in parameter estimation across varied starting points. It is also important to note that one of the chains started from the true initial conditions  $\hat{s}_{\text{true}}$  while the other two started from random  $\hat{s}$ . Fig. 8.2 depicts the normalized auto-correlation function for  $\beta$  (for  $\Lambda = 0.2 h \text{ Mpc}^{-1}$ ), for one of the chains. We find the correlation length  $\tau(\beta)$  to be quite short, substantially shorter than that of  $\sigma_8$  in the field-level inference chains shown in [21, 90]. This is a major computational advantage which also allows us to push to smaller scales than used there. We determine the effective number of samples by dividing the absolute length of the chain by the estimated correlation length.

Our main findings for Mock A are summarized in Fig. 8.3. In the left panel, we show the remaining systematic bias in the  $\beta$  value. For the lower cutoffs,  $\Lambda = 0.15 h \text{ Mpc}^{-1}$  and  $\Lambda = 0.18 h \text{ Mpc}^{-1}$ , the bias is below 1%, however in the case of  $\Lambda = 0.2 h \text{ Mpc}^{-1}$  the systematic

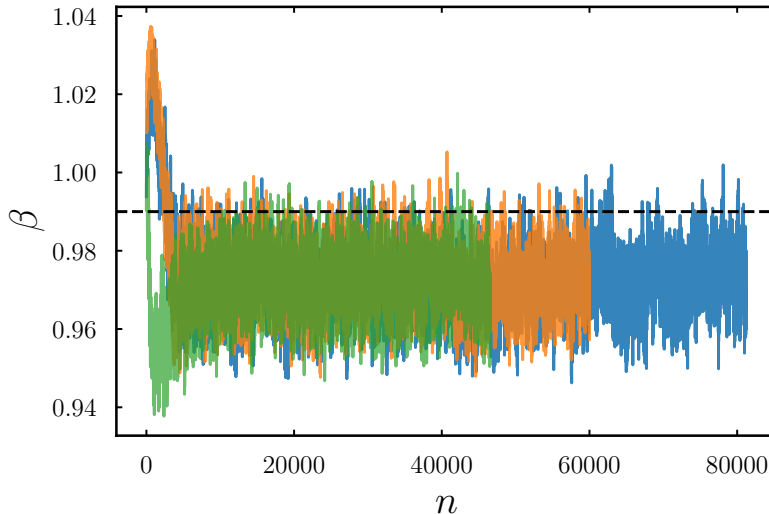


Figure 8.1: Trace plot of parameter  $\beta$  for  $\Lambda = 0.2 h \text{ Mpc}^{-1}$  for three independent MCMC chains, where  $n$  denotes the sample index. The chain shown in green started from the true initial conditions  $\hat{s}_{\text{true}}$  while the other two chains started from random initial conditions  $\hat{s}$ . Each chain started from a different initial  $\beta$  value, with all quickly converging to the same value. Dashed black line indicates the ground truth value  $\beta_0$ .

offset is around 1.8%. This is most likely due to our choice to employ a second-order bias expansion for the inference. We generated the mocks at a higher cutoff, and thus they require more bias terms to describe at the lower cutoff used for the inference.

The right panel of Fig. 8.3 displays the 68% confidence-level error bars for  $\beta$ , denoted as  $\sigma_{\text{F}}(\beta)$ , obtained through the EFT likelihood across varying  $\Lambda$  values. For the lowest cutoff,  $\sigma_{\text{F}}(\beta)$  slightly exceeds 1%, whereas for the two higher cutoffs, it reduces to 0.71% and 0.66%, respectively. The reduction in error bar size with increasing cutoff was anticipated, as a larger  $\Lambda$  permits the inclusion of more modes in both the forward model and the likelihood, thereby providing additional information. We can also compare the behavior of  $\sigma_{\text{F}}(\beta)$  as a function of  $\Lambda$  with the ideal expectation from mode counting,  $\sigma_{\text{F}}(\beta) \propto N_{\text{mode}}^{-1/2}(\Lambda)$ , finding very rough agreement. More precisely, the error bar  $\sigma_{\text{F}}(\beta)$  improves more rapidly than the mode scaling between  $\Lambda = 0.15 h \text{ Mpc}^{-1}$  and  $\Lambda = 0.18 h \text{ Mpc}^{-1}$ , while between  $\Lambda = 0.18 h \text{ Mpc}^{-1}$  and  $\Lambda = 0.2 h \text{ Mpc}^{-1}$ , it shrinks at a lower rate than estimated from mode counting. Note however that the simple mode counting ignores the varying sensitivity to a change in  $\beta$  of the linear power spectrum as a function of  $k$ .

Turning our attention to Mock B, this data set is generated using the second-order Eulerian bias and sampled with both the second-order Eulerian and second-order Lagrangian biases. The left panel of Fig. 8.4 shows the inferred  $\beta$  for both Eulerian and Lagrangian bias cases. In the instance of Eulerian bias, we observe that the residual systematic bias remains below 1% across all considered cutoffs. Additionally, the ground truth value of  $\beta$  is consistently recovered within  $1\sigma$ . Conversely, when using the Lagrangian bias model for

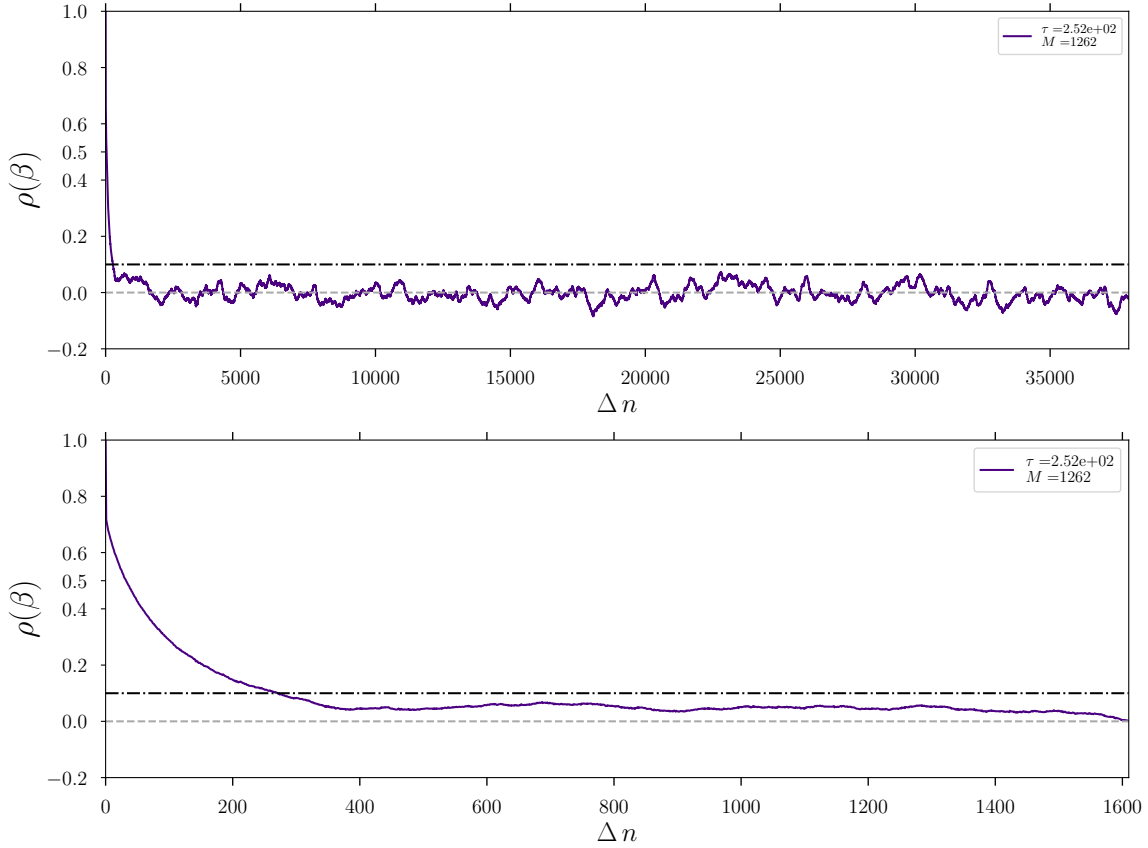


Figure 8.2: The normalized auto-correlation function for parameter  $\beta$  inferred at  $\Lambda = 0.2 h \text{Mpc}^{-1}$ . In the figure we also display the correlation length value  $\tau$  together with the maximum separation  $M$  between the samples considered, both of which are defined in App. B. The correlation length of  $\beta$  is estimated to be  $\tau \simeq 244$  samples. In the lower panel, we zoom into the first 1800 samples of the chain.

inference, a slightly higher systematic bias is evident. Specifically, for  $\Lambda = 0.15 h \text{Mpc}^{-1}$  and  $0.18 h \text{Mpc}^{-1}$ , this bias hovers around 1%, while for  $\Lambda = 0.2 h \text{Mpc}^{-1}$ , it increases somewhat to 1.7%. This is consistent with what we found for Mock A, and would likely be solved by going to a higher order in bias in the inference.

In the right panel of Fig. 8.4, we show the inferred 68% CL error bar  $\sigma_{\text{F}}(\beta)$  for the Mock B at the different cutoffs. We find that in the case of both bias models the size of the error bar is shrinking with increasing  $\Lambda$ . This trend aligns with our expectations, as a larger  $\Lambda$  implies the inclusion of more modes in both the forward model and the likelihood.

Comparing the error bar size,  $\sigma_{\text{F}}(\beta)$ , between the Eulerian and Lagrangian models shows that the error bar is smaller in the case of the Lagrangian bias model. This difference is likely attributable to the construction of bias operators in these models. In the Eulerian bias model, bias operators are constructed using the filtered matter field,  $\delta_{\Lambda}$ . This second filter (in addition to the one applied to the initial conditions) removes some mode-coupling

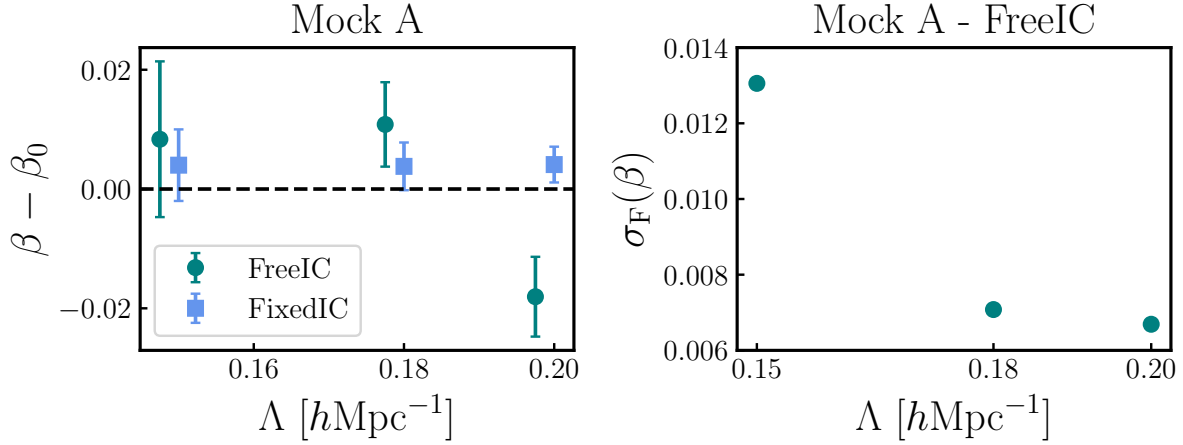


Figure 8.3: Inference results for the Mock A. Left panel shows inferred BAO scale relative to ground truth obtained using Lagrangian bias for sampling. FreeIC are represented using circle marker and FixedIC using a square. On the right we show the 68% CL error bar on the BAO scale,  $\sigma_F(\beta)$ , as a function of cutoff  $\Lambda$ .

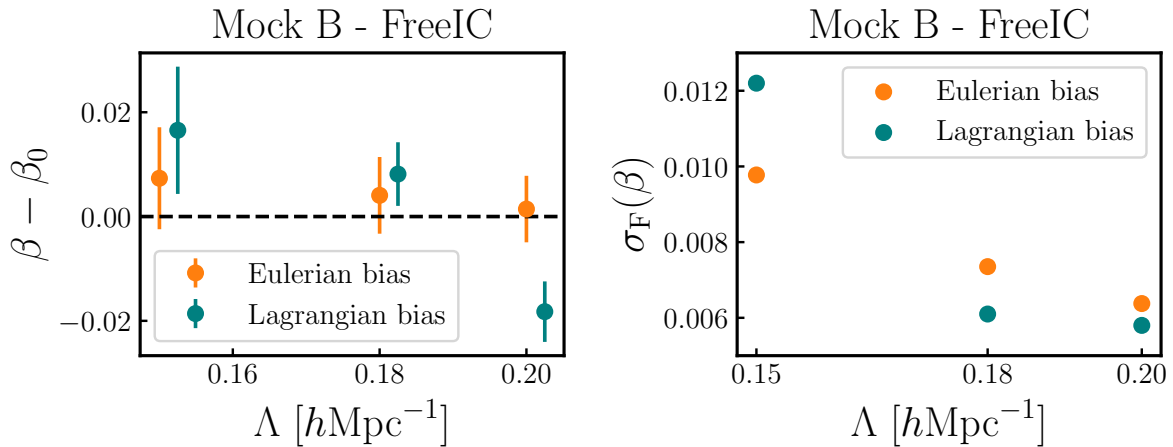


Figure 8.4: Inference results for Mock B. The left panel displays the inferred BAO scale relative to the ground truth, where the BAO scale is sampled alongside the initial conditions. The Lagrangian bias points, computed for the same values of  $\Lambda$ , have been slightly displaced horizontally for better visibility. On the right, we show the 68% CL error bar,  $\sigma_F(\beta)$ , as a function of the cutoff  $\Lambda$ . The results obtained using the Lagrangian bias are depicted in blue, while those obtained using Eulerian bias are shown in orange.

contributions that are under control and kept in the Lagrangian bias model, which only filters the initial conditions (both bias models of course use the same likelihood filter). The downside of the Lagrangian approach is the higher computational cost due to the

additional density assignments needed.

In Fig. 8.5, we show posteriors of parameters sampled on the Mock B dataset using  $\Lambda = 0.18 h \text{ Mpc}^{-1}$ . The two panels correspond to the Eulerian and Lagrangian biases, respectively. Mock B was generated at  $\Lambda_0 = 0.3 h \text{ Mpc}^{-1}$  with  $\sigma_\epsilon = 0.9$ . From Eq. (6.11), we find that this will correspond  $\sigma_\epsilon \approx 0.41$  at  $\Lambda = 0.18 h \text{ Mpc}^{-1}$ . We see that the inferred value of  $\sigma_\epsilon$  is indeed consistent with the expected value within errors. However, we notice that  $\sigma_{\epsilon,2}$  is now larger than zero. This elevation in noise level is due to the fact that inference is performed at  $\Lambda < \Lambda_0$ . Since the model is nonlinear, the modes between  $\Lambda$  and  $\Lambda_0$  which are integrated out lead to additional effective noise contributions, as shown explicitly in [71] and at the level of renormalization-group equations in [108].

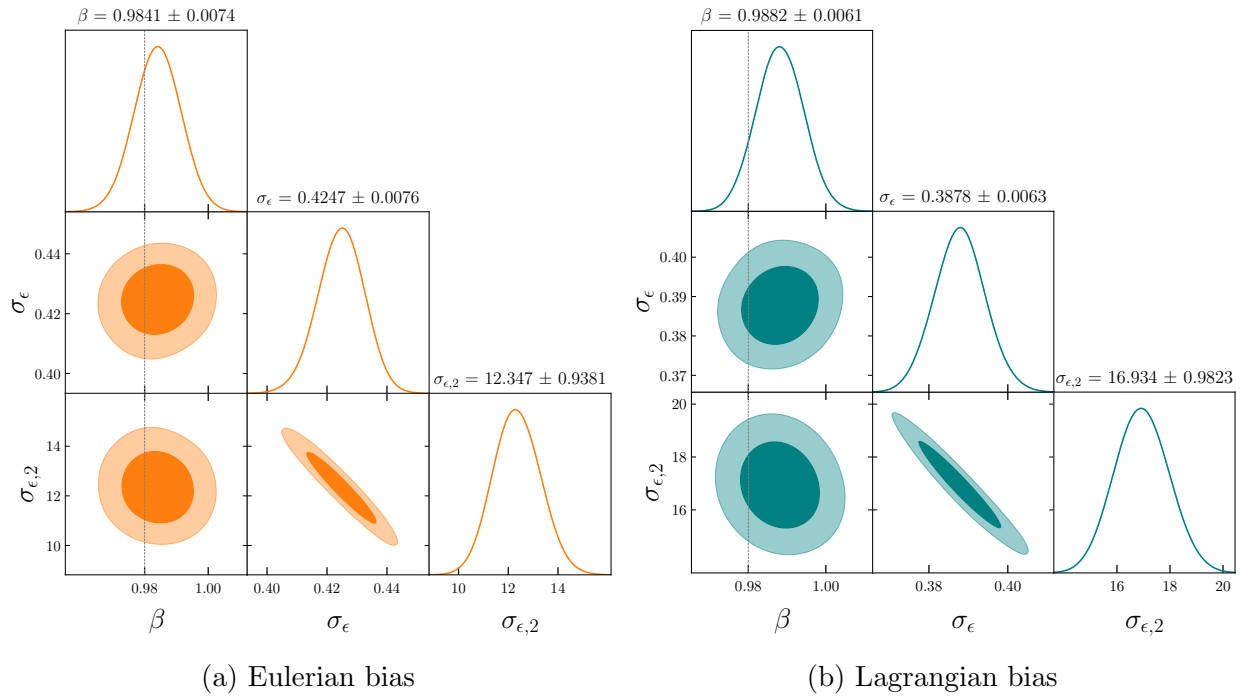


Figure 8.5: Posterior of parameters for the FreeIC inference in the case of Mock B. Left panel (a) represents the Eulerian bias model while the right panel (b) represents the Lagrangian bias. The dotted gray line indicates the ground truth value  $\beta_0$  in each case. The inference was performed at  $\Lambda = 0.18 h \text{ Mpc}^{-1}$  in both cases.

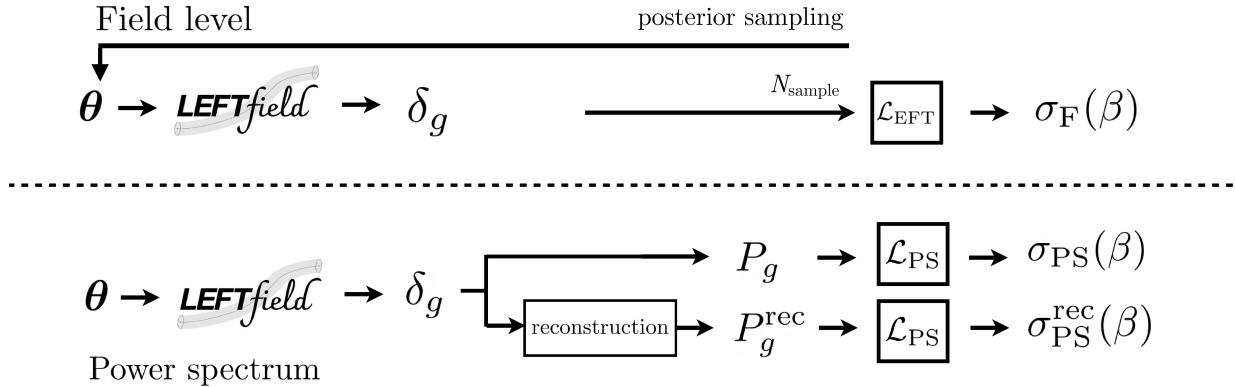


Figure 8.6: Diagram of two methods of BAO inference; field level inference (top) and power spectrum-based inference with and without reconstruction (bottom). The reconstruction step includes the generation of a discrete tracer catalog from  $\delta_g$ , as described in the text

## 8.4 Comparing the field-level results to the reconstruction approach

### 8.4.1 BAO Reconstruction Procedure

We now describe how we implement a BAO reconstruction pipeline on our mock data. The initial step involves generating mock datasets using the `LEFTfield` code. The parameters chosen for the creation of these datasets are aligned with those employed in the field-level inference (as described below) to maintain consistency across the two analyses. This includes the use of the same bias parameters, noise levels, and the value for  $\beta$ . A flowchart summarizing both analyses is shown in Fig. 8.6.

We adopt the standard reconstruction procedure, which is based on the algorithm introduced by [50] and summarized in Chapter 5.2. However, before this can be applied, we need to convert the density distribution on a grid (of size  $N^{\Lambda_0} = 192^3$ , where  $\Lambda_0 = 0.3 h \text{Mpc}^{-1}$  is the cutoff value used to generate the mock) generated by the `LEFTfield` code to a catalog of discrete “tracer” positions. This is done by first replacing the Gaussian likelihood used in the EFT likelihood with a Poisson process, which generates a discrete tracer count  $N_i$  in each voxel  $i$ . For the average tracer number density  $\bar{n}_g$ , we adopt the value of  $1/P_\epsilon$  used for the mocks employed in the field-level analysis. We then assign random positions to each of the  $N_i$  tracers within the voxel  $i$ .

Once the mock catalog is obtained, we proceed with the reconstruction. To ensure a fair comparison with the field level approach and guarantee that both methods have access to the same  $k$ -modes, we carefully select the smoothing scale and grid sizes. The choice of the smoothing scale is particularly important, given that the field-level approach employs a sharp- $k$  filter, while standard reconstruction involves a Gaussian filter. We choose the Gaussian smoothing scale  $R = \frac{1}{\Lambda}$ . We consider this to be a conservative choice

for the comparison, as it allows for a significant contribution from modes with  $k > \Lambda$  in the standard reconstruction approach, while these modes are excluded from the field-level analysis.

The reconstruction proceeds as follows.

1. Smooth the density field  $\delta_g$  using a Gaussian filter  $S(k, R)$  with a smoothing scale  $R$ :  $\delta_g(\mathbf{k}) \rightarrow S(k, R)\delta_g(\mathbf{k})$ .
2. Using the smoothed density field, we find the estimated displacement  $\boldsymbol{\psi}$ , where

$$\boldsymbol{\psi}(\mathbf{k}) \equiv -i \frac{\mathbf{k}}{k^2} S(k, R) \frac{\delta_g(\mathbf{k})}{b_\delta}. \quad (8.3)$$

3. We interpolate  $\boldsymbol{\psi}$  to find its value at the position of each tracer and use it to move the tracers.
4. Once all the tracers have been shifted, we use the nearest-grid-point (NGP) assignment scheme and a grid of size  $N^{\Lambda_0}$  to obtain the “displaced” density field  $\delta_d$ . Notice that this operation removes a large fraction of the large-scale perturbations in  $\delta_g$ .
5. We generate a spatially uniform grid of particles and shift them by  $\boldsymbol{\psi}$  to create the “shifted” field  $\delta_s$ . The assignment scheme used to find  $\delta_s$  is again NGP, and the grid size is  $N^{\Lambda_0}$ .
6. The reconstructed density field is obtained as  $\delta_g^{\text{rec}} = \delta_d - \delta_s$ , where the field  $-\delta_s$  re-instates the large-scale perturbations removed from  $\delta_d$ .
7. Next, we resize the reconstructed field to a grid of size  $N_g^\Lambda$  to make sure we keep only the modes below the cutoff.
8. Finally, we measure the power spectrum of the reconstructed field,  $P_g^{\text{rec}}$ , with  $k_{\text{max}} = \Lambda$ .

As an illustration, the left panel of Fig. 8.7 displays the oscillatory part of the power spectrum averaged over 500 Mock A-like realizations, for both pre- and post-reconstruction cases. Post-reconstruction, the wiggles become significantly more pronounced.

Finally, to obtain the BAO scale parameter  $\beta$  and its uncertainty, we use a maximum-likelihood approach, where all parameters apart from  $\beta$  are fixed to their ground truths. For a given value of  $\Lambda$ , we calculate the power spectrum likelihood  $\mathcal{L}_{\text{PS}}$  for a set of  $\{\beta_i\}$  values, where

$$-2 \log \mathcal{L}_{\text{PS}}(\beta) = \frac{(P_{\text{data}}(k) - P_{\text{theory}}(k, \beta))^2}{\text{Cov}[P_{\text{data}}(k)]} + \text{const.} \quad (8.4)$$

Here,  $P_{\text{data}}(k)$  represents the power spectrum of the reconstructed mock data from which we aim to infer the BAO scale, and  $P_{\text{theory}}(k, \beta)$  is the theoretical prediction for the reconstructed power spectrum for different  $\beta$  values. We find the latter by averaging over 500

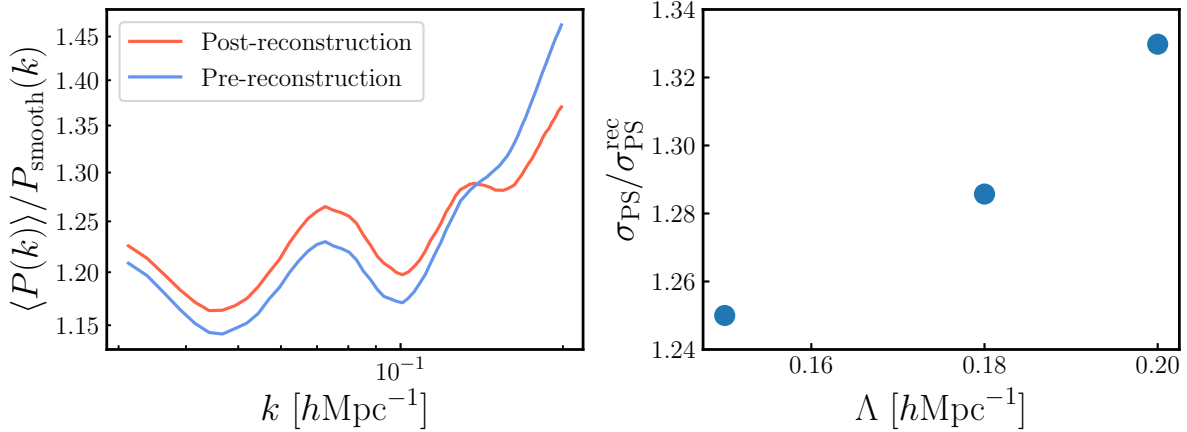


Figure 8.7: The left panel shows the oscillatory part of the power spectrum averaged over 500 Mock A-like realizations. We show this for both the pre- and post-reconstructed power spectrum (for  $\Lambda = 0.2 h \text{Mpc}^{-1}$ ). We see that following the reconstruction, the wiggles on smaller scales become more pronounced. The right panel shows the inferred error bar  $\sigma_{\text{PS}}(\beta)$  on the BAO scale using pre- and post-reconstruction power spectrum. The gain in BAO scale precision due to reconstruction increases as  $\Lambda$  increases.

samples, each sharing the same cosmological, bias, and noise parameters at fixed  $\beta$ , but featuring independent realizations of the initial conditions. We use linear binning to find the power spectrum. The forward model, specified by  $\Lambda_0$ , as well as all bias terms and  $\sigma_\epsilon$  are fixed at the values used for generating the mock. It is worth noting that  $P_{\text{theory}}(k, \beta)$  already incorporates the stochastic contributions  $P_\epsilon$ . We use the linear covariance

$$\text{Cov}[P_{\text{data}}(k)] = 2 \frac{[P_{\text{theory}}(k, \beta_0)]^2}{m_k}, \quad (8.5)$$

where  $m_k$  is the number of modes inside a bin. Since the covariance is independent of  $\beta$ , the normalization constant in Eq. (8.4) is irrelevant.

We then fit a parabola to the set of  $\{\beta_i, -2 \ln \mathcal{L}_{\text{PS}}(\beta_i)\}$ . The maximum-likelihood value of  $\beta$ , denoted as  $\hat{\beta}$ , is located at the minimum of this parabola. The error bar,  $\sigma_{\text{PS}}(\beta)$ , can be estimated by finding the point at which  $-2 \log \mathcal{L}_{\text{PS}}$  increases by 1. Note that we apply this inference procedure using  $\mathcal{L}_{\text{PS}}$  both for the pre- and post-reconstruction power-spectra, as depicted in Fig. 8.6. The improvement in BAO scale determination after reconstruction is demonstrated in the right panel Fig. 8.7. Notice that the relative improvement grows with with increasing  $\Lambda$ , which is expected since the sharpening of the BAO by reconstruction is more pronounced at higher  $k$ .

Compared to the field-level approach, which jointly infers all bias and stochastic parameters, this analysis strongly favors the standard power-spectrum-based method. By conducting the reconstruction at the same cutoff used to generate the mock, we give access to the complete information about the mock, and avoid the model mismatches that the

field-level analysis had to overcome. Additionally, we fix the values of the bias parameters, whereas in practice, jointly inferring the values of the bias parameters would introduce further uncertainties into the inference process and enlarge the error bars. These issues are clearly worth revisiting in the future.

### 8.4.2 Inference results and comparison with the field level

In this section, we compare the results of the power spectrum analysis (before and after reconstruction) with the field-level inference presented in the previous section.

We begin with Mock A, presenting in Fig. 8.8 the ratio of error bars on  $\hat{\beta}$  derived from the two power-spectrum-based analyses,  $\sigma_{\text{PS}}$ , to those obtained at the field level,  $\sigma_{\text{F}}$ . Compared to the field level, the pre-reconstruction power spectrum yields an error bar between 1.15 and 2 times larger. As expected, this difference between  $\sigma_{\text{PS}}$  and  $\sigma_{\text{F}}$  decreases once we perform reconstruction, where we find  $\sigma_{\text{PS}}$  to be at most 1.5 times larger than  $\sigma_{\text{F}}$ . Note that the improvement of field level over power spectrum generally increases with the cutoff. There are several possible explanations for this, which we turn to in the discussion Sec. 8.5.

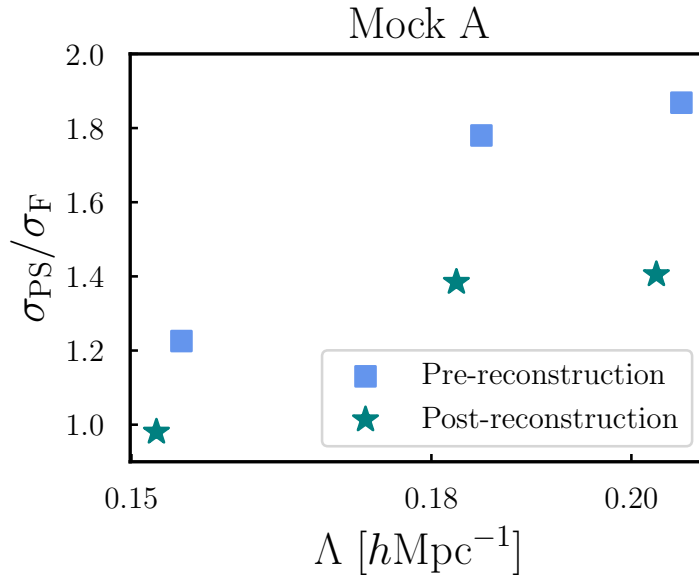


Figure 8.8: Inferred error bar  $\sigma_{\text{PS}}(\beta)$  on the BAO scale using pre- and post-reconstruction power spectrum, relative to that in the field-level inference  $\sigma_{\text{F}}$ , in the case of Mock A. This mock was generated (and sampled, in case of field-level inference) using Lagrangian bias. Pre-reconstruction results are depicted using squares, whereas post-reconstruction results are represented by stars. It is evident that, even comparing to power spectrum after BAO reconstruction, the field-level BAO scale inference is more precise, by up to a factor of 1.4, corresponding to a  $\sim 2$  times larger survey volume.

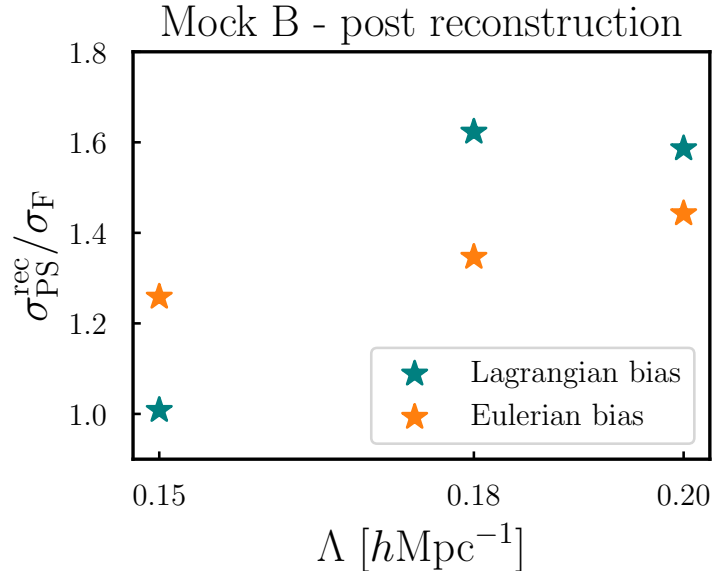


Figure 8.9: Inferred error bar  $\sigma_{\text{PS}}(\beta)$  on the BAO scale from the post-reconstruction power spectrum, relative to that in the field-level inference  $\sigma_{\text{F}}$ , in the case of Mock B. Blue points indicate the scenario where the Lagrangian bias is used in the field level inference, while orange points correspond to the Eulerian case (the reconstruction results are the same in both cases). The field-level error bar is consistently smaller, regardless of which bias basis is used in the field-level inference.

We perform a similar analysis in the case of the Mock B, the results of which are summarized in Fig. 8.9. In the plot, the orange points represent the comparison of the post-reconstruction power spectrum variance  $\sigma_{\text{PS}}$  to the case when we use Eulerian bias expansion in the field level. Blue points correspond to Lagrangian bias expansion being used for the field level. We find that results here are consistent with the ones in the case of Mock A:  $\sigma_{\text{PS}}$  (after reconstruction) is between 1.1 and 1.6 times larger than  $\sigma_{\text{F}}$ , with the improvement generally increasing toward higher  $\Lambda$ .

## 8.5 Discussion and Conclusions

In this chapter, we have presented the outcome of field-level BAO scale inferences, which jointly infer the BAO scale together with the initial conditions, bias and stochastic parameters via the `LEFTfield` code, applied to mock data in the rest frame (without redshift-space distortions). The mock datasets were created using bias parameters taken from a fixed initial condition (FixedIC) analysis on halo catalogues, and at a substantially higher cutoff (or resolution) than those used in the inference. By introducing model misspecification in this way, we attempt to make our mocks as realistic as possible. The primary distinction between the two sets of mock data is in the bias expansion model employed for their gen-

eration: Mock A was produced using the second-order Lagrangian bias, whereas Mock B used the second-order Eulerian bias.

For Mock A, the analysis was done only using the second-order Lagrangian bias expansion in the inference. It showed that the systematic bias in  $\beta$  stays below 1% and is effectively negligible for all  $\Lambda$  values, except for the highest cutoff, where it increases to about 1.8%. We plan to investigate this increase in systematic bias in  $\beta$  in the future by going to the third order in the bias expansion.

For the Eulerian-bias Mock B, our analysis included both second-order Lagrangian and Eulerian biases. For the Eulerian bias, we find that the remaining systematic bias is consistent with zero and decreases as  $\Lambda$  increases. In the case of Lagrangian bias expansion, the remaining systematic bias is slightly higher. Again, it is possible that the residual systematic shift in the Lagrangian analysis decreases once we go to a higher order in bias expansion. Furthermore, we find that the error bar in the case of the Lagrangian analysis is lower than in the case of Eulerian analysis. This is likely connected to the approaches used for constructing bias operators in these models. For the Eulerian bias model, the construction of bias operators involves an additional filtering of the matter field, beyond the initial condition filtering. This extra filtering step results in the omission of some mode-coupling contributions, which are preserved in the Lagrangian bias model. The latter only applies filtering to the initial conditions. Note that both models utilize the same likelihood filter.

The standard approach to BAO inference is based on applying a reconstruction procedure to the tracer catalog, and then measuring the BAO scale in the post-reconstruction power spectrum. In Sec. 8.4, we detailed the application of this reconstruction algorithm to our mock data. Throughout the reconstruction process, we employed the same  $\Lambda_0$ , and fixed the bias parameters to the values that were used to generate the mock datasets, thereby giving a significant benefit to the reconstruction-based analysis pipeline. Figures 8.8 and 8.9 summarize the comparison between the error bars obtained from the field level analysis,  $\sigma_F$ , and those derived using the power spectrum,  $\sigma_{PS}$ . These figures illustrate that, depending on the mock and the value of  $\Lambda$ ,  $\sigma_F$  is smaller than  $\sigma_{PS}$  by up to a factor of two (pre-reconstruction), or between 1.4 and 1.6 (post-reconstruction), the latter corresponding to an effective doubling of the survey volume. Additionally, we observe that the improvement over the power spectrum analysis increases as more modes are included with increasing  $\Lambda$ .

These results are clearly very encouraging for the field-level approach. However, one might naturally ask two questions about these findings: first, where does the additional information come from? As argued in [112], the field-level approach extracts the BAO feature not only in the power spectrum, but also in higher  $n$ -point functions of the tracer, such as the bispectrum, as it does not rely on any compression of the data. In addition, our use of a 2LPT forward model means that the change of the local BAO scale in the presence of large-scale density perturbations (due to the different local expansion in the separate-universe picture) is consistently captured. On the other hand, the Zeldovich approximation used in Eq. (8.3) does not describe this effect correctly [124]. Both of these effects are expected to become more significant as smaller scales are included in the analysis, which

could explain the increasing improvement that we find toward smaller scales (higher  $\Lambda$ ).

It is worth noting that the maximum wavenumbers included in our analysis are somewhat lower than those chosen in current BAO reconstruction analyses. Specifically, these choose a smoothing kernel in the displacement construction on similar scales as the one used here, but then measure the post-reconstruction power spectrum to higher  $k \sim 0.3 - 0.5 h \text{ Mpc}^{-1}$ . This approach assumes that the BAO are still well described by the perturbative model on scales where perturbation theory no longer applies, an assumption which needs to be carefully validated. On the other hand, the field-level approach by construction requires that the model describe all aspects of the data up to the maximum scale included, which precludes us from pushing this approach beyond perturbative scales.

The second natural question is whether these results apply to actual nonlinear tracers. Thus, our next step will be to transition from mock data to dark matter halos in full N-body simulations, and perform a similar comparison there. We are also advancing our redshift-space modeling [130], which will enable an anisotropic BAO scale inference in terms of line-of-sight and perpendicular components. Moreover, we plan to jointly infer the BAO scale while varying cosmological parameters governing the growth, such as  $\sigma_8$  and the growth rate  $f$ .

Finally, the field-level forward model also enables a consistent Bayesian inference of the BAO scale using the BAO reconstruction technique, by way of simulation-based inference (SBI) [137], allowing us to consistently marginalize over bias, noise and cosmological parameters. We also plan to explore this direction in the near future.



# Chapter 9

## Summary and Outlook

In this thesis, we have analyzed the application of field-level inference to BAO scale estimation. The main results are presented in Chapter 7 and Chapter 8.

In Chapter 7, we applied this analysis to rest frame halo catalogs and we kept the initial conditions fixed to the ground truth. The forward model we used was a combination of third-order LPT with the third-order Lagrangian bias expansion. We looked into the remaining systematic bias in the BAO scale and summarised the main findings in Fig. 7.4 and Tab. 7.2. We found that most of the samples have the remaining systematic bias below 1%. Only the most biased sample, with the most massive halos, had a remaining systematic bias up to 2%. We compared our field-level analysis to standard power spectrum-based analysis, but without BAO reconstruction. We have found that the field level error bar is between 1.1 and 3.3 times smaller than that of the power spectrum, depending on the sample considered.

In Chapter 8, we conducted a joint field-level inference of the BAO scale alongside the initial conditions. For this analysis, we used mock data generated with the `LEFTfield` code. To make the mocks more realistic, we produced them at  $\Lambda$  values significantly higher than those used in the inference and incorporated bias coefficients obtained from the FixedIC inference on halo catalogs. Our results demonstrate that this type of analysis is not only feasible but also exhibits very low remaining systematic bias. Focusing on the results obtained with the Eulerian bias model, we found that the remaining bias is consistently below 1% and effectively zero in all cases. For the Lagrangian bias model, the bias is slightly larger, reaching up to 1.8% at  $\Lambda = 0.2$ . Comparing these findings to the standard BAO reconstruction applied to the same mock data, we observed that the field-level inference yields error bars 1.4 to 1.6 times smaller than those from the reconstruction-based analysis.

In the near future, we aim to investigate the source of additional information about the BAO in field-level analysis. To address this, we plan to compare the standard Zel'dovich approximation (1LPT) with the 2LPT analysis on the same mock data. If the error bars on the BAO scale are larger with the 1LPT model compared to the 2LPT model, it would suggest that the information gain observed in [12] is attributable to the use of 2LPT. Conversely, if the error bars are similar, the additional information likely originates from higher-order n-point functions.

We also plan to apply the BAO analysis to rest-frame halo catalogs and compare these results with our existing findings. Preliminary work in this area indicates that the field-level BAO inference is consistent with our results from mock data.

Let us also note that the computational effort required for full field-level inference, including BAO scale inference alongside other cosmological parameters, is expected to be manageable. This conclusion is based on the short correlation length for the BAO, as demonstrated in Section 8.

In the long term, our goal is to apply this analysis to observed data. Two major steps are required to achieve this. Firstly, we need to integrate the anisotropic BAO scale into our analysis. To accomplish this, incorporating redshift-space distortions (RSD) into our model is essential. Fortunately, substantial progress has already been made on RSD within our group [130], which should make this step relatively straightforward.

The second step involves incorporating masks into our code. This is expected to be more challenging, as it requires masking small regions of the sky in a manner consistent with the Effective Field Theory of Large Scale Structure (EFTofLSS).

The general methodology combines BAO reconstruction with full-shape galaxy n-point functions. As demonstrated in [102], applying this technique to the power spectrum enhances cosmological constraints. However, challenges arise in accurately modeling the covariance and developing a theoretical model for the reconstructed power spectrum. This is where the `LEFTfield` forward model, in conjunction with Simulation-Based Inference (SBI), becomes particularly advantageous. The SBI approach eliminates the need for explicit covariance modeling, greatly simplifying the process. However, the primary challenge with SBI is the need for a sufficient number of simulations to effectively train the model. `LEFTfield` addresses this by providing a fast and reliable method for generating the required simulations. By combining SBI and `LEFTfield`, we can analyze both pre- and post-reconstructed spectra on galaxy density fields. Extending the analysis beyond the power spectrum to include the bispectrum and trispectrum within this framework is much simpler than using more traditional n-point function-based methods. This combination of SBI and `LEFTfield` has already been applied to  $\sigma_8$  [90] so extending it to BAO scale inference should be straight forward.

# Appendix A

## Power spectrum covariance for fixed phases

In this section we derive the power spectrum covariance in the case where the initial phases are fixed. Inside a thin shell bin of magnitude  $k$ , which we keep fixed throughout, the prediction for the halo power spectrum can be written as

$$P_h(k) = \frac{1}{m_k} \sum_{\mathbf{q}} |\delta_{\text{det}}(\mathbf{q}) + \varepsilon(\mathbf{q})|^2, \quad (\text{A.1})$$

with the sum running over all the modes  $\mathbf{q}$  inside the bin of magnitude  $k$ .  $\delta_{\text{det}}(\mathbf{q}) \equiv \delta_{\text{det}}(\mathbf{q}|\delta_{\text{in}}, \{b_O\})$  is the deterministic halo density field (for fixed phases  $\delta_{\text{in}}$ ) which can be found using the forward model,  $\varepsilon(\mathbf{q})$  is the noise field and  $m_k$  is the number of modes inside that bin. We are interested in the variance of  $P_h(k)$ , i.e.,

$$\text{Var}_{\text{fix}}[P_h(k)] = \langle P_h^2(k) \rangle - \langle P_h(k) \rangle^2 \quad (\text{A.2})$$

$$= \frac{1}{m_k^2} \sum_{\mathbf{q}, \mathbf{q}'}^{||\mathbf{q}, \mathbf{q}'| - k| < \Delta k/2} (\langle |\delta_h(\mathbf{q})|^2 |\delta_h(\mathbf{q}')|^2 \rangle - \langle |\delta_h(\mathbf{q})|^2 \rangle \langle |\delta_h(\mathbf{q}')|^2 \rangle), \quad (\text{A.3})$$

in the case where  $\delta_{\text{det}}(\mathbf{k})$  is fixed. We start by focusing on the right-hand side of Eq. (A.3). The expected value  $\langle |\delta_h(\mathbf{q})|^2 \rangle$  for a single mode  $\mathbf{q}$  can be written as

$$\langle |\delta_h(\mathbf{q})|^2 \rangle = \int \mathcal{D}\varepsilon \mathcal{P}(\varepsilon|P_\varepsilon) |\delta_{\text{det}}(\mathbf{q}) + \varepsilon(\mathbf{q})|^2, \quad (\text{A.4})$$

where  $\mathcal{P}(\varepsilon|P_\varepsilon)$  is a multivariate Gaussian given by

$$\mathcal{P}(\varepsilon|P_\varepsilon) = \frac{1}{\sqrt{(2\pi P_\varepsilon)^{m_k}}} \exp \left[ -\frac{1}{2} \sum_{\mathbf{p}}^{m_k} \frac{|\varepsilon(\mathbf{p})|^2}{P_\varepsilon} \right] \quad (\text{A.5})$$

and  $P_\varepsilon \propto \sigma_\varepsilon^2$  is the noise power spectrum. Notice that in Eq. (A.4) we integrate only over  $\varepsilon$ , since the value of  $\delta_{\text{det}}$  is fixed. Inserting

$$|\delta_{\text{det}}(\mathbf{q}) + \varepsilon(\mathbf{q})|^2 = |\delta_{\text{det}}(\mathbf{q})|^2 + 2\text{Re}[\delta_{\text{det}}(\mathbf{q})\varepsilon^*(\mathbf{q})] + |\varepsilon(\mathbf{q})|^2 \quad (\text{A.6})$$

in the integral of Eq. (A.4), only the first two terms will survive. The last term integrates to zero since  $\mathcal{P}(\varepsilon|P_\varepsilon)$  is a symmetric function. Therefore, Eq. (A.4) becomes

$$\langle |\delta_h(\mathbf{q})|^2 \rangle = \frac{1}{\sqrt{(2\pi P_\varepsilon)^{m_k}}} \int \mathcal{D}\varepsilon(\mathbf{p}) \exp \left[ -\frac{1}{2} \sum_{\mathbf{p} \neq \mathbf{q}}^{m_k} \frac{|\varepsilon(\mathbf{p})|^2}{P_\varepsilon} \right] \quad (\text{A.7})$$

$$\times \int \mathcal{D}\varepsilon(\mathbf{q}) \exp \left[ -\frac{1}{2} \frac{|\varepsilon(\mathbf{q})|^2}{P_\varepsilon} \right] (|\delta_{\det}(\mathbf{q})|^2 + |\varepsilon(\mathbf{q})|^2). \quad (\text{A.8})$$

This allows us to perform the integration for a single mode  $\mathbf{q}$  and obtain

$$\langle |\delta_h(\mathbf{q})|^2 \rangle = |\delta_{\det}(\mathbf{q})|^2 + P_\varepsilon. \quad (\text{A.9})$$

This holds equivalently for  $\mathbf{q}'$ , while the result for the whole bin can be found by summing over all the modes. Now let us focus on the first term in Eq. (A.3),  $\langle P_h^2(k) \rangle$ , where  $\langle |\delta_h(\mathbf{q})|^2 |\delta_h(\mathbf{q}')|^2 \rangle = \langle |\delta_{\det}(\mathbf{q}) + \varepsilon(\mathbf{q})|^2 |\delta_{\det}(\mathbf{q}') + \varepsilon(\mathbf{q}')|^2 \rangle$  can be expanded as

$$\begin{aligned} \langle |\delta_h(\mathbf{q})|^2 |\delta_h(\mathbf{q}')|^2 \rangle &= \langle (|\delta_{\det}(\mathbf{q})|^2 + 2\text{Re}[\delta_{\det}(\mathbf{q})\varepsilon^*(\mathbf{q})] + |\varepsilon(\mathbf{q})|^2) \\ &\quad \times (|\delta_{\det}(\mathbf{q}')|^2 + 2\text{Re}[\delta_{\det}(\mathbf{q}')\varepsilon^*(\mathbf{q}')] + |\varepsilon(\mathbf{q}')|^2) \rangle \\ &= \langle |\delta_{\det}(\mathbf{q})|^2 |\delta_{\det}(\mathbf{q}')|^2 + |\delta_{\det}(\mathbf{q})|^2 |\varepsilon(\mathbf{q}')|^2 + |\varepsilon(\mathbf{q})|^2 |\delta_{\det}(\mathbf{q}')|^2 \\ &\quad + |\varepsilon(\mathbf{q})|^2 |\varepsilon(\mathbf{q}')|^2 + 4\text{Re}[\delta_{\det}(\mathbf{q})\varepsilon^*(\mathbf{q})]\text{Re}[\delta_{\det}(\mathbf{q}')\varepsilon^*(\mathbf{q}')] \rangle. \end{aligned} \quad (\text{A.10})$$

From the previous calculation of  $\langle |\delta_h(\mathbf{q})|^2 \rangle$ , we already know how to calculate the expected values encountered in Eq. (A.10). What is left for us to understand are the ones shown in the last line, Eq. (A.11). Regarding the first term, since  $\varepsilon$  is a random Gaussian field, by Wick's theorem we obtain

$$\begin{aligned} \langle \varepsilon(\mathbf{q})\varepsilon^*(\mathbf{q})\varepsilon(\mathbf{q}')\varepsilon^*(\mathbf{q}') \rangle &= \langle \varepsilon(\mathbf{q})\varepsilon^*(\mathbf{q}) \rangle \langle \varepsilon(\mathbf{q}')\varepsilon^*(\mathbf{q}') \rangle \\ &\quad + \langle \varepsilon(\mathbf{q})\varepsilon(\mathbf{q}') \rangle \langle \varepsilon^*(\mathbf{q})\varepsilon^*(\mathbf{q}') \rangle + \langle \varepsilon(\mathbf{q})\varepsilon^*(\mathbf{q}') \rangle \langle \varepsilon^*(\mathbf{q})\varepsilon(\mathbf{q}') \rangle \\ &= P_\varepsilon^2 (1 + \delta_{\mathbf{q},-\mathbf{q}'} + \delta_{\mathbf{q},\mathbf{q}'}). \end{aligned} \quad (\text{A.12})$$

Regarding the last term from Eq. (A.11), we can expand it as

$$\begin{aligned} \langle 4\text{Re}[\delta_{\det}(\mathbf{q})\varepsilon^*(\mathbf{q})]\text{Re}[\delta_{\det}(\mathbf{q}')\varepsilon^*(\mathbf{q}')] \rangle &= \langle [\delta_{\det}(\mathbf{q})\varepsilon^*(\mathbf{q}) + \delta_{\det}^*(\mathbf{q})\varepsilon(\mathbf{q})][\delta_{\det}(\mathbf{q}')\varepsilon^*(\mathbf{q}') + \delta_{\det}^*(\mathbf{q}')\varepsilon(\mathbf{q}')] \rangle \\ &= \langle \delta_{\det}(\mathbf{q})\varepsilon^*(\mathbf{q})\delta_{\det}(\mathbf{q}')\varepsilon^*(\mathbf{q}') + \delta_{\det}(\mathbf{q})\varepsilon^*(\mathbf{q})\delta_{\det}^*(\mathbf{q}')\varepsilon(\mathbf{q}') \\ &\quad + \delta_{\det}^*(\mathbf{q})\varepsilon(\mathbf{q})\delta_{\det}(\mathbf{q}')\varepsilon^*(\mathbf{q}') + \delta_{\det}^*(\mathbf{q})\varepsilon(\mathbf{q})\delta_{\det}^*(\mathbf{q}')\varepsilon(\mathbf{q}') \rangle. \end{aligned} \quad (\text{A.13})$$

$$\quad (\text{A.14})$$

Let us inspect how to calculate the expectation value of the first contribution of Eq. (A.13),

$$\begin{aligned} \langle \delta_{\det}(\mathbf{q})\varepsilon^*(\mathbf{q})\delta_{\det}(\mathbf{q}')\varepsilon^*(\mathbf{q}') \rangle &= \frac{1}{\sqrt{(2\pi P_\varepsilon)^{m_k}}} \int \mathcal{D}\varepsilon(\mathbf{p}) \exp \left[ -\frac{1}{2} \sum_{\mathbf{p} \neq \mathbf{q}}^{m_k} \frac{|\varepsilon(\mathbf{p})|^2}{P_\varepsilon} \right] \\ &\quad \times \int \mathcal{D}\varepsilon(\mathbf{q}) \exp \left[ -\frac{1}{2} \frac{|\varepsilon(\mathbf{q})|^2}{P_\varepsilon} \right] \delta_{\det}(\mathbf{q})\varepsilon^*(\mathbf{q})\delta_{\det}(\mathbf{q}')\varepsilon^*(\mathbf{q}') \\ &= |\delta_{\det}(\mathbf{q})|^2 P_\varepsilon \delta_{\mathbf{q},-\mathbf{q}'}. \end{aligned} \quad (\text{A.15})$$

The calculation for the other three contributions of Eqs. (A.13)–(A.14) follows similarly. Collecting terms, we have that

$$\begin{aligned} \langle |\delta_h(\mathbf{q})|^2 |\delta_h(\mathbf{q}')|^2 \rangle &= |\delta_{\det}(\mathbf{q})|^2 |\delta_{\det}(\mathbf{q}')|^2 + |\delta_{\det}(\mathbf{q})|^2 P_\varepsilon + |\delta_{\det}(\mathbf{q}')|^2 P_\varepsilon \\ &\quad + P_\varepsilon^2 (1 + \delta_{\mathbf{q},-\mathbf{q}'} + \delta_{\mathbf{q},\mathbf{q}'}) + 2|\delta_{\det}(\mathbf{q})|^2 P_\varepsilon (\delta_{\mathbf{q},-\mathbf{q}'} + \delta_{\mathbf{q},\mathbf{q}'}) \end{aligned} \quad (\text{A.16})$$

By inserting Eq. (A.16) and the values of Eq. (A.9) for  $\mathbf{q}$  and  $\mathbf{q}'$  into the expression for the variance of the power spectrum given by Eq. (A.3), we find that

$$\begin{aligned} \text{Var}_{\text{fix}}[P_h(k)] &= \frac{1}{m_k^2} \sum_{\mathbf{q}, \mathbf{q}'}^{|\mathbf{q}, \mathbf{q}'| - k < \Delta k/2} [\langle |\delta_h(\mathbf{q})|^2 |\delta_h(\mathbf{q}')|^2 \rangle - \langle |\delta_h(\mathbf{q})|^2 \rangle \langle |\delta_h(\mathbf{q}')|^2 \rangle] \\ &= \frac{1}{m_k^2} \sum_{\mathbf{q}, \mathbf{q}'}^{|\mathbf{q}, \mathbf{q}'| - k < \Delta k/2} [|\delta_{\det}(\mathbf{q})|^2 |\delta_{\det}(\mathbf{q}')|^2 + P_\varepsilon (|\delta_{\det}(\mathbf{q})|^2 + |\delta_{\det}(\mathbf{q}')|^2) + P_\varepsilon^2 \\ &\quad + (P_\varepsilon^2 + 2|\delta_{\det}(\mathbf{q})|^2 P_\varepsilon) (\delta_{\mathbf{q},-\mathbf{q}'} + \delta_{\mathbf{q},\mathbf{q}'}) - (|\delta_{\det}(\mathbf{q})|^2 + P_\varepsilon) (|\delta_{\det}(\mathbf{q}')|^2 + P_\varepsilon)] . \end{aligned} \quad (\text{A.17})$$

Summing over  $\mathbf{q}'$ , we finally obtain the power-spectrum variance when the phases of  $\delta$  are fixed,

$$\text{Var}_{\text{fix}}[P_h(k)] = \frac{2P_\varepsilon}{m_k^2} \sum_{\mathbf{q}}^{|\mathbf{q}| - k < \Delta k/2} (2|\delta_{\det}(\mathbf{q})|^2 + P_\varepsilon) . \quad (\text{A.18})$$

Using a mock generator for  $\delta_{\det} = b_1 \delta$  in which the phases of  $\delta$  are fixed, we verify in Fig. A.1 that this prediction accurately matches the variance of  $10^3$  power spectra measured in a  $512h^{-1}\text{Mpc}$  box with  $128^3$  cells.

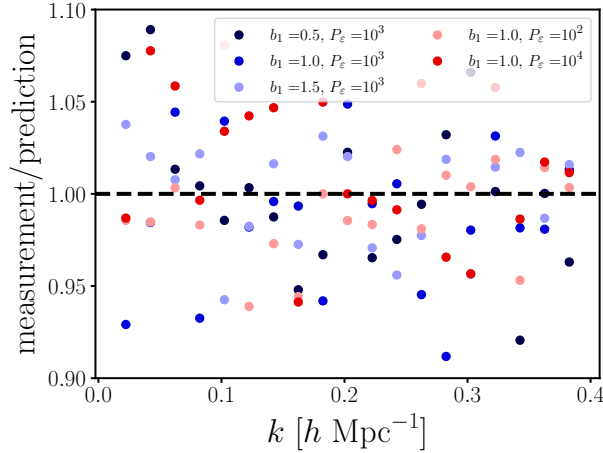


Figure A.1: Ratio of the variance of  $10^3$  power spectra with fixed phases to the prediction obtained in Eq. (A.18) for a variety of bias and noise parameters.



# Appendix B

## Details of Data Analysis

### B.1 Correlation length

In this section, we describe in detail how we conducted the analysis of field-level chains. We follow the same procedure for both mocks. For each bias expansion used to perform the inference, we analyze three  $\Lambda$  values. For each  $\Lambda$ , we run three chains. For one chain, we leverage our knowledge of the ground truth for the initial conditions and start sampling from there. The other two chains begin from random initial conditions, with a different seed used for each to ensure they start from a unique set of initial conditions. All three chains also had slightly different initial values for the cosmological parameters sampled. This approach ensured that the inferred value of BAO is independent of the sampler's starting point. As mentioned in the Sec. 8.3.1, one chain used Gaussian prior for bias, while the other two used uniform priors; however, these priors were essentially uninformative, as the bias parameters are well constrained by the data (at least when sampling only  $\beta$  as cosmological parameter),

To perform the analysis, we combine the three independent chains into one large chain, which consists of  $N$  elements; for a parameter  $f$ , we label the sample points as  $\{f_s\}$ , after discarding the burn-in portion of each chain, which was about 5 correlation lengths. To denote the mean of the dataset, we use  $\langle f_s \rangle \equiv \bar{f} = \frac{1}{N} \sum_{s=1}^N f_s$ . We continue running the chains until we achieve 100 effective samples of the  $\beta$  parameter for each dataset and  $\Lambda$  considered. The number of effective samples is calculated by dividing the total number of samples,  $N$ , by the auto-correlation length. The auto-correlation length for an MCMC chain indicates the number of steps required within the chain to obtain samples that are independent of each other. Correlation length can be estimated using the relation

$$\hat{\tau}_f(M) = 1 + 2 \sum_{\tau=1}^M \hat{\rho}_f(\tau), \quad (\text{B.1})$$

where  $\hat{\rho}$  is the normalized autocorrelation function

$$\rho(\tau) = \frac{\mathcal{A}(\tau)}{\mathcal{A}(0)}, \quad (\text{B.2})$$

and

$$\mathcal{A}(\tau) = \langle f_s f_{s+\tau} \rangle_s - \langle f_s \rangle_s^2. \quad (\text{B.3})$$

is the auto-correlation function.  $M$  is the maximum separation between the samples considered. As the best choice for  $M$ , [127] suggests using the smallest value of  $M$  such that  $M \geq C \hat{\tau}_f(M)$  for a constant  $C$  chosen to minimize the covariance of the estimator. This is usually achieved for values of  $C$  close to 5. Plots indicating  $\tau_f$  values of  $\beta$  for chains analyzed in the chapter are shown below. In the tables below, we summarize the correlation lengths for the parameter  $\beta$ .

$\Lambda [h \text{Mpc}^{-1}]$	0.15	0.18	0.2
$\tau$			
Chain 1	210	683	101
Chain 2	165	728	132
Chain 3	175	609	261

Table B.1: Correlation length values for chains run on the Mock A using Lagrangian bias.

$\Lambda [h \text{Mpc}^{-1}]$	0.15	0.18	0.2
$\tau$			
Chain 1	350	252	507
Chain 2	272	771	728
Chain 3	212	123	609

Table B.2: Correlation length values for chains run on the Mock B using Lagrangian bias.

$\Lambda [h \text{Mpc}^{-1}]$	0.15	0.18	0.2
$\tau$			
Chain 1	186	590	735
Chain 2	105	606	744
Chain 3	800	522	710

Table B.3: Correlation length values for chains run on the Mock B using Eulerian bias.

## B.2 Parameter posteriors: marginalized likelihood

Below we present the corner plots showing posterior distribution of parameters sampled for both mocks and cutoffs. Results for the Mock B are summarized in the Fig. B.1, where again we denote Lagrangian bias results in blue and Eulerian in orange. We notice the same trend of increasing noise as we did in Sec. 8.3.2. In Fig. B.2, we present the results for Mock A. The effective noise also grows in the case of Mock A, but in this case it is  $\sigma_\epsilon$  that grows more significantly, rather than  $\sigma_{\epsilon,2}$ .

### B.2.1 Parameter posteriors: non-marginalized likelihood

In this section, we present the results of the inference obtained using a likelihood that was not marginalized over the bias parameters. For this analysis, uniform priors were applied to the bias parameters. Specifically, a uniform prior of  $\mathcal{U}(0.01, 10)$  was used for  $b_\delta$ , while all other bias parameters were assigned a uniform prior of  $\mathcal{U}(-30, 30)$ . For the inference process, two chains per sample were initiated, each starting from random initial conditions  $\hat{s}$  and a different initial value of  $\beta$ . These chains converged quickly to a similar  $\beta$  value, as illustrated in Figure B.3, which displays the trace plot of  $\beta$  for Mock B sampled with Eulerian bias at  $\Lambda = 0.15 h \text{ Mpc}^{-1}$ . The chains were run until 100 effective samples were obtained.

In Fig. B.4 we show the auto-correlation plot for one of the chains. We see that the correlation length for  $\beta$  is very short even in the case when the non-marginalized likelihood is used. In fact, the correlation length is shorter than for the marginalized likelihood in this case (Tab. B.3), in contrast to the findings for  $\sigma_8$  in [71]. This finding is clearly worth further investigation; note that the parameter posteriors show no significant correlations of  $\beta$  with any other parameter.

Finally, Figure B.5 displays the corner plots for all sampled parameters, including the mean value and the size of the error bars for each parameter. Comparing the size of the error bars for  $\sigma(\beta)$  in this plot with those in Figure B.1a reveals that the error bar size for  $\beta$  does not depend on the type of likelihood used, as expected. Furthermore, the values of  $\sigma_\epsilon$  and  $\sigma_{\epsilon,2}$  are consistent with those obtained using the marginalized likelihood.

The inferred values of the bias parameters differ from those used to generate the mock data, due to the mismatch in  $\Lambda$  between the generation and sampling of the mock data [107]. That is, the bias parameters and stochastic parameters are expected to run with  $\Lambda$ , while the inferred cosmological parameter, in this case  $\beta$ , should be consistent with the ground truth value.

The same analysis using the non-marginalized likelihood has been applied to Mock A sampled with the Lagrangian bias. The results of this analysis are summarized in Fig. B.6. Similarly as in the case of mock B, we find that the error bar  $\sigma(\beta)$  is the same as when the marginalized likelihood is used for the same cutoff.

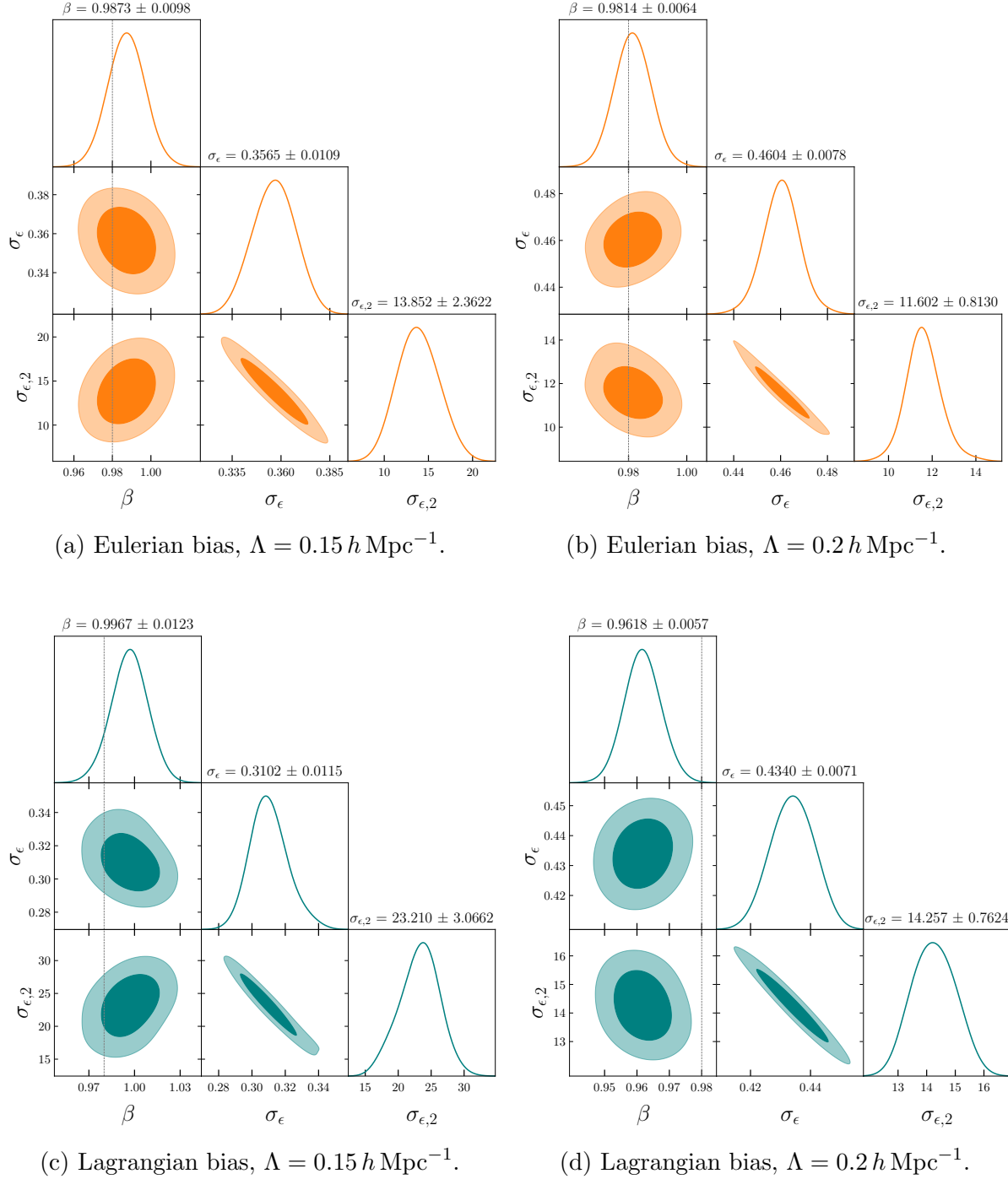


Figure B.1: Posterior of parameters for the inference performed on Mock B. Top two panels (orange color) corresponds to Eulerian bias, while the lower two panels (blue) correspond to Lagrangian bias. The intermediate cutoff  $\Lambda = 0.18 h \text{ Mpc}^{-1}$  behaves similarly, and is not shown here for brevity.

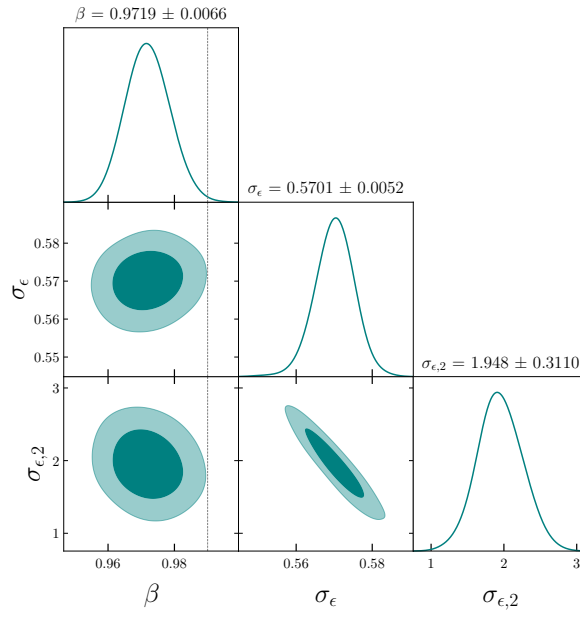
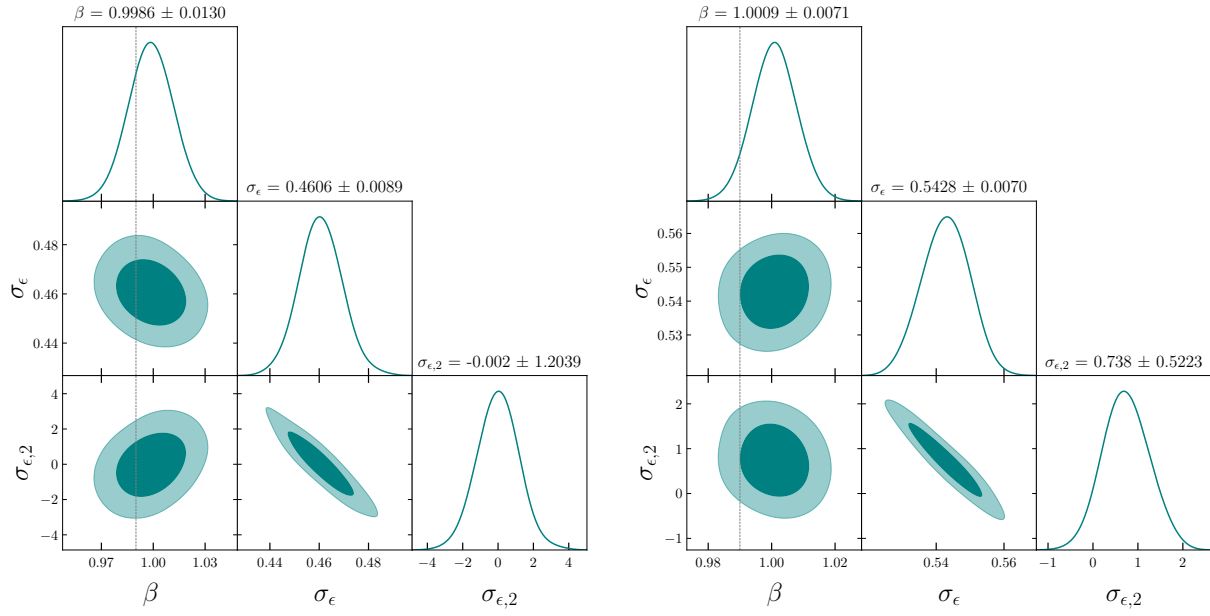


Figure B.2: Posterior of parameters for the inference performed on Mock A.

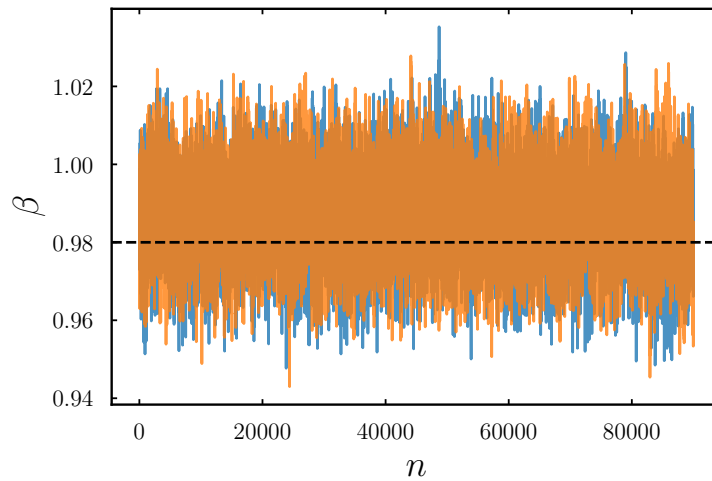


Figure B.3: Trace plot for parameter  $\beta$  in chains generated using the non-marginalized likelihood. Inference was performed at  $\Lambda = 0.15 h \text{ Mpc}^{-1}$  for Mock B.

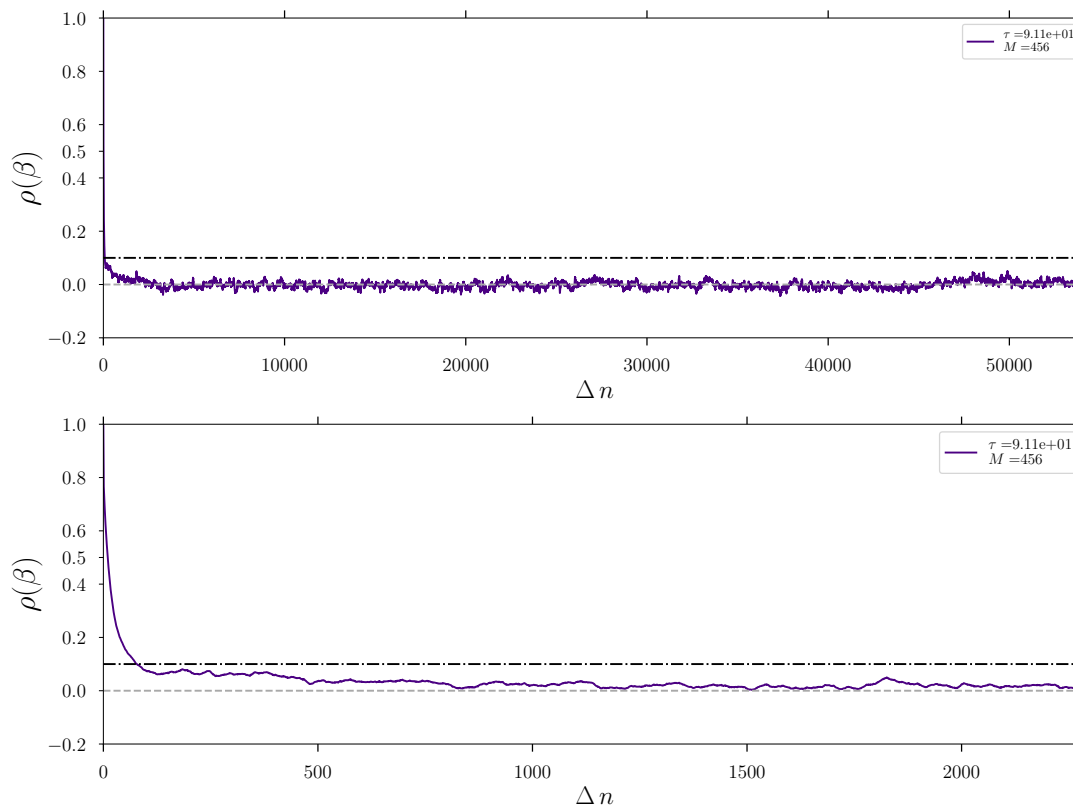


Figure B.4: The normalized auto-correlation function for parameter  $\beta$  inferred at  $\Lambda = 0.15 h \text{ Mpc}^{-1}$  using the non-marginalized likelihood. We also show the correlation length value  $\tau$  together with the maximum separation  $M$  between the samples considered. The lower panel zooms in on the first 3000 samples.

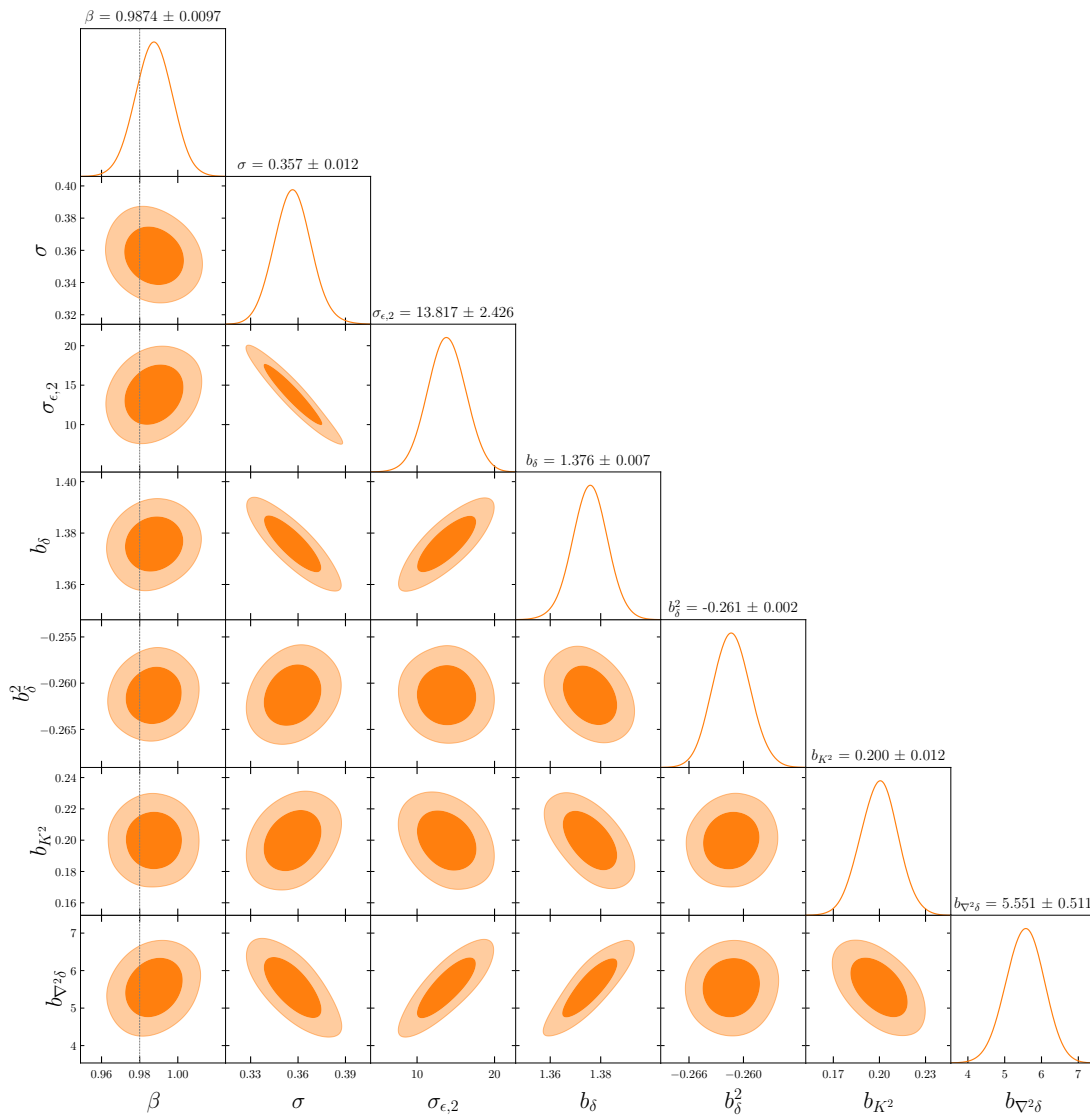


Figure B.5: Results of the joint FreeIC inference on the Mock B using non-marginalized likelihood and Eulerian bias. We show the posterior for all noise parameters, bias parameters and  $\beta$ . Inference was performed at  $\Lambda = 0.15 h \text{ Mpc}^{-1}$ .

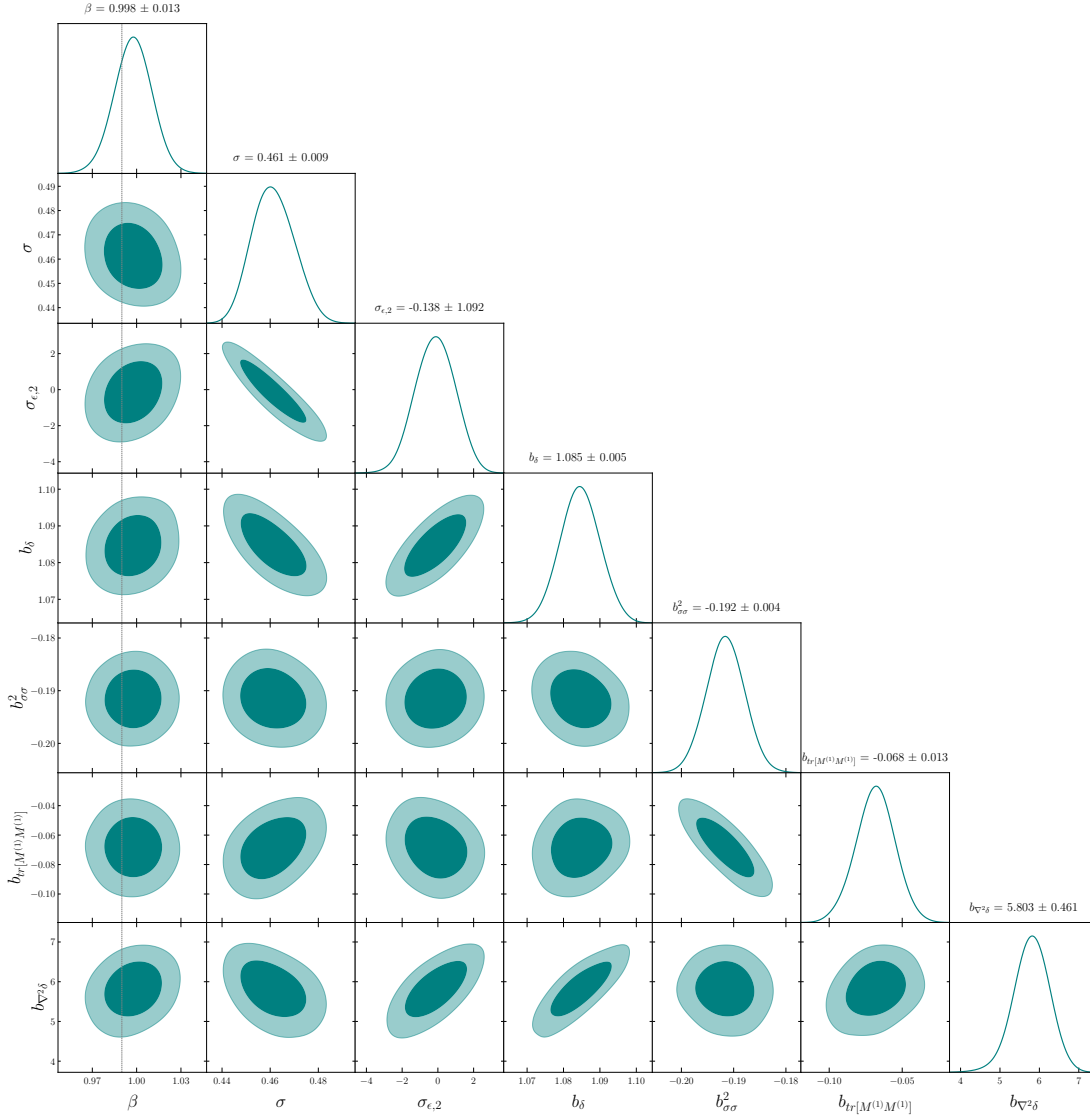


Figure B.6: Results of the joint FreeIC inference on the Mock A using non-marginalized likelihood and Lagrangian bias. We show the posterior for all noise parameters, bias parameters and  $\beta$ . Inference was performed at  $\Lambda = 0.15 h \text{ Mpc}^{-1}$ .

# Bibliography

- [1] A.A. Abolhasani, M. Mirbabayi und E. Pajer, *Journal of Cosmology and Astroparticle Physics* **2016** (2016), 063063.
- [2] N. Aghanim, Y. Akrami, M. Ashdown, J. Aumont, C. Baccigalupi, M. Ballardini, A.J. Banday, R.B. Barreiro, N. Bartolo, S. Basak, R. Battye, K. Benabed, J.P. Bernard, M. Bersanelli, P. Bielewicz, J.J. Bock, J.R. Bond, J. Borrill, F.R. Bouchet, F. Boulanger, M. Bucher, C. Burigana, R.C. Butler, E. Calabrese, J.F. Cardoso, J. Carron, A. Challinor, H.C. Chiang, J. Chluba, L.P.L. Colombo, C. Combet, D. Contreras, B.P. Crill, F. Cuttaia, P. de Bernardis, G. de Zotti, J. Delabrouille, J.M. Delouis, E. Di Valentino, J.M. Diego, O. Dor, M. Douspis, A. Ducout, X. Dupac, S. Dusini, G. Efstathiou, F. Elsner, T.A. Enlin, H.K. Eriksen, Y. Fantaye, M. Farhang, J. Fergusson, R. Fernandez-Cobos, F. Finelli, F. Forastieri, M. Frailis, A.A. Fraisse, E. Franceschi, A. Frolov, S. Galeotta, S. Galli, K. Ganga, R.T. Gnova-Santos, M. Gerbino, T. Ghosh, J. Gonzalez-Nuevo, K.M. Grski, S. Gratton, A. Gruppuso, J.E. Gudmundsson, J. Hamann, W. Handley, F.K. Hansen, D. Herranz, S.R. Hildebrandt, E. Hivon, Z. Huang, A.H. Jaffe, W.C. Jones, A. Karakci, E. Keihnen, R. Keskitalo, K. Kiiveri, J. Kim, T.S. Kisner, L. Knox, N. Krachmalnicoff, M. Kunz, H. Kurki-Suonio, G. Lagache, J.M. Lamarre, A. Lasenby, M. Lattanzi, C.R. Lawrence, M. Le Jeune, P. Lemos, J. Lesgourgues, F. Levrier, A. Lewis, M. Liguori, P.B. Lilje, M. Lilley, V. Lindholm, M. Lopez-Caniego, P.M. Lubin, Y.Z. Ma, J.F. Macas-Prez, G. Maggio, D. Maino, N. Mandolesi, A. Mangilli, A. Marcos-Caballero, M. Maris, P.G. Martin, M. Martinelli, E. Martinez-Gonzalez, S. Matarrese, N. Mauri, J.D. McEwen, P.R. Meinhold, A. Melchiorri, A. Mennella, M. Migliaccio, M. Millea, S. Mitra, M.A. Miville-Deschne, D. Molinari, L. Montier, G. Morgante, A. Moss, P. Natoli, H.U. Nrgaard-Nielsen, L. Pagano, D. Paoletti, B. Partridge, G. Patanchon, H.V. Peiris, F. Perrotta, V. Pettorino, F. Piacentini, L. Polastri, G. Polenta, J.L. Puget, J.P. Rachen, M. Reinecke, M. Remazeilles, A. Renzi, G. Rocha, C. Rosset, G. Roudier, J.A. Rubio-Martn, B. Ruiz-Granados, L. Salvati, M. Sandri, M. Savelainen, D. Scott, E.P.S. Shellard, C. Sirignano, G. Sirri, L.D. Spencer, R. Sunyaev, A. Suur-Uski, J.A. Tauber, D. Tavagnacco, M. Tenti, L. Toffolatti, M. Tomasi, T. Trombetti, L. Valenziano, J. Valiviita, B. Van Tent, L. Vibert, P. Vielva, F. Villa, N. Vittorio, B.D. Wandelt, I.K. Wehus, M. White, S.D.M. White, A. Zacchei und A. Zonca, *Astronomy & Astrophysics* **641** (2020), A6.

- [3] S. Alam, M. Ata, S. Bailey, F. Beutler, D. Bizyaev, J.A. Blazek, A.S. Bolton, J.R. Brownstein, A. Burden, C.H. Chuang, J. Comparat, A.J. Cuesta, K.S. Dawson, D.J. Eisenstein, S. Escoffier, H. Gil-Marn, J.N. Grieb, N. Hand, S. Ho, K. Kinemuchi, D. Kirkby, F. Kitaura, E. Malanushenko, V. Malanushenko, C. Maraston, C.K. McBride, R.C. Nichol, M.D. Olmstead, D. Oravetz, N. Padmanabhan, N. Palanque-Delabrouille, K. Pan, M. Pellejero-Ibanez, W.J. Percival, P. Petitjean, F. Prada, A.M. Price-Whelan, B.A. Reid, S.A. Rodriguez-Torres, N.A. Roe, A.J. Ross, N.P. Ross, G. Rossi, J.A. Rubio-Martín, S. Saito, S. Salazar-Albornoz, L. Samushia, A.G. Sánchez, S. Satpathy, D.J. Schlegel, D.P. Schneider, C.G. Scoccola, H.J. Seo, E.S. Sheldon, A. Simmons, A. Slosar, M.A. Strauss, M.E.C. Swanson, D. Thomas, J.L. Tinker, R. Tojeiro, M.V. Magaia, J.A. Vazquez, L. Verde, D.A. Wake, Y. Wang, D.H. Weinberg, M. White, W.M. Wood-Vasey, C. Yche, I. Zehavi, Z. Zhai und G.B. Zhao, *Monthly Notices of the Royal Astronomical Society* **470** (2017), 26172652.
- [4] C. Alcock und B. Paczynski, *Nature* **281** (1979), 358.
- [5] L. Anderson, E. Aubourg, S. Bailey, F. Beutler, A.S. Bolton, J. Brinkmann, J.R. Brownstein, C.H. Chuang, A.J. Cuesta, K.S. Dawson, D.J. Eisenstein, S. Ho, K. Honscheid, E.A. Kazin, D. Kirkby, M. Manera, C.K. McBride, O. Mena, R.C. Nichol, M.D. Olmstead, N. Padmanabhan, N. Palanque-Delabrouille, W.J. Percival, F. Prada, A.J. Ross, N.P. Ross, A.G. Sánchez, L. Samushia, D.J. Schlegel, D.P. Schneider, H.J. Seo, M.A. Strauss, D. Thomas, J.L. Tinker, R. Tojeiro, L. Verde, D. Wake, D.H. Weinberg, X. Xu und C. Yèche, *Monthly Notices of the Royal Astronomical Society* **439** (2014), 83101.
- [6] R. Angulo, C. Baugh, C. Frenk, R. Bower, A. Jenkins und S. Morris, *Monthly Notices of the Royal Astronomical Society* **362** (2005), L25.
- [7] R.E. Angulo, C.M. Baugh, C.S. Frenk und C.G. Lacey, *Monthly Notices of the Royal Astronomical Society* **383** (2008), 755.
- [8] R.E. Angulo, S. Foreman, M. Schmittfull und L. Senatore, *Journal of Cosmology and Astroparticle Physics* **2015** (2015), 039039.
- [9] V. Assassi, D. Baumann, D. Green und M. Zaldarriaga, *Journal of Cosmology and Astroparticle Physics* **2014** (2014), 056056.
- [10] M. Ata, F.S. Kitaura, C.H. Chuang, S. Rodriguez-Torres, R.E. Angulo, S. Ferraro, H. Gil-Marn, P. McDonald, C.H. Monteagudo, V. Müller und et al., *Monthly Notices of the Royal Astronomical Society* (2017), stx178.
- [11] I. Babić, F. Schmidt und B. Tucci, *Journal of Cosmology and Astroparticle Physics* **2022** (2022), 007.

- [12] I. Babić, F. Schmidt und B. Tucci. *Straightening the Ruler: Field-Level Inference of the BAO Scale with LEFTfield*, 2024.
- [13] T. Baldauf: *Effective Field Theory of Large-Scale Structure: Lecture Notes of the Les Houches Summer School*. Oxford University Press, 2020.
- [14] A.H. Barnett, J.F. Magland und L. af Klinteberg. *A parallel non-uniform fast Fourier transform library based on an exponential of semicircle kernel*, 2019.
- [15] A. Barreira, T. Lazeyras und F. Schmidt, *Journal of Cosmology and Astroparticle Physics* **2021** (2021), 029.
- [16] B.A. Bassett und R. Hlozek. *Baryon Acoustic Oscillations*, 2009.
- [17] D. Baumann, A. Nicolis, L. Senatore und M. Zaldarriaga, *Journal of Cosmology and Astroparticle Physics* **2012** (2012), 051051.
- [18] D. Baumann, A. Nicolis, L. Senatore und M. Zaldarriaga, *Journal of Cosmology and Astroparticle Physics* **2012** (2012), 051051.
- [19] F. Bernardeau, S. Colombi, E. Gaztaaga und R. Scoccimarro, *Physics Reports* **367** (2002), 1248.
- [20] D. Bertolini, K. Schutz, M.P. Solon und K.M. Zurek, *Journal of Cosmology and Astroparticle Physics* **2016** (2016), 052052.
- [21] Beyond-2pt Collaboration, :, E. Krause, Y. Kobayashi, A.N. Salcedo, M.M. Ivanov, T. Abel, K. Akitsu, R.E. Angulo, G. Cabass, S. Contarini, C. Cuesta-Lazaro, C. Hahn, N. Hamaus, D. Jeong, C. Modi, N.M. Nguyen, T. Nishimichi, E. Pailas, M. Pellejero Ibañez, O.H.E. Philcox, A. Pisani, F. Schmidt, S. Tanaka, G. Verza, S. Yuan und M. Zennaro, *arXiv e-prints* (2024), arXiv:2405.02252.
- [22] C. Blake, E.A. Kazin, F. Beutler, T.M. Davis, D. Parkinson, S. Brough, M. Colless, C. Contreras, W. Couch, S. Croom, D. Croton, M.J. Drinkwater, K. Forster, D. Gilbank, M. Gladders, K. Glazebrook, B. Jelliffe, R.J. Jurek, I.h. Li, B. Madore, D.C. Martin, K. Pimblet, G.B. Poole, M. Pracy, R. Sharp, E. Wisnioski, D. Woods, T.K. Wyder und H.K.C. Yee, *Monthly Notices of the Royal Astronomical Society* **418** (2011), 17071724.
- [23] C. Blake, D. Parkinson, B. Bassett, K. Glazebrook, M. Kunz und R.C. Nichol, *Monthly Notices of the Royal Astronomical Society* **365** (2006), 255.
- [24] F.R. Bouchet, S. Colombi, E. Hivon und R. Juszkiewicz. *Perturbative Lagrangian Approach to Gravitational Instability*, 1994.
- [25] T. Buchert, *Astron. Astrophys.* **223** (1989), 9.

- [26] T. Buchert, *Monthly Notices of the Royal Astronomical Society* **254** (1992), 729.
- [27] T. Buchert, *Astron. Astrophys.* **267** (1993), L51.
- [28] A. Burden, W.J. Percival und C. Howlett, *Monthly Notices of the Royal Astronomical Society* **453** (2015), 456468.
- [29] G. Cabass und F. Schmidt, *Journal of Cosmology and Astroparticle Physics* **2020** (2020), 042042.
- [30] J.J.M. Carrasco, M.P. Hertzberg und L. Senatore, *Journal of High Energy Physics* **2012** (2012).
- [31] J.J.M. Carrasco, M.P. Hertzberg und L. Senatore, *Journal of High Energy Physics* **2012** (2012).
- [32] J.J.M. Carrasco, M.P. Hertzberg und L. Senatore, *Journal of High Energy Physics* **2012** (2012).
- [33] S.M. Carroll, S. Leichenauer und J. Pollack, *Physical Review D* **90** (2014).
- [34] P. Catelan, *Mon. Not. Roy. Astron. Soc.* **276** (1995), 115.
- [35] S.F. Chen, Z. Vlah und M. White, *Journal of Cosmology and Astroparticle Physics* **2020** (2020), 062062.
- [36] P. Coles und P. Erdodu, *Journal of Cosmology and Astroparticle Physics* **2007** (2007), 007007.
- [37] D. Collaboration, A.G. Adame, J. Aguilar, S. Ahlen, S. Alam, D.M. Alexander, M. Alvarez, O. Alves, A. Anand, U. Andrade, E. Armengaud, S. Avila, A. Aviles, H. Awan, B. Bahr-Kalus, S. Bailey, C. Baltay, A. Bault, J. Behera, S. BenZvi, A. Bera, F. Beutler, D. Bianchi, C. Blake, R. Blum, S. Brieden, A. Brodzeller, D. Brooks, E. Buckley-Geer, E. Burtin, R. Calderon, R. Canning, A.C. Rosell, R. Cereskaite, J.L. Cervantes-Cota, S. Chabanier, E. Chaussidon, J. Chaves-Montero, S. Chen, X. Chen, T. Claybaugh, S. Cole, A. Cuceu, T.M. Davis, K. Dawson, A. de la Macorra, A. de Mattia, N. Deiosso, A. Dey, B. Dey, Z. Ding, P. Doel, J. Edelstein, S. Eftekhazadeh, D.J. Eisenstein, A. Elliott, P. Fagrelus, K. Fanning, S. Ferraro, J. Ereza, N. Findlay, B. Flaugher, A. Font-Ribera, D. Forero-Snchez, J.E. Forero-Romero, C.S. Frenk, C. Garcia-Quintero, E. Gaztaaga, H. Gil-Marn, S.G.A. Gontcho, A.X. Gonzalez-Morales, V. Gonzalez-Perez, C. Gordon, D. Green, D. Gruen, R. Gspaner, G. Gutierrez, J. Guy, B. Hadzhiyska, C. Hahn, M.M.S. Hanif, H.K. Herrera-Alcantar, K. Honscheid, C. Howlett, D. Huterer, V. Iri, M. Ishak, S. Juneau, N.G. Karaayl, R. Kehoe, S. Kent, D. Kirkby, A. Kremin, A. Krolewski, Y. Lai, T.W. Lan, M. Landriau, D. Lang, J. Lasker, J.M.L. Goff,

- L.L. Guillou, A. Leauthaud, M.E. Levi, T.S. Li, E. Linder, K. Lodha, C. Magneville, M. Manera, D. Margala, P. Martini, M. Maus, P. McDonald, L. Medina-Varela, A. Meisner, J. Mena-Fernandez, R. Miquel, J. Moon, S. Moore, J. Moustakas, N. Mudur, E. Mueller, A. Muoz-Gutierrez, A.D. Myers, S. Nadathur, L. Napolitano, R. Neveux, J.A. Newman, N.M. Nguyen, J. Nie, G. Niz, H.E. Noriega, N. Padmanabhan, E. Paillas, N. Palanque-Delabrouille, J. Pan, S. Penmetsa, W.J. Percival, M.M. Pieri, M. Pinon, C. Poppett, A. Porredon, F. Prada, A. Prez-Fernandez, I. Prez-Rfols, D. Rabinowitz, A. Raichoor, C. Ramirez-Prez, S. Ramirez-Solano, C. Ravoux, M. Rashkovetskyi, M. Rezaie, J. Rich, A. Rocher, C. Rockosi, N.A. Roe, A. Rosado-Marin, A.J. Ross, G. Rossi, R. Ruggeri, V. Ruhlmann-Kleider, L. Samushia, E. Sanchez, C. Saulder, E.F. Schlafly, D. Schlegel, M. Schubnell, H. Seo, A. Shafieloo, R. Sharples, J. Silber, A. Slosar, A. Smith, D. Sprayberry, T. Tan, G. Tarl, P. Taylor, S. Trusov, L.A. Urea-Lpez, R. Vaisakh, D. Valcin, F. Valdes, M. Vargas-Magaa, L. Verde, M. Walther, B. Wang, M.S. Wang, B.A. Weaver, N. Weaverdyck, R.H. Wechsler, D.H. Weinberg, M. White, J. Yu, Y. Yu, S. Yuan, C. Yche, E.A. Zaborowski, P. Zarrouk, H. Zhang, C. Zhao, R. Zhao, R. Zhou, T. Zhuang und H. Zou. *DESI 2024 VI: Cosmological Constraints from the Measurements of Baryon Acoustic Oscillations*, 2024.
- [38] R.J. Cooke, M. Pettini und C.C. Steidel, *Astrophys. J.* **855** (2018), 102.
- [39] M.P. van Daalen, J. Schaye, I.G. McCarthy, C.M. Booth und C.D. Vecchia, *Monthly Notices of the Royal Astronomical Society* **440** (2014), 29973010.
- [40] K.S. Dawson, J.P. Kneib, W.J. Percival, S. Alam, F.D. Albareti, S.F. Anderson, E. Armengaud, . Aubourg, S. Bailey, J.E. Bautista, A.A. Berlind, M.A. Bershad, F. Beutler, D. Bizyaev, M.R. Blanton, M. Blomqvist, A.S. Bolton, J. Bovy, W.N. Brandt, J. Brinkmann, J.R. Brownstein, E. Burtin, N.G. Busca, Z. Cai, C.H. Chuang, N. Clerc, J. Comparat, F. Cope, R.A.C. Croft, I. Cruz-Gonzalez, L.N.d. Costa, M.C. Cousinou, J. Darling, A.d.l. Macorra, S.d.l. Torre, T. Delubac, H.d.M.d. Bourboux, T. Dwelly, A. Ealet, D.J. Eisenstein, M. Eracleous, S. Escoffier, X. Fan, A. Finoguenov, A. Font-Ribera, P. Frinchaboy, P. Gaulme, A. Georgakakis, P. Green, H. Guo, J. Guy, S. Ho, D. Holder, J. Huehnerhoff, T. Hutchinson, Y. Jing, E. Jullo, V. Kamble, K. Kinemuchi, D. Kirkby, F.S. Kitaura, M.A. Klaene, R.R. Laher, D. Lang, P. Laurent, J.M.L. Goff, C. Li, Y. Liang, M. Lima, Q. Lin, W. Lin, Y.T. Lin, D.C. Long, B. Lundgren, N. MacDonald, M.A.G. Maia, E. Malanushenko, V. Malanushenko, V. Mariappan, C.K. McBride, I.D. McGreer, B. Mnard, A. Merloni, A. Meza, A.D. Montero-Dorta, D. Muna, A.D. Myers, K. Nandra, T. Naugle, J.A. Newman, P. Noterdaeme, P. Nugent, R. Ogando, M.D. Olmstead, A. Oravetz, D.J. Oravetz, N. Padmanabhan, N. Palanque-Delabrouille, K. Pan, J.K. Parejko, I. Pris, J.A. Peacock, P. Petitjean, M.M. Pieri, A. Pisani, F. Prada, A. Prakash, A. Raichoor, B. Reid, J. Rich, J. Ridl, S. Rodriguez-Torres, A.C. Rosell, A.J. Ross, G. Rossi, J. Ruan, M. Salvato, C. Sayres, D.P. Schneider, D.J. Schlegel, U. Seljak, H.J. Seo, B. Sesar, S. Shandera, Y. Shu, A. Slosar, F. Sobreira, A. Streblyanska,

- N. Suzuki, D. Taylor, C. Tao, J.L. Tinker, R. Tojeiro, M. Vargas-Magaa, Y. Wang, B.A. Weaver, D.H. Weinberg, M. White, W.M. Wood-Vasey, C. Yeche, Z. Zhai, C. Zhao, G.b. Zhao, Z. Zheng, G.B. Zhu und H. Zou, *The Astronomical Journal* **151** (2016), 44.
- [41] K.S. Dawson, D.J. Schlegel, C.P. Ahn, S.F. Anderson, . Aubourg, S. Bailey, R.H. Barkhouser, J.E. Bautista, A. Beifiori, A.A. Berlind, V. Bhardwaj, D. Bizyaev, C.H. Blake, M.R. Blanton, M. Blomqvist, A.S. Bolton, A. Borde, J. Bovy, W.N. Brandt, H. Brewington, J. Brinkmann, P.J. Brown, J.R. Brownstein, K. Bundy, N.G. Busca, W. Carithers, A.R. Carnero, M.A. Carr, Y. Chen, J. Comparat, N. Connolly, F. Cope, R.A.C. Croft, A.J. Cuesta, L.N. da Costa, J.R.A. Davenport, T. Delubac, R. de Putter, S. Dhital, A. Ealet, G.L. Ebelke, D.J. Eisenstein, S. Escoffier, X. Fan, N. Filiz Ak, H. Finley, A. Font-Ribera, R. Gnova-Santos, J.E. Gunn, H. Guo, D. Haggard, P.B. Hall, J.C. Hamilton, B. Harris, D.W. Harris, S. Ho, D.W. Hogg, D. Holder, K. Honscheid, J. Huehnerhoff, B. Jordan, W.P. Jordan, G. Kauffmann, E.A. Kazin, D. Kirkby, M.A. Klaene, J.P. Kneib, J.M. Le Goff, K.G. Lee, D.C. Long, C.P. Loomis, B. Lundgren, R.H. Lupton, M.A.G. Maia, M. Makler, E. Malanushenko, V. Malanushenko, R. Mandelbaum, M. Manera, C. Maraston, D. Margala, K.L. Masters, C.K. McBride, P. McDonald, I.D. McGreer, R.G. McMahon, O. Mena, J. Miralda-Escud, A.D. Montero-Dorta, F. Montesano, D. Muna, A.D. Myers, T. Naugle, R.C. Nichol, P. Noterdaeme, S.E. Nuza, M.D. Olmstead, A. Oravetz, D.J. Oravetz, R. Owen, N. Padmanabhan, N. Palanque-Delabrouille, K. Pan, J.K. Parejko, I. Pris, W.J. Percival, I. Prez-Fournon, I. Prez-Rfols, P. Petitjean, R. Pfaffenberger, J. Pforr, M.M. Pieri, F. Prada, A.M. Price-Whelan, M.J. Raddick, R. Rebolo, J. Rich, G.T. Richards, C.M. Rockosi, N.A. Roe, A.J. Ross, N.P. Ross, G. Rossi, J.A. Rubio-Martin, L. Samushia, A.G. Snchez, C. Sayres, S.J. Schmidt, D.P. Schneider, C.G. Scoccola, H.J. Seo, A. Sheldon, E. Sheldon, Y. Shen, Y. Shu, A. Slosar, S.A. Smee, S.A. Snedden, F. Stauffer, O. Steele, M.A. Strauss, A. Streblyanska, N. Suzuki, M.E.C. Swanson, T. Tal, M. Tanaka, D. Thomas, J.L. Tinker, R. Tojeiro, C.A. Tremonti, M. Vargas Magaa, L. Verde, M. Viel, D.A. Wake, M. Watson, B.A. Weaver, D.H. Weinberg, B.J. Weiner, A.A. West, M. White, W.M. Wood-Vasey, C. Yeche, I. Zehavi, G.B. Zhao und Z. Zheng, *The Astronomical Journal* **145** (2012), 10.
- [42] V. Desjacques, D. Jeong und F. Schmidt, *Physics Reports* **733** (2018), 1193.
- [43] V. Desjacques, D. Jeong und F. Schmidt, *Physics Reports* **733** (2018), 1193.
- [44] N.A. Dmitriev und Y.B. Zel'dovich, *JETP* **18** (1964), 793.
- [45] S. Dodelson und F. Schmidt: *Modern Cosmology*. Academic press, 2020.
- [46] A.G. Doroshkevich, Y.B. Zel'dovich und R.A. Sunyaev, *Astronomicheskii Zhurnal (AZh)* **55** (1978), 913. English translation: *Soviet Astronomy*, 22, 523–528.

- [47] J. Ehlers und T. Buchert, *Gen. Rel. Grav.* **29** (1997), 733.
- [48] D.J. Eisenstein, *New Astronomy Reviews* **49** (2005), 360.
- [49] D.J. Eisenstein und W. Hu, *The Astrophysical Journal* **496** (1998), 605614.
- [50] D.J. Eisenstein, H. Seo, E. Sirko und D.N. Spergel, *The Astrophysical Journal* **664** (2007), 675679.
- [51] D.J. Eisenstein, H. Seo und M. White, *The Astrophysical Journal* **664** (2007), 660674.
- [52] F. Elsner, F. Schmidt, J. Jasche, G. Lavaux und N.M. Nguyen, *Journal of Cosmology and Astroparticle Physics* **2020** (2020), 029029.
- [53] P. Erdodu, O. Lahav, S. Zaroubi, G. Efstathiou, S. Moody, J.A. Peacock, M. Colless, I.K. Baldry, C.M. Baugh, J. Bland-Hawthorn und et al., *Monthly Notices of the Royal Astronomical Society* **352** (2004), 939960.
- [54] K.B. Fisher, O. Lahav, Y. Hoffman, D. Lynden-Bell und S. Zaroubi, *Monthly Notices of the Royal Astronomical Society* (1995).
- [55] M.H. Goroff, B. Grinstein, S.J. Rey und M.B. Wise, *Astrophysical Journal, Part 1* **311** (1986), 6.
- [56] W. Hu und N. Sugiyama, *The Astrophysical Journal* **471** (1996), 542570.
- [57] W. Hu und M. White, *The Astrophysical Journal* **471** (1996), 3051.
- [58] E. Huff, A.E. Schulz, M. White, D.J. Schlegel und M.S. Warren, *Astroparticle Physics* **26** (2007), 351.
- [59] B. Jain und E. Bertschinger, *The Astrophysical Journal* **431** (1994), 495.
- [60] F. James und M. Roos, *Computer Physics Communications* **10** (1975), 343.
- [61] J. Jasche und F.S. Kitaura, *Monthly Notices of the Royal Astronomical Society* **407** (2010), 2942.
- [62] J. Jasche, F.S. Kitaura, C. Li und T.A. Enlin, *Monthly Notices of the Royal Astronomical Society* **409** (2010), 355370.
- [63] J. Jasche, F.S. Kitaura, B.D. Wandelt und T.A. Enlin, *Monthly Notices of the Royal Astronomical Society* **406** (2010), 6085.
- [64] J. Jasche und B.D. Wandelt, *Monthly Notices of the Royal Astronomical Society* **432** (2013), 894913.
- [65] D. Jeong und E. Komatsu, *The Astrophysical Journal* **651** (2006), 619.

- [66] N. Kaiser, *The Astrophysical Journal Letters* **284** (1984), L9.
- [67] N. Kaiser, *Monthly Notices of the Royal Astronomical Society* **227** (1987), 1.
- [68] E.A. Kazin, J. Koda, C. Blake, N. Padmanabhan, S. Brough, M. Colless, C. Contreras, W. Couch, S. Croom, D.J. Croton, T.M. Davis, M.J. Drinkwater, K. Forster, D. Gilbank, M. Gladders, K. Glazebrook, B. Jelliffe, R.J. Jurek, I.h. Li, B. Madore, D.C. Martin, K. Pimblet, G.B. Poole, M. Pracy, R. Sharp, E. Wisnioski, D. Woods, T.K. Wyder und H.K.C. Yee, *Monthly Notices of the Royal Astronomical Society* **441** (2014), 35243542.
- [69] F.S. Kitaura, S. Gallerani und A. Ferrara, *Monthly Notices of the Royal Astronomical Society* **420** (2011), 6174.
- [70] F.S. Kitaura, J. Jasche und R.B. Metcalf, *Monthly Notices of the Royal Astronomical Society* **403** (2010), 589604.
- [71] A. Kostić, N.M. Nguyen, F. Schmidt und M. Reinecke, *Journal of Cosmology and Astroparticle Physics* **2023** (2023), 063.
- [72] O. Lahav, K.B. Fisher, Y. Hoffman, C.A. Scharf und S. Zaroubi, *The Astrophysical Journal* **423** (1994), L93.
- [73] T. Lazeyras, A. Barreira und F. Schmidt, *Journal of Cosmology and Astroparticle Physics* **2021** (2021), 063.
- [74] T. Lazeyras und F. Schmidt, *Journal of Cosmology and Astroparticle Physics* **2018** (2018), 008008.
- [75] J. Lesgourgues. *The Cosmic Linear Anisotropy Solving System (CLASS) I: Overview*, 2011.
- [76] M. Levi, C. Bebek, T. Beers, R. Blum, R. Cahn, D. Eisenstein, B. Flaugher, K. Honscheid, R. Kron, O. Lahav, P. McDonald, N. Roe, D. Schlegel und representing the DESI collaboration. *The DESI Experiment, a whitepaper for Snowmass 2013*, 2013.
- [77] C.P. Ma und E. Bertschinger, *The Astrophysical Journal* **455** (1995), 7.
- [78] T. Matsubara, *The Astrophysical Journal* **525** (1999), 543553.
- [79] T. Matsubara, *Phys. Rev. D* **78** (2008), 083519. [Erratum: *Phys.Rev.D* 78, 109901 (2008)].
- [80] T. Matsubara, *Physical Review D* **92** (2015).
- [81] A. Meiksin, M. White und J. Peacock, *Monthly Notices of the Royal Astronomical Society* **304** (1999), 851.

- [82] M. Mirbabayi, F. Schmidt und M. Zaldarriaga, *Journal of Cosmology and Astroparticle Physics* **2015** (2015), 030030.
- [83] H. Mo, F.C. van den Bosch und S. White: *Galaxy Formation and Evolution*. Cambridge University Press, Cambridge, 2010.
- [84] C. Modi, M. White, A. Slosar und E. Castorina, *Journal of Cosmology and Astroparticle Physics* **2019** (2019), 023023.
- [85] J. Moon et al. , *Mon. Not. Roy. Astron. Soc.* **525** (2023), 5406.
- [86] F. Moutarde, J.M. Alimi, F.R. Bouchet, R. Pellat und A. Ramani, *Astrophys. J.* **382** (1991).
- [87] V. Mukhanov: *Physical Foundations of Cosmology*. Cambridge University Press, 2005. Online publication date: September 2012.
- [88] R. Neal. In *Handbook of Markov Chain Monte Carlo* (2011), Seiten 113–162.
- [89] R.M. Neal. *Slice Sampling*, 2000.
- [90] N.M. Nguyen, F. Schmidt, B. Tucci, M. Reinecke und A. Kostić. *How much information can be extracted from galaxy clustering at the field level?*, 2024.
- [91] C. Nikolis, H. Rubira und F. Schmidt, *Journal of Cosmology and Astroparticle Physics* **2024** (2024), 017.
- [92] Y. Noh, M. White und N. Padmanabhan, *Physical Review D* **80** (2009).
- [93] Y. Noh, M. White und N. Padmanabhan, *Phys. Rev. D* **80** (2009), 123501.
- [94] N. Padmanabhan, M. White und J.D. Cohn, *Phys. Rev. D* **79** (2009), 063523.
- [95] N. Padmanabhan, M. White und J.D. Cohn, *Physical Review D* **79** (2009).
- [96] N. Padmanabhan, X. Xu, D.J. Eisenstein, R. Scalzo, A.J. Cuesta, K.T. Mehta und E. Kazin, *Monthly Notices of the Royal Astronomical Society* **427** (2012), 21322145.
- [97] E. Paillas, Z. Ding, X. Chen, H. Seo, N. Padmanabhan, A. de Mattia, A.J. Ross, S. Nadathur, C. Howlett, J. Aguilar, S. Ahlen, O. Alves, U. Andrade, D. Brooks, E. Buckley-Geer, E. Burtin, S. Chen, T. Claybaugh, S. Cole, K. Dawson, A. de la Macorra, A. Dey, P. Doel, K. Fanning, S. Ferraro, J.E. Forero-Romero, C. Garcia-Quintero, E. Gaztaaga, H. Gil-Marn, S.G.A. Gontcho, G. Gutierrez, C. Hahn, M.M.S. Hanif, K. Honscheid, M. Ishak, R. Kehoe, A. Kremin, M. Landriau, L.L. Guillou, M.E. Levi, M. Manera, P. Martini, L. Medina-Varela, A. Meisner, J. Mena-Fernandez, R. Miquel, J. Moustakas, E. Mueller, A. Muoz-Gutierrez, A.D. Myers, J.A. Newman, J. Nie, G. Niz, N. Palanque-Delabrouille, W.J. Percival, C. Poppett, F. Prada, A. Prez-Fernandez, M. Rashkovetskyi, M. Rezaie, A. Rosado-Marin,

- G. Rossi, R. Ruggeri, E. Sanchez, C. Saulder, E.F. Schlafly, D. Schlegel, M. Schubnell, D. Sprayberry, G. Tarl, D. Valcin, M. Vargas-Magaa, J. Yu, S. Yuan, R. Zhou und H. Zou. *Optimal Reconstruction of Baryon Acoustic Oscillations for DESI 2024*, 2024.
- [98] S. Patrone, A. Testa und M.B. Wise. *Regularization Scheme Dependence of the Counterterms in the Galaxy Bias Expansion*, 2023.
- [99] P.J.E. Peebles und J.T. Yu, *The Astrophysical Journal* **162** (1970), 815.
- [100] M.E. Peskin und D.V. Schroeder: *An Introduction to quantum field theory*. Addison-Wesley, Reading, USA, 1995.
- [101] O.H. Philcox. *An Introduction to the EFTofLSS*, 2024.
- [102] O.H. Philcox, M.M. Ivanov, M. Simonović und M. Zaldarriaga, *Journal of Cosmology and Astroparticle Physics* **2020** (2020), 032.
- [103] J. Polchinski, *Nuclear Physics B* **231** (1984), 269.
- [104] R.A. Porto, L. Senatore und M. Zaldarriaga, *Journal of Cosmology and Astroparticle Physics* **2014** (2014), 022022.
- [105] D.K. Ramanah, G. Lavaux, J. Jasche und B.D. Wandelt, *A&A* **621** (2019), A69.
- [106] C. Rampf und T. Buchert, *Journal of Cosmology and Astroparticle Physics* **2012** (2012), 021021.
- [107] H. Rubira und F. Schmidt. *Galaxy bias renormalization group*, 2023.
- [108] H. Rubira und F. Schmidt. *The Renormalization Group for Large-Scale Structure: Origin of Galaxy Stochasticity*, 2024.
- [109] F. Schmidt, *Journal of Cosmology and Astroparticle Physics* **2021** (2021), 033.
- [110] F. Schmidt, *Journal of Cosmology and Astroparticle Physics* **2021** (2021), 032.
- [111] F. Schmidt, G. Cabass, J. Jasche und G. Lavaux, *Journal of Cosmology and Astroparticle Physics* **2020** (2020), 008008.
- [112] F. Schmidt, F. Elsner, J. Jasche, N.M. Nguyen und G. Lavaux, *Journal of Cosmology and Astroparticle Physics* **2019** (2019), 042042.
- [113] M. Schmittfull, T. Baldauf und M. Zaldarriaga, *Physical Review D* **96** (2017).
- [114] M. Schmittfull, Y. Feng, F. Beutler, B. Sherwin und M.Y. Chu, *Phys. Rev. D* **92** (2015), 123522.

- [115] M. Schmittfull, M. Simonović, V. Assassi und M. Zaldarriaga, *Physical Review D* **100** (2019).
- [116] I. Schmoldt, V. Saar, P. Saha, E. Branchini, G. Efstathiou, C. Frenk, O. Keeble, S. Maddox, R. McMahon, S. Oliver, M. Rowan-Robinson, W. Saunders, W. Sutherland, H. Tadros und S. White, *The Astronomical Journal* **118** (2007), 1146.
- [117] U. Seljak, G. Aslanyan, Y. Feng und C. Modi, *Journal of Cosmology and Astroparticle Physics* **2017** (2017), 009009.
- [118] L. Senatore, *Journal of Cosmology and Astroparticle Physics* **2015** (2015), 007007.
- [119] H. Seo und D.J. Eisenstein, *The Astrophysical Journal* **598** (2003), 720740.
- [120] H. Seo und D.J. Eisenstein, *The Astrophysical Journal* **665** (2007), 1424.
- [121] H. Seo, E.R. Siegel, D.J. Eisenstein und M. White, *The Astrophysical Journal* **686** (2008), 1324.
- [122] H.J. Seo, J. Eckel, D.J. Eisenstein, K. Mehta, M. Metchnik, N. Padmanabhan, P. Pinto, R. Takahashi, M. White und X. Xu, *The Astrophysical Journal* **720** (2010), 16501667.
- [123] H.J. Seo und D. Eisenstein, *The Astrophysical Journal* **633** (2005), 575.
- [124] B.D. Sherwin und M. Zaldarriaga, *Phys. Rev. D* **85** (2012), 103523.
- [125] Y. Shi, M. Cautun und B. Li, *Phys. Rev. D* **97** (2018), 023505.
- [126] J. Silk, *The Astrophysical Journal* **151** (1968), 459.
- [127] A.D. Sokal: *Monte Carlo Methods in Statistical Mechanics: Foundations and New Algorithms Note to the Reader. Monte Carlo Methods in Statistical Mechanics: Foundations and New Algorithms Note to the Reader.* (1996).
- [128] V. Springel, S.D.M. White, A. Jenkins, C.S. Frenk, N. Yoshida, L. Gao et al. , *Nature* **435** (2005), 629.
- [129] J. Stadler, F. Schmidt und M. Reinecke. *Fast, Accurate and Perturbative Modeling of the Cosmic Large Scale Structure; Part I: Tracer Restframe.* In preparation.
- [130] J. Stadler, F. Schmidt und M. Reinecke, *Journal of Cosmology and Astroparticle Physics* **2023** (2023), 069.
- [131] T. Steele und T. Baldauf, *Physical Review D* **103** (2021).
- [132] R.A. Sunyaev und Y.B. Zeldovich, *Astrophysics and Space Science* **7** (1970), 3.
- [133] S. Tassev, *Journal of Cosmology and Astroparticle Physics* **2014** (2014), 008008.

- [134] S. Tassev und M. Zaldarriaga, *Journal of Cosmology and Astroparticle Physics* **2012** (2012), 013013.
- [135] S. Tassev und M. Zaldarriaga, *Journal of Cosmology and Astroparticle Physics* **2012** (2012), 006006.
- [136] R. Tojeiro, A.J. Ross, A. Burden, L. Samushia, M. Manera, W.J. Percival, F. Beutler, J. Brinkmann, J.R. Brownstein, A.J. Cuesta, K. Dawson, D.J. Eisenstein, S. Ho, C. Howlett, C.K. McBride, F. Montesano, M.D. Olmstead, J.K. Parejko, B. Reid, A.G. Sanchez, D.J. Schlegel, D.P. Schneider, J.L. Tinker, M.V. Magaa und M. White, *Monthly Notices of the Royal Astronomical Society* **440** (2014).
- [137] B. Tucci und F. Schmidt, *Journal of Cosmology and Astroparticle Physics* **2024** (2024), 063.
- [138] Z. Vlah, E. Castorina und M. White, *Journal of Cosmology and Astroparticle Physics* **2016** (2016), 007007.
- [139] Z. Vlah, M. White und A. Aviles, *Journal of Cosmology and Astroparticle Physics* **2015** (2015), 014014.
- [140] C. Wagner, V. Müller und M. Steinmetz, *Astronomy & Astrophysics* **487** (2008), 63.
- [141] H. Wang, H.J. Mo, X. Yang, Y.P. Jing und W.P. Lin, *Astrophys. J.* **794** (2014), 94.
- [142] X. Wang, H.R. Yu, H.M. Zhu, Y. Yu, Q. Pan und U.L. Pen, *The Astrophysical Journal* **841** (2017), L29.
- [143] S. Weinberg. *Frontmatter*. Cambridge University Press, 1996.
- [144] M. White, *Monthly Notices of the Royal Astronomical Society* **439** (2014), 36303640.
- [145] S.S. Wilks, *The Annals of Mathematical Statistics* **9** (1938), 60 .
- [146] K.G. Wilson, *Physical Review B* **4** (1971), 3174.
- [147] D.G. York, J. Adelman, J. John E. Anderson, S.F. Anderson, J. Annis, N.A. Bahcall, J.A. Bakken, R. Barkhouser, S. Bastian, E. Berman, W.N. Boroski, S. Bracker, C. Briegel, J.W. Briggs, J. Brinkmann, R. Brunner, S. Burles, L. Carey, M.A. Carr, F.J. Castander, B. Chen, P.L. Colestock, A.J. Connolly, J.H. Crocker, I. Csabai, P.C. Czarapata, J.E. Davis, M. Doi, T. Dombeck, D. Eisenstein, N. Ellman, B.R. Elms, M.L. Evans, X. Fan, G.R. Federwitz, L. Fiscelli, S. Friedman, J.A. Frieman, M. Fukugita, B. Gillespie, J.E. Gunn, V.K. Gurbani, E. de Haas, M. Halde- man, F.H. Harris, J. Hayes, T.M. Heckman, G.S. Hennessy, R.B. Hindsley, S. Holm, D.J. Holmgren, C. hao Huang, C. Hull, D. Husby, S.I. Ichikawa, T. Ichikawa, eljko Ivezić, S. Kent, R.S.J. Kim, E. Kinney, M. Klaene, A.N. Kleinman, S. Kleinman, G.R. Knapp, J. Korienek, R.G. Kron, P.Z. Kunszt, D.Q. Lamb, B. Lee, R.F. Leger,

- S. Limmongkol, C. Lindenmeyer, D.C. Long, C. Loomis, J. Loveday, R. Lucinio, R.H. Lupton, B. MacKinnon, E.J. Mannery, P.M. Mantsch, B. Margon, P. McGehee, T.A. McKay, A. Meiksin, A. Merelli, D.G. Monet, J.A. Munn, V.K. Narayanan, T. Nash, E. Neilsen, R. Neswold, H.J. Newberg, R.C. Nichol, T. Nicinski, M. Nonino, N. Okada, S. Okamura, J.P. Ostriker, R. Owen, A.G. Pauls, J. Peoples, R.L. Peterson, D. Petravick, J.R. Pier, A. Pope, R. Pordes, A. Prosapio, R. Rechenmacher, T.R. Quinn, G.T. Richards, M.W. Richmond, C.H. Rivetta, C.M. Rockosi, K. Ruthmanskorfer, D. Sandford, D.J. Schlegel, D.P. Schneider, M. Sekiguchi, G. Sergey, K. Shimasaku, W.A. Siegmund, S. Smee, J.A. Smith, S. Snedden, R. Stone, C. Stoughton, M.A. Strauss, C. Stubbs, M. SubbaRao, A.S. Szalay, I. Szapudi, G.P. Szokoly, A.R. Thakar, C. Tremonti, D.L. Tucker, A. Uomoto, D.V. Berk, M.S. Vogeley, P. Waddell, S. i Wang, M. Watanabe, D.H. Weinberg, B. Yanny and N. Yasuda, *The Astronomical Journal* **120** (2000), 1579.
- [148] M. Zaldarriaga und M. Mirbabayi. *Lagrangian Formulation of the Eulerian-EFT*, 2015.
- [149] Y.B. Zeldovich, *Astronomy and Astrophysics* **5** (1969), 84.
- [150] V. Zheligovsky und U. Frisch, *Journal of Fluid Mechanics* **749** (2014), 404430.



# Danksagung

I would like to begin by expressing my sincere gratitude to my supervisor, Fabian Schmidt, for giving me the opportunity to work on this project. I am deeply thankful for the patience with which he has guided me and for all the invaluable knowledge he has shared over the years.

I would also like to thank the members of my thesis committee – Eiichiro Komatsu, Alex Barreira, and Ariel Sánchez – for their invaluable advice and encouragement throughout my PhD.

I am especially grateful to all the past and present members of the **LEFTfield** group – Andrija Kostić, Julia Stadler, Şafak Çelik, Ivana Nikolac, Henrique Rubira, Minh Nguyen, Sam Goldstein, and Beatriz Tucci – for all the great discussions we had during the group meetings and outside of them. I especially enjoyed our “hack” weeks. I would also like to thank Bea for being a fantastic co-author on all my papers. Our struggles with the reconstruction will forever stay with me.

I would also like to thank to the rest of of the cosmology group at MPA for all the great discussions during informology, EFTofLSS book club, journal club and random encounters in the MPA hallways. I would like to thank Marta Monelli and Anik Halder for moral and practical support during the writing of thins thesis, and to Luisa Lucie-Smith always giving good advice.

I would also like to thank my Munich friends: Ana, Ceci, Max, Anamaria and Thomas for making my stay in Munich such a great experience. I am extremely grateful to Kasia Budzik for her friendship, support and constant supply of relevant memes.

Hvala mojim prijateljima u Peći, lipo je znat da uvek mogu na vas računat da rukan otirate oblake. Hvala Barbari i Pašku što su mi posudili svoj stan za pisanje prva dva poglavlja ove teze. Neizmjerno hvala Ivani Nikolac na pomoći za vrijeme Fhrüingszeugnis avanture i na iznimno detaljnom čitanju ove teze.

Hvala mojoj obitelji na njihovoj bezuvjetnoj ljubavi i podršci (i na kilogramima pancete poslanih kroz godine u Minhen).

I na kraju Marine, tebi dugujem više no što se riječima može iskazti, hvala ti na svemu.